Arnold Schwarzenegger
Governor

ENERGY PERFORMANCE OF UNDERFLOOR AIR DISTRIBUTION SYSTEMS

Part III: The Fluid Dynamics of a UFAD System

APPENDIX C

Prepared For:
California Energy Commission
Public Interest Energy Research Program

Prepared By:
Center for the Built Environment,
University of California, Berkeley
University of California, San Diego
Lawrence Berkeley National Laboratory

October 2009
CEC-500-2007-050-APC

UNIVERSITY OF CALIFORNIA, SAN DIEGO

The Fluid Dynamics of an Underfloor Air Distribution System

A dissertation submitted in partial satisfaction of the
requirements for the degree Doctor of Philosophy
in Engineering Sciences (Systems Science)

by

Qing Liu

Committee in charge:

Professor Paul F. Linden, Chairperson
Professor Steve Buckley
Professor Rob Pinkel
Professor Sutanu Sarkar
Specialist Tom Webster
Professor Clinton Winant

2006

Copyright

Qing Liu, 2006

All rights reserved.

The dissertation of Qing Liu is approved, and it is acceptable in quality and form for publication on microfilm:

Chair

University of California, San Diego

2006

TABLE OF CONTENTS

Signature Page iii

Table of Contents vi

Vita vii

Abstract viii

1 Introduction 1
1.1 Motivation 1
1.2 Previous research 13
1.3 Turbulent plume theory 16
1.3.1 Pure plume theory 16
1.3.2 Virtual origin 21
1.4 Turbulent fountain theory 23
1.4.1 Penetrative entrainment rate 26

2 Laboratory Experiments & Numerical Modelling 29
2.1 Introduction 29
2.2 Experimental set-up 29
2.3 Density measurement technique and calibrations 33
2.4 Numerical modelling 36
2.4.1 Numerical model for a fountain flow 36
2.4.2 Entrainment rates for a plume and a fountain 37
2.4.3 Penetrative entrainment rate of a fountain at a density interface 41
2.4.4 Implementation 43

3 The Interior Zone Model — Single Source & Multiple Diffusers 45
3.1 Theoretical Model about Multiple Cooling Diffusers 45
3.1.1 Fixed heat load and total ventilation rate 45
3.1.2 Fixed heat load and underfloor pressure 49
3.1.3 An elevated heat source 50
3.2 Experimental results & comparisons with the model predictions . . 51
3.2.1 Effects of multiple diffusers 52
3.2.2 Effects of an elevated heat source 61
3.3 Conclusions 64

4 The Interior Zone Model — Single Diffuser & Multiple Sources 68
4.1 Theoretical model for multiple heat sources of same strength 69
4.1.1 Fixed heat load and total ventilation rate 71
4.1.2 Fixed heat load per heat source and total ventilation rate . . . 73
4.2 Theoretical model for multiple heat sources of different strengths . 74

4.2.1 Weak diffuser 75
4.2.2 Strong diffuser 81
4.2.3 Approximate multi-unequal-plume model with a strong diffuser flow 85
4.3 Experimental results 88
4.3.1 Two plumes of same strength 90
4.3.2 Two plumes of unequal strengths 92
4.4 Scaling analysis 98
4.5 Conclusions 101

5 The Perimeter Zone Model — Line Source & Single Diffuser 103
5.1 Theoretical model about a UFAD perimeter zone 104
5.1.1 Line plumes 104
5.1.2 UFAD perimeter zone model 107
5.2 Experimental results 109
5.2.1 Qualitative observations 111
5.2.2 Quantitative comparisons 113
5.3 Conclusion 116

6 The Comparisons between Small-scale & Full-scale Experiments 118
6.1 Full-scale tests 119
6.1.1 Equivalent parameters 122
6.1.2 Airflow leakage 123
6.1.3 Heat loss 124
6.1.4 Virtual origin 126
6.2 Stratification comparisons – interior zone 126
6.2.1 Stratification in small-scale and full-scale experiments 126
6.2.2 Effects of multiple diffusers for small-scale and full-scale experiments 130
6.3 Non-dimensional scaling comparisons 132
6.3.1 Definition of non-dimensional parameters 132
6.3.2 Interior zone scaling comparisons between small-scale and full-scale experiments 135
6.3.3 Perimeter zone non-dimensional scalings 139
6.4 Floor leakage study 142
6.5 EnergyPlus 146
6.6 Conclusion 148

VITA

2001–2006	Research Assistant, University of California, San Diego
2001	M.S., Southeast University, China
1997	B.E., Anhui University of Technology, China

ABSTRACT OF THE DISSERTATION

The Fluid Dynamics of an Underfloor Air Distribution System

by

Qing Liu
Doctor of Philosophy in Engineering Sciences (Systems Science)
University of California, San Diego, 2006
Professor Paul F. Linden, Chair

This thesis discusses the fluid dynamics of an under floor air distribution (UFAD) ventilation system in which, in contrast to conventional air conditioning systems, cool air is delivered from diffusers in the floor rather than from overhead vents. In order to produce more realistic models of UFAD systems, we extend previous work on a simplified system consisting of a single heat source at floor level and a single cooling diffuser developed by Lin & Linden (2005), to the case of multiple cooling diffusers and a single heat source located at different heights above the floor; of two and more sources of equal or unequal buoyancy fluxes and of a line heat source in a UFAD system. This is an attempt to provide more guidelines to complete the complicated models of UFAD in reality. We carry out experiments in which the heat sources are represented as buoyant point plumes, and the cooling diffusers are modelled using negatively buoyant vertical jets. The radiation from the sun into the system is represented by a line plume attached to a wall. The experiments show that the properties of the system are determined by the entrainment into the plumes and the negatively buoyant jets. In the spirit of Morton, Taylor & Turner (1956), we characterize these entrainment processes by entrainment coefficients, and develop a theoretical model based on layered models of ventilation flows introduced by Linden, Lane-Serff & Smeed (1990). The model predictions are compared with the laboratory experiments, and used to determine the dependence of these parameters on the cooling load, the ventilation rate and the properties of the cooling diffusers. The tank experiments have been compared with full-scale UFAD room tests by non-dimensional scaling analysis, based on which explicit equations were concluded to use in Energy Plus codes.

Chapter 1

Introduction

1.1 Motivation

After various attempts in the 19th century, including one by David B. Reed, an English scientist, who developed a system to humidify and ventilate the air supplied to the British House of Commons, air conditioning was invented by Willis Haviland Carrier. Carrier had his first patent 'Apparatus for Treating Air' (U.S. Patent 808897) granted in 1906, but it was Stuart H. Cramer a textile engineer who first used the term 'air conditioning' in a 1906 patent claim. Cooling for human comfort, rather than industrial need, began in 1924, in the J.L. Hudson Department Store in Detroit, Michigan. Air conditioning of apartments and homes began during the 1930s. In 1939, Packard Motors introduced air-conditioning units for cars. Currently approximately 10% of all energy use in the United States is used for heating and cooling buildings. On a hot summer day in Los Angeles the amount of energy used in cooling buildings exceeds that used by transport! In many large cities, for example Tokyo, Paris, Rome, the peak energy demand for cooling outstrips the supply. Building energy use is also responsible for 36% of U.S. emissions of CO_2.

Over the past 20 years or so architects, designers and engineers have becoming increasingly concerned with this energy use and have sought ways to make

buildings more energy efficient. Writing in the *Economist*[1], Sir Norman Foster pointed out the implications on energy use and greenhouse gas emissions with increasing industrialization of India and China, and used the word *ecotecture* to describe this concern with sustainability of the built environment. New buildings particularly in Europe but also in the US are being designed with energy efficiency as a major consideration. There are many aspects to sustainability and energy efficiency of buildings, but the fluid dynamicist can mainly contribute to the design of efficient heating and cooling systems. In many parts of the world, efficient cooling represents the main challenge and it is this aspect we address in this chapter.

The tendency for hot air to rise means that the air in a space is usually stably stratified, with the warmest air at the ceiling. Conventional air conditioning systems supply cool air at the ceiling as forced, negatively buoyant jets (figure 1.1(a)). These jets fall to the floor, driven both by their initial momentum and by their negative buoyancy, and tend to mix the air within the space, minimizing the vertical stratification. The average temperature T_R of the air within the space and the ventilation rate Q are

$$T_R = T_S + \frac{\mathtt{H}}{Q\rho C_p} \text{ or } Q = \frac{\mathtt{H}}{\rho C_p (T_R - T_S)}, \tag{1.1}$$

where T_S is the supply temperature, $\mathtt{H}$ is the heat flux of the internal gains within the space, ρ and C_p are the density and specific heat at constant pressure of air, respectively and Q. Thus for a given supply temperature T_S, the minimum flow rate occurs for the maximum return temperature T_R. In a conventional overhead system the return temperature is the same as the space temperature, but if stratification is allowed it is possible for the return temperature to be larger than the space temperature. Thus a system that produces stratification provides the potential for removing the heat load at a lower ventilation rate, thereby reducing fan power, or using a larger supply temperature T_S, thereby reducing the chiller load.

[1]Special issue December 2004, The World in 2005, p126

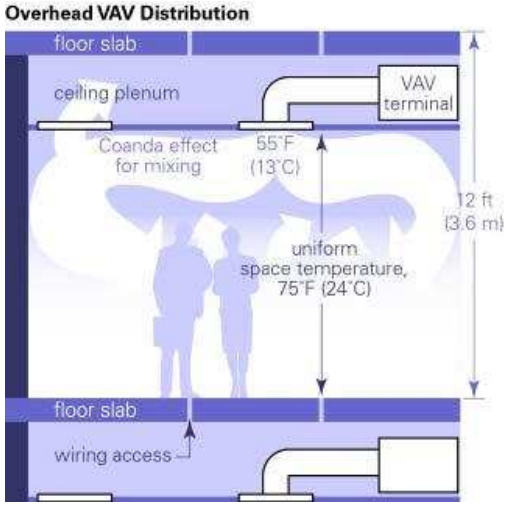

(a)

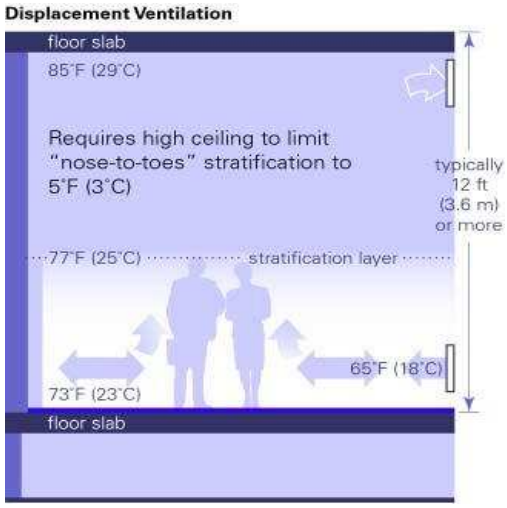

(b)

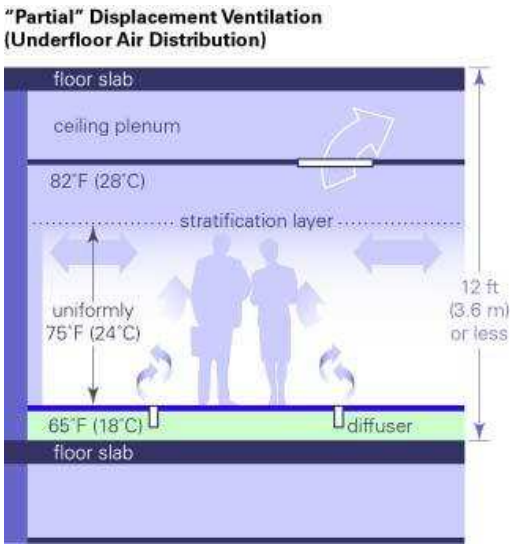

(c)

Figure 1.1: (a) A conventional overhead air conditioning system; (b) A displacement system; (c) An UFAD system (Stanke , 2001)

Thus, one way to increase the efficiency of an air-conditioning system is to allow the air within the building to stratify. This can be achieved by displacement ventilation where the cool, supply air is delivered at low velocities at the bottom of the space (figure 1.1(b)). The supply air spreads out across the floor with minimal mixing with the warmer air in the space, and the warm air is 'displaced' upwards and out of the space through return vents in the ceiling. Both the stratification and the return temperature are maximized in this case, and only the lower occupied zone is cooled. Provided some of this heated air is exchanged with cooler outside air, a fraction of the internal heat gains, rising as thermal plumes from sources within the space, are not effectively cooled. Depending on the local climate, energy savings can be as much as 40% over conventional air-conditioning systems (Bauman 2004).

The stratification within the space, while essential for realizing the energy savings, can potentially be uncomfortable. Individuals exposed to significant temperature variations over their bodies, experience discomfort. The industry standard (ASHRAE *Standard* 55–1992) recommends that vertical temperature gradients be less than 1.9K over 1m. Recent work (Zhang, Huizenga & Arens 2005) suggests that this recommendation is too restrictive, and that humans can tolerate larger variations over the body, provided no part is excessively hot or cold. Irrespective of the particular values for tolerable temperatures, it is clear that a ventilation system that seeks to create significant stratification may have a negative impact on occupant comfort. In displacement systems for example, the presence of cool air at floor level can be a cause of discomfort.

Under floor air distribution (UFAD) is a ventilation strategy that attempts to improve comfort while retaining significant energy efficiencies over convectional systems (figure 1.1(c)). UFAD uses a raised-access floor to create a plenum into which conditioned air is supplied from the chiller. This air enters the space through vents, called 'diffusers', located in panels in the floor. The flow from a diffuser takes the form of an upward negatively-buoyant turbulent jet, sometimes

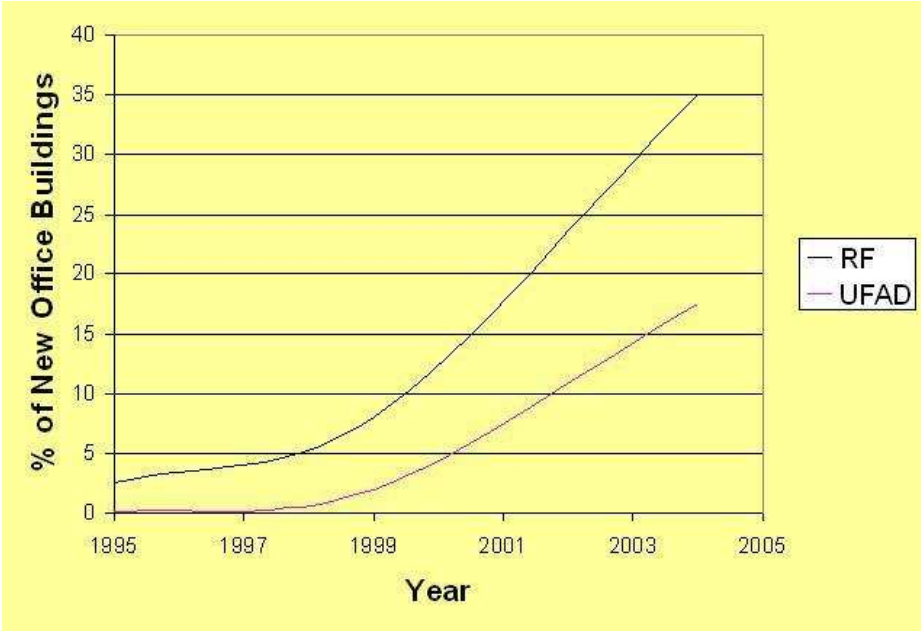

Figure 1.2: The growth of UFAD installation. "RF" refers to raised floor.

with the addition of swirl. This jet rises until its vertical momentum reduces to zero, after which it reverses and falls towards the floor. The height at which the flow reverses is known as the diffuser 'throw', and depends on the temperature of the air in the plenum and the space and the initial momentum of the flow through the diffuser. It also depends on the specific geometry of the diffuser. These designs differ across manufacturers, and can change the flow significantly from that of a simple jet. For example, some diffusers impart significant swirl to the flow using an arrangement of vanes. As in both the conventional and displacement systems the return vents on the ceiling extract the hot air from the upper region.

The diffuser flows are designed to be turbulent and air is entrained into the jet as it rises. When the flow reverses it also continues to entrain and mix the air within the space. In particular, during its descent the diffuser flow carries warm air downwards from the upper part of the space, thereby increasing the temperature near the floor. This process reduces the stratification compared to that found in a pure displacement system, and provides a compromise between

Figure 1.3: The diffuser flow visualized by smoke tests comes from a swirl Krantz diffuser in a test room (Webster *et al.* 2006).

energy efficiency and thermal comfort.

The first UFAD system was introduced in the 1950s to cool a computer room (Grahl 2002). The massive amount of cooling and air conditioning required by mainframe computers created the need for a modular cooling system. In the 1970s, underfloor air distribution was introduced into office buildings in West Germany as a solution to cable management and heat load removal issues caused by the proliferation of electronic equipment throughout the office (Sodec & Craig 1990). Prior to 1990s, UFAD had been installed in office buildings, where cooling loads are relatively small primarily in South Africa, Germany, and other parts of Europe. In the late 1990 growth for raised floor installations in the US was dramatic. As shown in figure 1.2, about 35% of new offices used raised floors by 2004 and, half of which incorporate UFAD technology.

Figure 1.4 shows an office enclosure using UFAD technology. Typically, in an open-plan environment, many diffusers are located in the floor, in order to provide localized cooling. Occupants can open or close diffusers near their work space, and this 'local control' is a popular feature. The use of modular panel floors allow the diffuser arrangements to be reconfigured easily, giving flexibility to the

Figure 1.4: An office using UFAD technology (Tate Access Floors).

use of the space. The plenum itself also provides space to run cabling and other services under the floor and avoids the need for false ceilings.

A UFAD system conserves energy since only the occupied zone is conditioned so that higher temperature supplied air, typically 18°C, can be used compared to a supply air temperature at 13°C in an overhead system. There is also a perceived improvement in air quality compared to a conventional overhead system. The plumes from the heat sources entrain pollutants from the lower part of the space and carry them to the upper, unoccupied part. Thus occupants are surrounded by relatively unpolluted supply air – rather like being washed in an inverted shower – as compared to a conventional mixing system in which pollutants are mixed throughout the space – like sitting a bath.

As the above discussion shows the optimal operation of a UFAD system involves a delicate balance between the stratification needed for energy efficiency while retaining thermal comfort. However, engineers and designers lack information and experience to design UFAD systems because wide spread use of the

technology is in its infancy, and standardized methods and guidelines are under development. The UFAD design guide by Bauman (2004) is the first and the only design book so far. Furthermore, designers need tools with which they can calculate the potential energy savings of a UFAD system when it is installed in a building. For conventional systems these calculations are made by running a thermal simulation program. These programs assume that each space within a building is well mixed and calculate the heat balances within each individual space, characterised by a single temperature, due to convective, conductive and radiative exchanges with the surfaces in the space. Since energy-efficient systems require stratification, these programs are unable to capture the energy savings. Thus there is a need to extend these simulation programs to include stratification. Typically, building simulation programs are run for whole buildings with two or more years of weather data, with a time step of 10 minutes. Consequently, the inclusion of algorithms to determine stratification must be simple or the computational overhead will be too large.

The goal of this research is to develop a model of a UFAD system that can be used by engineers to design and optimize the ventilation system, and that can be implemented in a thermal simulation program so that the performance of the design can be tested. Since radiation and other heat transfer mechanisms with the surfaces in a space are readily calculated, the problem here is to model the flow and stratification in the space driven by the internal gains and the ventilation flow itself. In order to achieve this, we need to understand and model the *fluid mechanics* of the UFAD system.

Several approaches are possible and have been used to address similar problems. The basis of thermal simulation programs is a network model, in which the spaces within a building are combined together using representations of ductwork, supply and return plenums, openings between spaces, etc. The submodel for each space then can be treated using using a number of methods.

Apart from empirical 'rule-of-thumb' approaches, the simplest is to use

zonal or nodal models (Li 1993; Rees & Haves 2001; Musy, Winkleman & Wurtz 2002). These models divide the space into zones or identify surfaces with nodes at different temperatures in order to calculate heat transfers, internal temperatures and ventilation flow rates. While these methods are computationally efficient, there is no clear basis on which to assign zones or nodes to physical space, and much is left to the skill and judgement of the modeler. Transfers between zones and nodes have to be artificially constructed using constraints such as conservation of mass.

Alternatively, computational fluid mechanics, for example using a turbulence model, large eddy simulation or direct numerical simulation of ventilation flows can be (and are) used (Mora, Gadgil & Wurtz 2003; Jiang & Chen 2003). Although theoretically feasible, these methods are difficult and expensive, due principally to the challenge of modeling stratified turbulence within complex building geometries. And, more significantly in the present context, it is not clear how such calculations can be coupled with whole-building codes. Griffith & Chen (2004) have proposed a coupling using a 'zero-equation' turbulence model. While this is a promising start, such a simplified model has significant limitations in the range of phenomena it represents.

Our approach is to develop algorithms that can be directly included into energy simulation codes. These algorithms are derived from models of the fluid flow that occur in buildings, and these are, in turn, discovered using analogue laboratory experiments. While there are limitations in this approach as well, as we will discuss below, the fact that we are modeling observed flows provides a basis for knowing what essential physics are captured, and what are not. Further, this approach leads to simplified design rules, since the physics is encapsulated in relatively simple formulas.

Experiments have two principal benefits. First, using modern visualization and data acquisition equipment, high-quality data and flow visualization may be obtained, avoiding many of the inherent difficulties of data acquisition in full-

scale rooms. Visualizations reveal the qualitative behavior of real flows, and help to identify key processes which may not be easy to observe in real buildings or numerical simulations. Second, the quantitative data obtained in the laboratory experiments may be used to formulate and test models of ventilation. These simple, experimentally based models may be used to parameterize and validate numerical simulations of flows within buildings.

The laboratory model consists of a combination of plumes, representing the internal gains from heat sources, and negatively buoyant jets, representing the flow from the diffusers. Since the pioneering work of Morton *et al.* (1956), who showed that a laboratory plume accurately represented the flow above a large scale plume in the atmosphere, it has been accepted that turbulent plumes generated in a bench-top experiments faithfully capture the physics at full scale. Morton *et al.* (1956) also showed that the entrainment into the plume – the critical factor that controls the dynamics – can be represented by an entrainment velocity that is proportional to the mean vertical velocity in the plume. The constant of proportionality is known as the *entrainment constant* α, and it takes a universal value for a buoyant plume. In a uniform environment, the existence of an entrainment constant follows from self-similarity and, crucially, Morton *et al.* (1956) showed that it also holds in stratified environments when the plume is no longer self-similar.

The study of negatively buoyant jets was initiated by Turner (1966) and investigated subsequently by, among others, McDougall (1981), Bloomfield & Kerr (1998) and Bloomfield & Kerr (2000). The jet rises to a finite height at which its vertical momentum flux is reduced to zero by the negative buoyancy force. The dense fluid then falls in an annular region surrounding the upward inner jet. Entrainment occurs between the rising jet and the falling dense fluid and the latter also entrains exterior fluid as it descends. These processes have been successfully modelled using an entrainment constant, although its value is different (smaller) than that of a plume.

It is essential that the laboratory experiments have dynamical similarity

with the full scale ventilation flows. This requires that the significant dimensionless parameters, the Reynolds number Re and the Peclét number Pe, where

$$Re = \frac{UH}{\nu}, \; Pe = \frac{UH}{\kappa}, g' = g\frac{\Delta\rho}{\rho_0} = g\frac{\Delta T}{T_0} \; , \tag{1.2}$$

which describe the relevant force balances must be similar at full scale and in the laboratory. In these expressions, H is a characteristic height scale, ν is kinematic viscosity, κ is the coefficient of molecular diffusivity, g is the acceleration due to gravity, and g' is the reduced gravity. Typical values of density and temperature are ρ_0 and T_0, and the typical fractional density change $\Delta\rho/\rho_0$ is associated with the typical fractional temperature change $\Delta T/T_0$. The Reynolds number Re is a measure of the relative importance of inertia and viscous forces, while Pe compares inertia and diffusion. In buoyancy-driven ventilation, the dominant fluid velocity is associated with the buoyancy force, which scales as $\sqrt{g'H}$. In a real room, for the air flows observed both Re and Pe are of the order of 1000 or larger. Therefore, except at the very smallest scales, the real flows are largely unaffected by viscosity and diffusion.

In the laboratory, the scale H is reduced by at least a factor of 10 when small-scale models are used to represent buildings. Sources of buoyancy, such as people, lights and equipment, are represented by fluid of different density which flows through nozzles designed to produce turbulent flow. The relative importance of the source mass, momentum and buoyancy flux can be precisely controlled by appropriate choices of the source volume flux, density difference and diameter, through well-established methods (Woods & Caulfield 1992, Caulfield & Woods 2002). Realistic values of Re and Pe, comparable to those in the full scale flows, can be achieved if the experimental fluid is water, and density differences are caused by either temperature or salinity. In this case, both ν and κ are smaller in water than in air, and g' can be made significantly larger, especially when salt is used to create the density differences, so it is possible to achieve dynamical similarity between the laboratory and room flows, the most critical part of which is the flow through the openings. Fortunately, in practice this flow takes place through

sharp-edged orifices and the pressure drop is associated with separation from these sharp edges, which is relatively insensitive to Reynolds number. So even if it is not possible to maintain such high values of Re in the laboratory, the effects are generally negligible (Hunt, Holford & Dally 2001; Linden 1999).

The study of ventilated enclosures containing a heat source also builds on the work of Baines & Turner (1969) who considered the effect of a plume in a closed container. This is the famous 'filling-box' problem in which a stable stratification is built up in the container even though the heat is added at the base. In this case the warm air in the plume spreads out across the ceiling and then descends in the interior, to compensate for the ambient fluid entrained into the plume. Since, at a later time, the plume rises through a warmer environment, it reaches the ceiling at a higher temperature than previously. Consequently, at any moment the fluid spreading at the ceiling is the warmest in the room and so the interior becomes stably stratified. If the container has insulating boundaries, the temperature increases everywhere with time and the system is inherently unsteady.

The difference with a ventilated enclosure is that heat can escape and a steady state can be achieved. As Linden *et al.* (1990) showed for a naturally ventilated enclosure with cool air entering at at the bottom and warm air leaving at the top, this steady state is also stably stratified, and the stratification takes the simple form of layers of uniform temperature separated by stable interfaces. Indeed this form of stratification occurs whenever there is a net vertical flow through an enclosure, such as in UFAD where air is also supplied at the floor and extracted at the ceiling. In the absence of conduction in the interior of the space and heat exchange with the walls, the steady, horizontally averaged heat equation is simply

$$w\frac{d\overline{T}}{dz} = 0, \tag{1.3}$$

where $\overline{T}$ is the horizontally averaged temperature, and w is the vertical velocity. Thus outside the plumes and diffuser flows there are two possibilities. Either $w \neq 0$ and $\frac{d\overline{T}}{dz} = 0$ – a layer of uniform temperature in which there is mean vertical motion

– or $w = 0$ and $\frac{d\overline{T}}{dz} \neq 0$ – an interface which the air can only cross in a plume or diffuser jet.

Consequently, we expect to observe layers and interfaces in experiments and we will construct a model by combining them with the dynamics of plumes and jets. This model is a form of zonal model, except that the zones (the layers, plumes and jets) and the exchanges between them are determined by the internal dynamics of the system. This avoids the arbitrariness of standard zonal models while retaining computational simplicity.

In a real building other factors such as heat exchanges with the surfaces and radiation alter the stratification and generally smoother temperature profiles are observed. However, as explained above these effects can be readily calculated and included in the simulation program. There is also another, pragmatic reason for considering a model using distinct layers. In order to improve current thermal simulation programs which consider each space to have a single temperature, the simplest way to extend them to include a measure of the stratification is to include two temperatures and a height. A model consisting of upper and lower layers at different temperatures and an interface of variable height does just that. The lower layer is considered to be the 'occupied zone' with a temperature T_{OZ} and the upper layer is the region above from which the air leaves with a return temperature T_R. The height of the interface gives the location of the top of the occupied zone and can be used to calculate a measure of the temperature gradient in the lower part of the space, which is important for the calculation of comfort.

1.2 Previous research

Ito & Nakahara (1954) developed a simplified temperature calculation model in a UFAD system through a number of experiments in a full-scale test chamber. In their model, the mixing process of the discharged air was divided into two regions: a completely mixed region in the lower part of the room, and a piston-

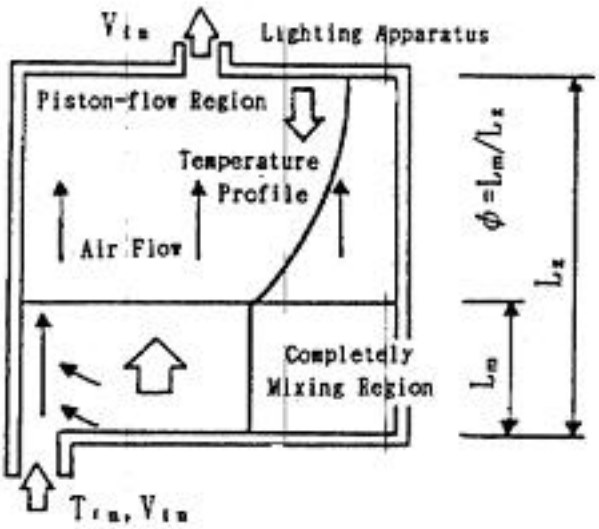

Figure 1.5: Two regions in the mixing model (Ito & Nakahara 1954).

flow region in the upper part, as shown in Figure 1.5. Based on the assumption that the discharged cool air mixed with the room air completely in the lower region, while the room air moved to the ceiling in the upper region, they derived the heat balance equations. They also found that the depth of the completely mixed region is a function of the Archimedes number ($A_r = g\alpha D_0 \Delta T$, here g is gravitational acceleration, α is the expansion coefficient, D_0 is the characteristic diameter of the outlet, and ΔT is the temperature difference between room air and supply air). Apparently, in their model, the lower mixing zone height is only affected by buoyancy and momentum of the diffuser.

Zhang (2001) developed a room air stratification model which is similar to the one of Ito & Nakahara (1954) with two regions in the ventilated space. But he argued that it is not acceptable to ignore thermal plumes in a UFAD model, since they affect the temperature stratification. He also applied the assumption by Niel (1988) that the mixing zone height should not be influenced by the momentum of air jet out of diffusers. Three sub-models including the thermal plume model (Morton *et al.* 1956), the multiple-layer model (Linden & Cooper 1996) and the room heat transfer model (Mundt 1990; Li, Sandberg & Fuchs 1992) are

integrated together in Zhang's (2001) model.

Lin & Linden (2005) conducted salt-bath simulations of the flow patterns of a simplified UFAD in a ventilated room, in which a single heat source and a single cooling diffuser are both located at the floor level. Water and salt solution were used to simulate the flow patterns caused by the different densities of hot and cool air, produced by heat sources and the cool air introduced through the UFAD system. Lin & Linden (2005) also developed a theoretical model for floor-positioned single-heat source and single-diffuser UFAD system, which was compared with the experimental measurements. The buoyancy flux of the heat source and the momentum flux of the cooling jets are found to be the controlling parameters on the stratification. Lin & Linden (2005) showed that the entrainment of warmer air from the upper zone by the flow from the cooling diffuser is a crucial feature of the performance of a UFAD system. Furthermore, he suggested a constant entrainment rate in his model.

Lin & Linden's (2005) model provides an understanding of the basic UFAD technology, and provides an efficient experimental method to simulate UFAD systems. However, in reality a UFAD system is more complicated than Lin's model. Heat sources will not be always on floor level, and there are generally multiple cooling vents and heat sources in a UFAD room.

In this research, I extend the work of Lin & Linden (2005) by considering a series of more realistic UFAD systems. I first consider the effects of multiple cooling diffusers and the vertical height of a single heat source with a single diffuser. I then examine the effects of multiple heat sources and a line plume source in a UFAD system. All these investigations consist of laboratory experiments and I develop a numerical model based on plume theory. The results are validated by comparison with large-scale experimental measurements in a UFAD test room.

1.3 Turbulent plume theory

Considerable work has been done to develop turbulent plume theory. Schmidt (1941) applied boundary-layer theory to determine the properties in a turbulent plume. Rouse, Yih & Humphreys (1952) first presented an integral model in order to identify the plume properties. The entrainment assumption proposed by Morton *et al.* (1956), which states that the rate of entrainment at the edge of the plume is proportional to the vertical velocity at that height, is the most successful approach to describe the entrainment process in a plume. Similarity theory for a heat plume assumed that the profiles of mean vertical velocity and mean buoyancy in horizontal sections are of similar form at all heights. Finally, the Boussinesq approximation assumes that the largest local variations of density in the field of motion are small compared with a chosen reference of density, which is taken as the density of the ambient fluid at the level of the source.

1.3.1 Pure plume theory

Consider a plume originating from a point source of buoyancy with a buoyancy flux B. The critical parameters are the vertical velocity $w(r, z)$, reduced gravity $g'(r, z)$ and the mean radius b. The definition of the reduced gravity is

$$g' = g\frac{\rho - \rho_r}{\rho_r}, \tag{1.4}$$

where ρ is the fluid density, ρ_r is the reference density and g is the gravitational acceleration. The Boussinesq approximation applies so that $(\rho - \rho_r) \ll \rho_r$. For an ideal gas, the reduced gravity is

$$g' = g\frac{T - T_r}{T_r}, \tag{1.5}$$

where T is the gas temperature, T_r is the reference temperature, and temperatures are in Kelvin.

Assuming the Reynolds number is high, in a uniform stationary ambient fluid, a plume is described by the buoyancy flux B and the distance above the source z. Dimensional analysis implies that

$$w \sim B^{1/3} z^{-1/3}, \;\; g' \sim B^{2/3} z^{-5/3}, \;\; b \sim z$$

Rouse, Yih & Humphreys (1952) observed in their experiments that $w(r,z)$ and $g'(r,z)$ may be described by Gaussian profiles in the plume at all heights, mathematically

$$w(r,z) \;=\; 4.7 B_0^{\frac{1}{3}} z^{-\frac{1}{3}} \exp(-96 r^2/z^2),$$

$$g'(r,z) \;=\; 11 B_0^{\frac{2}{3}} z^{-\frac{5}{3}} \exp(-71 r^2/z^2).$$

More generally, Gaussian distributions for $w(r,z)$ and $g'(r,z)$ can be expressed as

$$w(r,z) \;=\; w_g(z) \exp(-\frac{r^2}{2b_g^2}),$$

$$g'(r,z) \;=\; g'_g(z) \exp(-\frac{r^2}{2b_g^2}),$$

where w_g, g'_g and b_g are the mean axial velocity, the mean axial buoyancy, and the mean radius at the specific height z.

As the plumes are observed to be self-similar, it is sufficient to assume the top-hat distributions rather than Gaussian distributions for velocity and buoyancy. A top-hat distribution is a profile with a constant value across the plume but zero outside (figure 1.6). Therefore, the top-hat velocity distribution $\overline{w}$ is defined as

$$\overline{w}(z) \;=\; \begin{cases} \int_0^\infty 2\pi r w(r,z) dr / \pi b^2(z) & r \le b(z), \\ 0 & r > b(z), \end{cases} \tag{1.6}$$

and the reduced gravity $\overline{g'}(z)$ in the plume is given by

$$\overline{g'}(z) \;=\; \begin{cases} \int_0^\infty 2\pi r g'(r,z) dr / \pi b^2(z) & r \le b(z), \\ 0 & r > b(z). \end{cases} \tag{1.7}$$

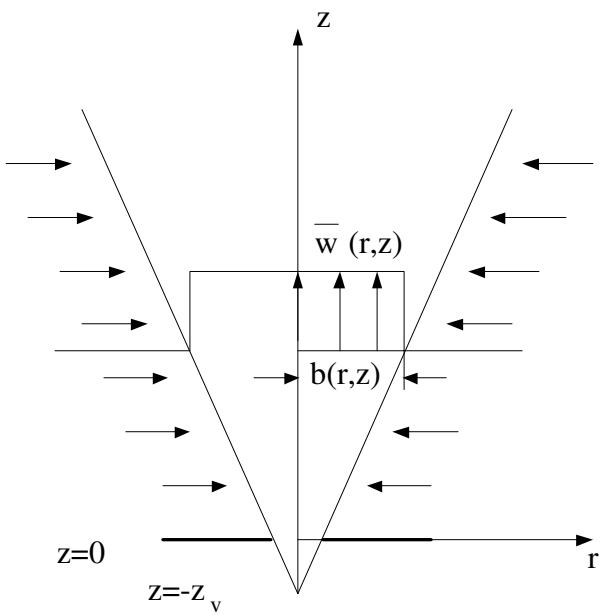

Figure 1.6: Schematic of a turbulent plume with a top-hat vertical velocity and a linearly increasing radius with height. Ambient fluid is entrained into the plume.

By applying the entrainment assumption and the top-hat profiles for velocity and buoyancy, the conservation of the fluxes of volume, momentum and buoyancy are

$$\frac{d}{dz}(\pi b^2 \overline{w}) \;=\; 2\pi b \alpha \overline{w}, \tag{1.8}$$

$$\frac{d}{dz}(\pi b^2 \overline{w}^2 \rho) \;=\; \pi b^2 g(\rho_0 - \rho), \tag{1.9}$$

$$\frac{d}{dz}[\pi b^2 \overline{w}(\rho_f - \rho)] \;=\; 2\pi b \alpha \overline{w}(\rho_f - \rho_0), \tag{1.10}$$

where, α is the entrainment constant, $\rho_0(z)$ is the environmental density, $\rho(z)$ is the mean density function inside the plume, and ρ_f is a constant reference density.

Substitute (1.8) into (1.10) and obtain

$$\begin{aligned}\frac{d}{dz}[\pi b^2\overline{w}(\rho_f-\rho)] &= (\rho_f-\rho_0)\frac{d}{dz}(\pi b^2\overline{w}) \\ &= \frac{d}{dz}[\pi b^2\overline{w}(\rho_f-\rho_0)] - (\pi b^2\overline{w})\frac{d}{dz}(\rho_f-\rho_0).\end{aligned}$$

Then, (1.10) becomes

$$\frac{d}{dz}[\pi b^2\overline{w}(\rho_0-\rho)] = \pi b^2\overline{w}\frac{d\rho_0}{dz}, \tag{1.11}$$

The Boussinesq approximation implies that the density differences $\triangle\rho = \rho_f - \rho$ are small with respect to ρ_f. Then, (1.8), (1.9) and (1.10) can be written as

$$\frac{d}{dz}(b^2\overline{w}) = 2b\alpha\overline{w}, \tag{1.12}$$

$$\frac{d}{dz}(b^2\overline{w}^2) = b^2\Delta, \tag{1.13}$$

$$\frac{d}{dz}(b^2\overline{w}\Delta) = b^2\overline{w}\frac{g}{\rho_f}\frac{d\rho_0}{dz}, \tag{1.14}$$

where the buoyancy acceleration $\Delta = -g\frac{\rho-\rho_0}{\rho_f}$.

An alternative form is

$$\frac{dQ}{dz} = 2\pi^{1/2}\alpha M^{1/2}, \tag{1.15}$$

$$\frac{dM}{dz} = \frac{BQ}{M}, \tag{1.16}$$

$$\frac{dB}{dz} = -N^2Q, \tag{1.17}$$

where, $Q = \pi b^2\overline{w}$ is the volume flux, $M = \pi b^2\overline{w}^2$ is the momentum flux, $B = Qg'$ is the buoyancy flux, and the ambient buoyancy frequency $N^2 = -\frac{g}{\rho_f}\frac{d\rho_0}{dz}$.

In a uniform ambient fluid $N = 0$, (1.17) is reduced to

$$\frac{dB}{dz} = 0. \tag{1.18}$$

Thus the buoyancy flux B is conserved at all heights in a uniform ambient environment. In this case the plume equations (1.15),(1.16) and (1.17) may be solved analytically to give the radius and vertical velocity of the plume as functions of the height as

$$b = \frac{6\alpha}{5} z, \tag{1.19}$$

$$\overline{w} = (\frac{5}{6\alpha})(\frac{9}{10}\alpha\frac{B}{\pi})^{\frac{1}{3}} z^{-\frac{1}{3}}. \tag{1.20}$$

The volume Q and reduced gravity $\overline{g'}$ in the plume are

$$Q = C(Bz^5)^{\frac{1}{3}}, \tag{1.21}$$

$$\overline{g'} = \frac{1}{C}(B^2 z^{-5})^{\frac{1}{3}}, \tag{1.22}$$

where, $C = \frac{6}{5}\alpha(\frac{9}{10}\alpha)^{\frac{1}{3}}\pi^{\frac{2}{3}}$, is a constant related to the entrainment coefficient α.

The entrainment rate α must be obtained from measurement. Recent experiments suggest that a value of $\alpha = 0.13$ should be used when top-hat variables are employed (Linden 2000).

When the ambient environment is stratified ($N^2 \neq 0$), the buoyancy flux is not conserved. In that case it is necessary to solve the equations numerically, from specified source condition (Morton *et al.* 1956). As we will see in §3 and §4, we will only be concerned with plumes rising through regions of uniform density. An numerical solution for a stratified environment is addressed in (Morton *et al.* 1956).

The Gaussian distributions and top-hat distributions provide identical values for the bulk properties of volume, momentum and buoyancy flux. However, the difference between them should not be ignored. By using Gaussian distributions for vertical velocity and reduced gravity, (1.12), (1.13) and (1.14) become

$$\frac{d}{dz}(b_g^2 w_g) \;=\; 2b_g \alpha_g w_g, \tag{1.23}$$

$$\frac{d}{dz}(b_g^2 w_g^2) \;=\; 2b_g^2 g_g', \tag{1.24}$$

$$\frac{d}{dz}(b_g^2 w_g g_g') \;=\; 2b_g^2 w_g \frac{dg_0'}{dz}. \tag{1.25}$$

Therefore, the relations of the radius, the mean axial reduced gravity and the mean axial vertical velocity in Gaussian and top-hat distributions are

$$b = \sqrt{2} b_g,\ \overline{g'} = \frac{1}{2} g_g',\ \overline{w} = \frac{1}{2} w_g,$$

and the entrainment constant has the relation of

$$\alpha \;=\; \sqrt{2}\alpha_g. \tag{1.26}$$

All subscript g indicates Gaussian profiles. Top-hat distributions are used in this thesis.

1.3.2 Virtual origin

The classical plume theory indicated in (1.12), (1.13) and (1.14) assumes an idealized (or pure) plume source, i.e, a point source of buoyancy flux B_0 with zero initial fluxes of volume Q_0 and momentum M_0. However, the plume, produced by adding salt solution, is not the 'ideal' plume of Morton *et al.* 1956 since it has finite volume flux Q_0 and momentum flux M_0 at the source. The effects of the non-ideal plume initial conditions can be accounted for by calculating a virtual origin, which is a height of the origin of an equivalent ideal plume that would have the actual (non-zero) Q_0 and M_0 at the physical location of the real plume source (figure 1.6).

A number of studies has been carried out to investigate this problem, and the virtual origin corrections may be roughly grouped, according to Hunt & Kaye

(2001), into four categories: (i) corrections based on empirical measurements (e.g. Morton *et al.* 1956; Turner 1966); (ii) a 'conical' source correction (e.g. Schmidt 1941); (iii) a jet-length based correction (e.g. Morton 1959); and (iv) a source correction based on the initial properties B_0, M_0 and Q_0 of the plume (e.g. Morton 1959).

Hunt & Kaye (2001) developed an analytical expression for the location of the asymptotic virtual source relative to the actual source of a lazy plume. They argued that a plume with the actual initial source conditions (Q_0, M_0, B_0) at $z = 0$, may be replaced with an equivalent point source pure plume with source conditions $(0, 0, B_0)$ at a virtual origin $z = -z_v$ located below the actual source.

Applying the plume theory (1.23), (1.24) and (1.25) (Gaussian profiles were used), Hunt & Kaye (2001) found that

$$\frac{z_v}{\frac{5}{6\alpha_g\sqrt{2\pi}}\frac{Q_0}{M_0^{1/2}}} = \Theta^{-\frac{1}{5}}(1-\delta) \qquad \text{for} \qquad \Theta > \frac{1}{2}, \tag{1.27}$$

where, the source parameter Θ is defined in terms of the actual physical fluxes in (1.28),

$$\Theta = \frac{5}{2^{\frac{7}{2}}\alpha_g\sqrt{\pi}}\left(\frac{{Q_0}^2 B_0}{M_0^{\frac{5}{2}}}\right), \tag{1.28}$$

$$\phi = \frac{\Theta - 1}{\Theta}, \tag{1.29}$$

and δ denotes the summation

$$\delta = \frac{3}{35}\phi + \frac{9}{42}\phi^2 + \frac{11}{1125}\phi^3 + ... \tag{1.30}$$

$$= \frac{3}{5}\sum_{n=1}^{\infty}\left(\frac{\phi^n}{5^{n-1}n!(10n-3)}\prod_{j=1}^{n}(1+5(j-1))\right). \tag{1.31}$$

They assumed that the exit velocity profile of the (circular) nozzle was uniform so that $M_0 = 4Q_0^2/\pi d_0^2$, where d_0 is the nozzle diameter. Therefore,

$$z_v = \frac{5d_0}{6\alpha_g 2^{\frac{3}{2}}}\Theta^{-\frac{1}{5}}(1-\delta). \tag{1.32}$$

In our experiments with point sources, Θ is around 5. The virtual origin of the plume z_v for our experiments, determined by (1.32), ranges from 1.0 to 1.3 cm, which is small compared with the depths of the tanks.

1.4 Turbulent fountain theory

Turbulent fountains are formed when a continuous jet of dense fluid is injected upwards into a lighter environment (Turner 1966). The entrainment of surrounding fluid into the turbulent fountain causes two effects: an increase of the volume flux with height and a decrease of the density of the rising fluid due to the addition of lighter ambient fluid. When the fountain is first started, the vertical velocity in the fountain decreases to zero at the initial maximum height, z_i, and then the flow reverses direction to fall as an annular plume which surrounds the central upflow. Subsequently, the turbulent interaction between the upflow and downflow reduces the height of the top of the fountain to a final maximum height, z_f.

A number of experimental studies in homogeneous environment,e.g. Turner (1966); Seban, Behnia & Abreu (1978); Mizushina, Ogino, Takeuchi, & Ikawa (1982) and in linearly stratified environments, e.g. Bloomfield & Kerr (1998) have been carried out.

The maximum height is considered to be a function of the initial momentum flux $M_0 = [L^4T^{-2}]$ and the buoyancy flux $F_0 = [L^4T^{-3}]$ from the source. Dimensional analysis estimates that the final maximum height, z_f is

$$z_f \;=\; C_f M_0^{\frac{3}{4}} \left|F_0\right|^{-\frac{1}{2}}, \tag{1.33}$$

where, C_f is a dimensionless constant. The empirical constant value C_f was measured by different investigators and found to range from 1.70 to 1.85 under a range of source Froude numbers ($Fr = \frac{\overline{w}_0}{\sqrt{b_0 \overline{g'_0}}}$) (Bloomfield & Kerr 2000).

In a homogeneous environment, the governing equations for a fountain

can be quantified using the entrainment equations of Morton *et al.* (1956):

$$\frac{d}{dz}(b^2\overline{w}) = 2\alpha_f b\overline{w}, \tag{1.34}$$

$$\frac{d}{dz}(b^2\overline{w}^2) = b^2\Delta, \tag{1.35}$$

$$\frac{d}{dz}(b^2\overline{w}\Delta) = 0, \tag{1.36}$$

where α_f is the entrainment coefficient of the fountain. The solutions of these equations have been successfully used to predict the initial height that a turbulent fountain reaches before the reverse flow has formed (Morton 1959; Bloomfield & Kerr 1998). However, these equations fail after the reverse flow forms. Morton (1962) suggested a double structure of coaxial turbulent jets to overcome this problem. Although at that time he did not know how the single idea of entrainment across a jet boundary should be extended in the more complicated "double" structure, Morton proposed one formulation to quantify the mixing between the core jet and the outer, annular jet.

McDougall (1981) applied the entrainment formulation proposed by Morton (1962) for coaxial jets in his theoretical modelling of a turbulent fountain in a homogeneous fluid. He argued that the supply of energy to the turbulence in the upflow arose because of the difference in mean velocities between the upflow and the downflow; similarly, the turbulence in the downflow occurred as a result of the shear between the flow and the stationary environment. These arguments lead to

$$\omega_\alpha = \alpha_f(w_u + w_d),\ \omega_\beta = \beta w_d,\ \omega_\gamma = \gamma w_d \tag{1.37}$$

where w_u and w_d are the upward and downward velocities, respectively, α, β and γ are the relevant entrainment coefficient, ω_α, ω_β and ω_γ are defined as the velocity of entrainment into the upflow, the velocity entering the downflow from the upflow, and that for ambient fluid mixed into the downflow, respectively. McDougall (1981)

was able to predict the final fountain height as well as the width, velocity and buoyancy in the upflow and downflow.

However, McDougall's (1981) formulation assumes that the shear between the upward and downward flows affects the upflow only. It not necessarily the case that the turbulence generated by the shear would be transferred in one direction only. Therefore, Bloomfield & Kerr (2000) argued that the total shear, $w_u + w_d$, should be partitioned so that the entrainment velocities depend on the relevant fraction of the total shear (figure 1.7) , i.e.

$$\omega_\alpha = \alpha_f w_u, \ \omega_\beta = \beta w_d, \ \omega_\gamma = \gamma w_d \tag{1.38}$$

Apparently, α_f is the only free parameter of the equations before the reversal. For top-hat distributions of vertical velocity and reduced gravity, Bloomfield & Kerr (1998) found that $\alpha_f = 0.085 \pm 0.01$ for a point source. This is a value between $\alpha_{jet} = 0.076 \pm 0.004$ (Alberson, Dai, Jensen & Rouse 1950) and $\alpha_{plume} = 1.117 \pm 0.004$ (Fischer, List, Koh, Imberger & Brooks 1979).

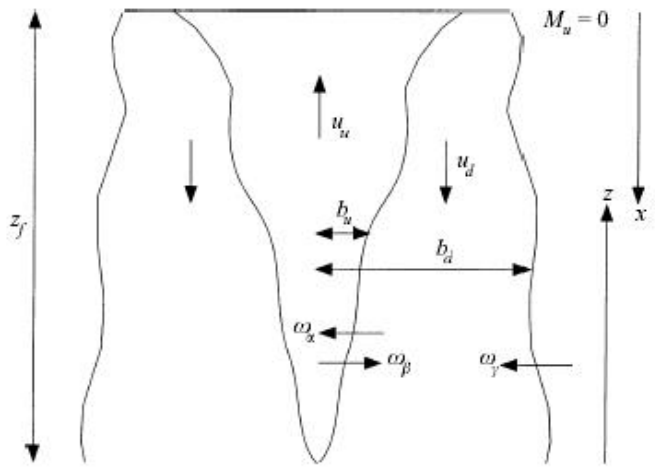

Figure 1.7: A turbulent fountain model (Bloomfield & Kerr 2000).

Bloomfield & Kerr (2000) modelled the downflow as a line plume which encircles the upflow by fixing β and γ at the value found for a line plume with

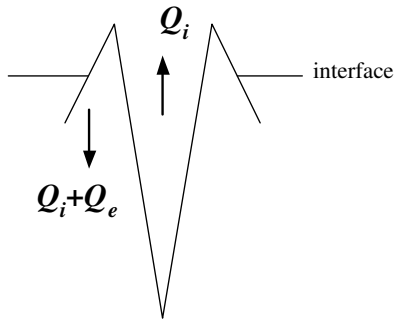

Figure 1.8: A fountain in a two-layer stratification.

top-hat profiles of velocity and buoyancy: $\beta = \gamma = 0.147$ (List 1982).

Lin (2003) focused on the penetrative entrainment by the downflow of a turbulent fountain through an interface, since his UFAD model has two-layer stratification. He assumed (figure 1.8) that the penetrative entrained volume flux Q_e across the density interface is proportional to the impinging volume flux at the density interface Q_i

$$Q_e = Q_i E, \tag{1.39}$$

where, E is the penetrative entrainment rate, which will be discussed in §1.4.1. Lin (2003) suggested a constant penetrative entrainment rate with values of E from $0.55 \sim 0.65$.

1.4.1 Penetrative entrainment rate

The penetrative entrainment refers to the entrainment by the fountain that brings a certain amount of upper zone warm fluid to the lower occupied zone. Baines (1975) argued that the entrainment rate must be a function of the local width, velocity and buoyancy difference, which can be combined to a dimensionless parameter, the Richardson number Ri:

$$Ri = \frac{\Delta g' \, b_i}{w_i^2}, \tag{1.40}$$

where, w_i and b_i are the vertical velocity and the radius of the buoyant plume at the density interface position respectively; and $\Delta g^{'}$ is the reduced gravity step at the interface. Therefore, it is assumed here that the penetrative entrainment rate across the density interface is a function of the local Richardson number Ri. And the penetrative entrainment rate is defined

$$E\,(Ri) \;=\; \frac{Q_e}{Q_i}, \tag{1.41}$$

(Lin 2003) (figure.1.8). The dimensionless parameter, E, was determined from experimental data.

From (1.40), Ri can be considered as a ratio of buoyancy energy and kinetic energy. If kinetic energy dominates, which means Ri is small, the fountain has high energy to penetrate further in the upper warmer layer, and brings more warm fluid from the layer. If potential energy, which prevents the fountain rising further, is the dominant parameter, Ri is large, and the entrainment by the fountain is reduced. This implies that E is a decreasing function of Ri.

In previous research on the penetrative entrainment E, two different decreasing functions of Ri, $E \sim Ri^{-3/2}$ and $E \sim Ri^{-1}$, were applied.

Baines (1975) studied a plume or jet impinging on a density interface, and found that

$$E \;=\; 0.1Ri^{-3/2} \tag{1.42}$$

for his experiments when $Ri > 0.83$.

Linden (1973) investigated the the interaction of a vortex ring with a sharp density interface in the laboratory, and proposed a model for turbulent entrainment. The rate of entrainment is found to be proportional to $Ri^{-3/2}$, which is consistent with the results of Baines (1975).

Kumagai (1984) studied the turbulent entrainment by a plume impinging on an interface, and he derived an empirical formula for the penetrative entrain-

ment rate to fit his experimental data:

$$E = \frac{Ri^{-3/2}}{1 + 3.1Ri^{-1} + 1.8Ri^{-3/2}} \tag{1.43}$$

where, $0.1 < Ri < 100$.

More recently, Cardoso & Woods (1993) who studied mixing at a density interface by a turbulent plume, proposed that the entrainment rate was proportional to Ri^{-1}, instead of $Ri^{-3/2}$, over an intermediate range $1.2 < Ri < 30$. Their model fits the experiments of Kumagai (1984) better in this restricted region of Ri than (1.43).

Lin (2003) noted that the performance of a UFAD system depends on the penetrative entrainment of warmer air from the upper zone by the flow from the cooling diffuser, and he applied a constant entrainment rate E in a range between 0.55 and 0.65. Most of his theoretical predictions agree with his experiment results within 10%.

Chapter 2

Laboratory Experiments & Numerical Modelling

2.1 Introduction

The salt-bath technique used in this research has been used in buoyancy-driven flows for half a century, since Bachelor (1954) first used it to study the heat convection and buoyancy effects in fluids. Salt solution has a negative buoyancy force in fresh water, which is in contrast to the heat convection problems in building ventilation. However, for the Boussinesq flows, this reversal of the direction of the buoyancy force is unimportant to the dynamics. If salt solution is introduced through a source nozzle at the top of a tank of fresh water, a plume forms in the tank. On the contrary, if fresh water is injected downward into a tank of salt solution, a fountain forms (Lin 2003).

2.2 Experimental set-up

Experiments were conducted in two clear plexiglas tanks (tank"A" with uniform cross-sectional area 30.6cm $\times$15.3cm and 30.6cm deep, and tank "B" with the dimensions of 58.5cm long, 28cm wide and 58.5cm deep) filled with fresh water. There are two reservoir tanks. One stores fresh water, and the other one is filled

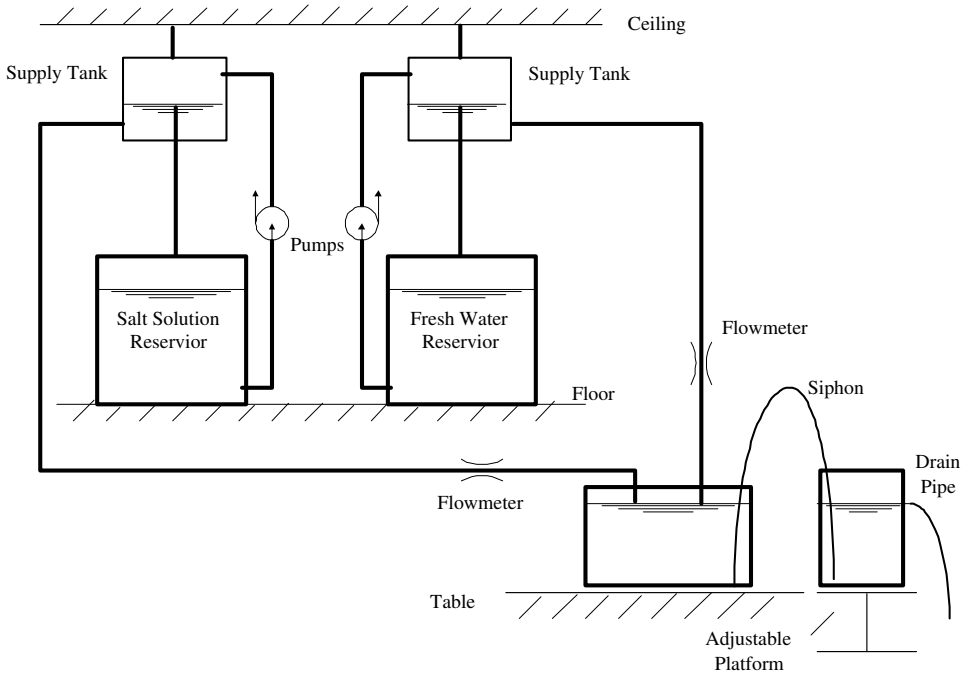

Figure 2.1: A sketch of the experiment set-up.

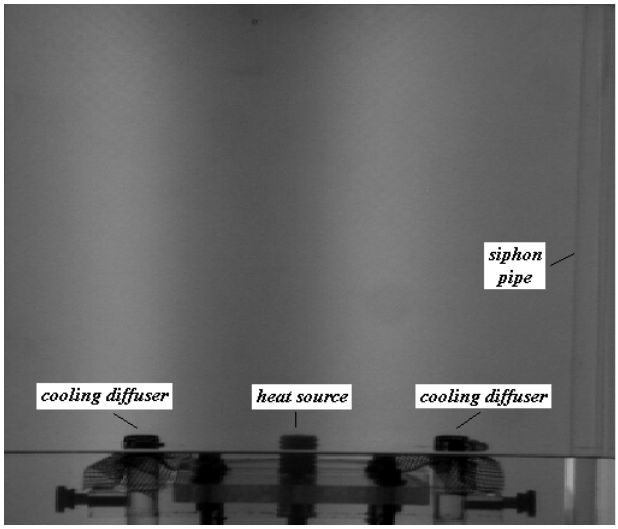

Figure 2.2: A DigImage image of the tank set-up with two diffusers.

with salt solution with a given concentration and a certain amount of dye, for flow visualization and quantitative measurement.

The outline of the experiments is as follows (figure 2.1). Two routes are set up for dyed salt solution and transparent fresh water, respectively. Each route starts from its own reservoir tank, from where the fluid gets pumped to a corresponding source supply tank hanging from the ceiling; and then comes down through a flow meter (Gilmont Correlated Flow Meters) which measures the flow rate of the fluid. Each source supply tank has a fixed height drain pipe so that a constant head is ensured, and redundant fluid is recycled to the reservoir tank through the drain pipe. The constant source supply pressure head to the source nozzle maintains a steady flow rate into the plexiglas tank. A siphon pipe with an inner diameter 1.57cm was used to keep a constant volume of fluid in the plexiglas tank (figure 2.2).

The salt solution and fresh water flow into different nozzles to make a plume and a fountain, separately. A single heat source was represented by a plume. The circular plume nozzle (diameter $d_0 = 0.5$cm) used in the experiments, as shown in Figure 2.3(a), was designed by Dr. Paul Cooper in the Department of Engineering, University of Wollongong, NSW, Australia. This design has a sharp expansion which excites a turbulent flow in a large chamber and, therefore, a turbulent plume is produced at the point of discharge. This is achieved by forcing the source solution through a narrow opening (0.1cm in diameter) from which it passed into the larger cylindrical chamber (1cm in diameter) before finally being discharged from the nozzle through a fine mesh (aperture size about 0.06cm $\times$0.06cm).

Cooling diffusers represented by fountains were used in my experiments. The fountain source nozzles in the experiments are plexiglas pipes (1.27cm in diameter) with a piece of fine mesh (aperture size about 0.1cm$\times$0.1cm) wrapped at one end to produce turbulent fountains into the ambient environment (figure 2.3 (b)).

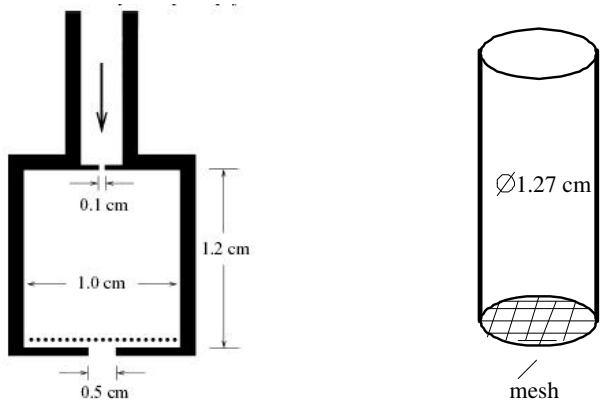

(a) (b)

Figure 2.3: (a) A plume nozzle. The arrow indicates the direction of flow into the nozzle. The line of dots adjacent to the outlet of the nozzle represent a fine square mesh (aperture size approx. 0.06cm ×0.06cm) Hunt & Linden (2001).; (b) A fountain nozzle with a piece of fine mesh (aperture size about 0.1cm×0.1cm)

.

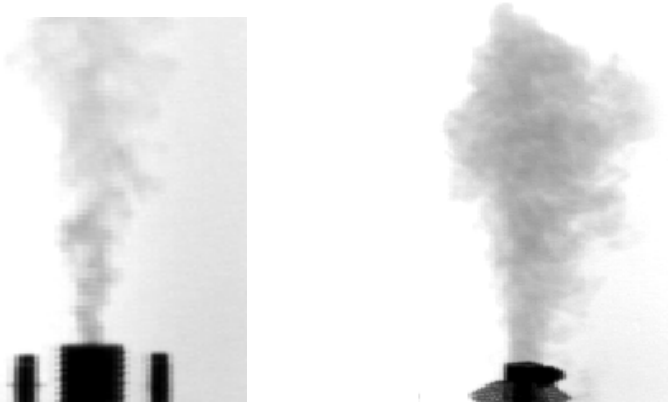

(a) (b)

Figure 2.4: (a) A plume image; (b) A fountain generated. There is a laminar length close to the source before turbulence develops.

All nozzles are separated from one another horizontally by about 6 $\sim$ 8 cm, so that the plumes and fountains develop independently. Discussions of interacting jets and plumes, of relevance when a diffuser is located close to a heat source or when heat sources are close together, can be found in Hunt, Linden & Cooper (2001) and Kaye & Linden (2004).

2.3 Density measurement technique and calibrations

Since it has a similar diffusion coefficient as the salt, the dye acts as a tracer for density. Light intensity signals are used to measure the density distribution and investigate the flow pattern evolution. It is of great importance that the light signals can be manipulated in order to obtain the true physical properties of the flow.

All experiments were recorded by capturing images with a 4910 series monochrome Charge-Coupled Device (CCD) camera at 1 minute intervals through a DT-2862 60Hz frame grabber card into a computer hard drive (figure 2.5). Tracing paper was used between the lighting source and the water tank to diffuse the light to make it as uniform as possible. The intensity attenuation of a tracer dye under a constant lighting source was analyzed by visualization software, *DigImage* (Dalziel 1993, 1992-1998) to determine the local density averaged across the width of the tank. In the *DigImage* Program, each image has two-dimensional light intensity signals with resolution 512 pixels $\times$480 pixels along horizontal direction x, and vertical direction z. The light intensity signals are values between 0 and 255(8 bytes greyscale signal), from the darkest to the brightest. The intensity results from the change in the incident light as it passes through the tank and so this method gives an average of the density from the front to the back of the tank.

In order to obtain applicable calibration between the intensity attenuation and the fluid density, the same background lighting, salt solution and camera settings were used in the calibration experiment and the real experiments. In

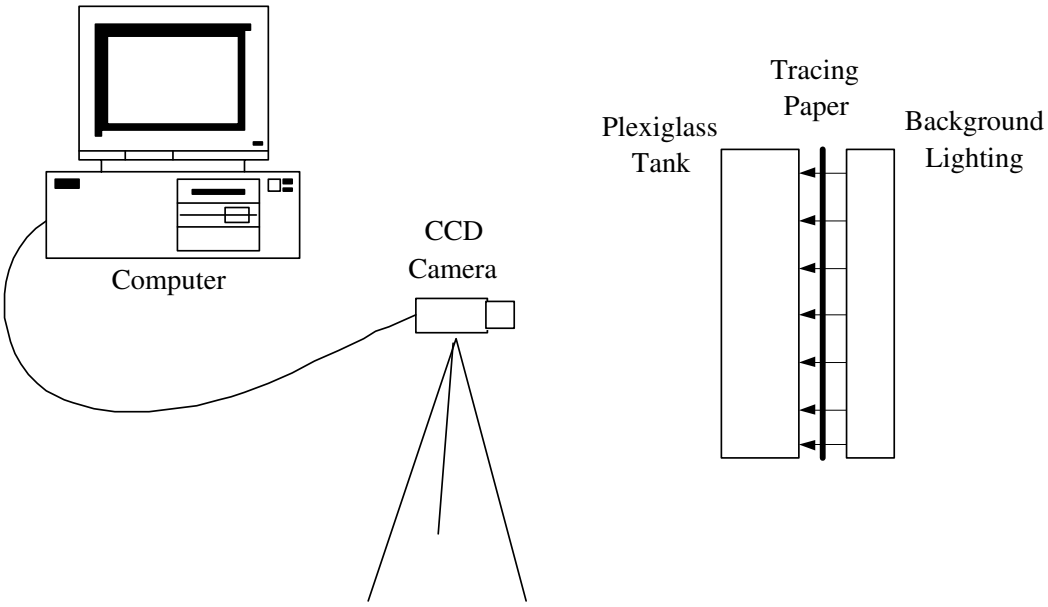

Figure 2.5: Lighting signals processing set-up

a calibration experiment, before any dye was added, a background image with background lighting B was recorded. About 25ml of dyed salt solution was added and mixed at each time to the tank initially filled with fresh water. For each time, a new image with the lighting F was recorded, and the sample from the tank was measured with an Anton Paar DMA 5000 density meterr, accurate to 10^{-5} g cm^{-3}. The final mean intensity of each new image corrected by the background image R can be calculated by

$$R = 255 \times \frac{F}{B}. \tag{2.1}$$

A typical diagram of density vs. averaged intensity is shown in figure 2.6. Apparently, light intensity is much more sensitive in a range of small density than that of large density. Therefore, this technique is expected to be more accurate for small density concentrations. This chart as shown in figure 2.6, is the reference to interpret the density profiles or evolutions of the flow in the experiments. It is important to apply the same environmental conditions in calibration experiments as those in the real experiments; otherwise, the diagram of the density vs. av-

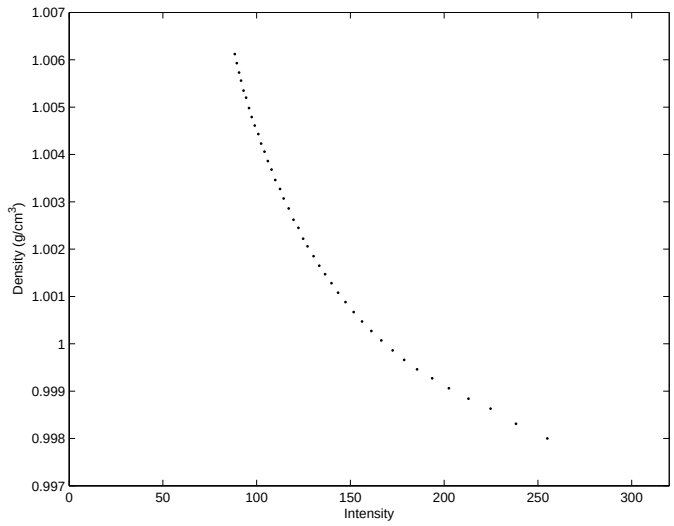

Figure 2.6: The calibration chart of salt water density and the average intensity attenuation.

eraged intensity will not translate the accurate density information for the real experiments.

The density distribution in the tank was verified by withdrawing small samples of fluid, typically 3 ml, at 1 cm intervals in height with a syringe. The density was measured again, with the Anton Paar DMA 5000 density meter. The discrepancy between these two measuring methods, which is within 5% of the initial salt concentration, comes mainly from the fact that the measurements were taken at different times. The fluid samples were withdrawn after each experiment was completed, while the light attenuation was extracted from the video taken during the experiments. Some other factors, such as the variability of the salt solution density and the background lighting, also contribute to the discrepancy.

Two types of flow meter, GF-1360 and GF-1460 manufactured by Glimont instrument company, were used in the experiments. I calibrated the flow meters to obtain the actual flow rates for the readings on flow meters. A stop watch and a graduate were used to measure the time, t (s) and the volume, V (cm^3) of fluid comes through a flow meter within the time, respectively. So, the flow rate

is $Q = V/t$ (cm^3/s). For each reading, these measurements were repeated three times. An averaged flow rate, $\bar{Q} = 1/3(Q_1 + Q_2 + Q_3)$ (cm^3/s) is considered the calibrated flow rate for that reading. We found that the calibration changes with the density of the fluid. In other words, new calibration is needed if the density of the supply fluid changes. With careful operation and the usage of an averaged flow rate, the sources of errors are mainly intrinsic errors. The calibrated flow rate is accurate to 10^0 cm^3/s. Correspondingly, the buoyancy flux B is also accurate to 10^0 cm^4/s^3.

2.4 Numerical modelling

2.4.1 Numerical model for a fountain flow

In order to get the volume flux of the fountain at the interface Q_i (figure 1.8), we need to solve the plume equation numerically. Based on the initial source volume flux Q_0, momentum flux M_0 and buoyancy flux F_0 of the fountain, a set of non-dimensional variables is given by

$$\begin{aligned} \tilde{z} = M_0^{-\frac{3}{4}} F_0^{\frac{1}{2}} z, \quad \tilde{b} = M_0^{-\frac{3}{4}} F_0^{\frac{1}{2}} b, \\ \tilde{u} = M_0^{\frac{1}{4}} F_0^{-\frac{1}{2}} \overline{w}, \quad \tilde{\Delta} = M_0^{\frac{5}{4}} F_0^{-\frac{3}{2}} \Delta. \end{aligned} \tag{2.2}$$

Therefore, the dimensionless fluxes of volume $\tilde{Q} = \tilde{b}^2\tilde{u}$, momentum $\tilde{M} = \tilde{b}^2\tilde{u}^2$, and buoyancy $\tilde{F} = \tilde{b}^2\tilde{u}\tilde{\Delta}$, and the governing equations (1.34), (1.35) and (1.36) have the non-dimensional forms

$$\frac{d}{d\tilde{z}}(\tilde{b}^2\tilde{u}) = 2\alpha_f \tilde{b}\tilde{u}, \tag{2.3}$$

$$\frac{d}{d\tilde{z}}(\tilde{b}^2\tilde{u}^2) = \tilde{b}^2\tilde{\Delta}, \tag{2.4}$$

$$\frac{d}{d\tilde{z}}(\tilde{b}^2\tilde{u}\tilde{\Delta}) = 0. \tag{2.5}$$

The starting conditions for the integration of the above equations (2.3), (2.4) and (2.5) are defined at a height $z_0 = z_l$ of the fountain source, where turbulence starts in the fountain. Then, the non-dimensional source conditions are $\tilde{Q}(\tilde{z}_0) = M_0^{-\frac{5}{4}} F_0^{\frac{1}{2}} Q_0$, and $\tilde{M}(\tilde{z}_0) = 1$ from (2.3). In a uniform environment, $\tilde{F}$ is unchanged from its value at the source, which gives $\tilde{F}(\tilde{z}_0) = -1$.

2.4.2 Entrainment rates for a plume and a fountain

Hunt & Linden (2001) suggest the entrainment rate $\alpha_g = 0.083$ for a plume (figure 2.4(a)) generating from the nozzle in figure 2.3(a), which implies $\alpha = 0.117$ for a top-hat distribution according to (1.26).

A fountain (figure 2.4(b)) originating from the nozzle in figure 2.3(b) can not be considered as a point source with finite momentum flux but zero volume flux so it is possible that the entrainment constant suggested by Bloomfield & Kerr (1998) is not applicable in my experiments. Supplementary experiments were carried out in order to determine α_f for the specific nozzle (See table 2.1).

In each experiment in table 2.1, the tank was filled with salt water of a uniform density as ρ_0. Fresh water came through the fountain nozzle to form a fountain flow. We measured the initial maximum height z_i that the fountain went and the laminar length z_l of the fountain had at its orifice. The corrected height is then $z_i - z_l$.

There are two assumptions for the fountain source momentum. The first assumes that the velocity at the source is uniform, so that the momentum fluxes can be determined simply from the volume flux and the source cross-sectional area:

$$M_0 = \frac{Q_0}{\pi r_0^2}, \tag{2.6}$$

where $r_0 = 0.635$cm is the measured radius of the fountain nozzle.

The second assumes a parabolic velocity at the source due to the Poiseulle flow in the pipe. Therefore, the velocity at the orifice is given as

Run No.	ρ_0 (g/cm^4)	Q_0 (cm^{3}s^{-1})	Measured z_i (cm)	z_l (cm)	Corrected z_i (cm)
1	1.00030	6.73	5.49	0.69	4.84
2	1.00031	10.1	12.1	1.3	10.8
3	1.00036	13.8	18.15	1.77	16.38
4	1.00033	17.4	24.48	4.3	20.18
5	1.00149	6.73	3.91	0.74	3.17
6	1.00152	10.1	9.03	1.3	7.73
7	1.00157	13.8	13.31	1.58	11.73
8	1.00165	17.43	17.59	1.86	15.73
9	1.01073	6.73	1.67	0	1.67
10	1.01075	10.1	4.17	0	4.17
11	1.01078	13.8	5.91	0.33	5.58
12	1.01066	17.4	8.58	0.42	8.16
13	1.01054	22.0	10.5	0.92	9.58
14	1.0103	26.3	15.08	1.28	13.8
15	1.01013	30.8	17.08	1.58	15.5
16	1.01097	36.3	19.58	1.83	17.75

Table 2.1: These are experimental data for 16 runs. ρ_0 is the constant environmental density, z_i is the initial maximum height of the fountain, and z_l is the laminar length of the fountain before turbulence develops.

$$u_0 = 2\bar{u}(1 - \frac{r^2}{r_0^2}) \tag{2.7}$$

where $\bar{u}$ is the averaged velocity at the orifice. For a fixed volume flux Q_0,

$$\bar{u} = Q_0/(\pi r_0^2) \tag{2.8}$$

is the equivalent uniform velocity.

The source momentum is

$$M_0 = \int_0^{r_0} u_0^2 2\pi r\, dr = \frac{4}{3}\bar{u}\pi r_0^2. \tag{2.9}$$

Substituting (2.8) into (2.9), we have

$$M_0 = \frac{4}{3}\frac{Q_0^2}{\pi r_0^2}. \tag{2.10}$$

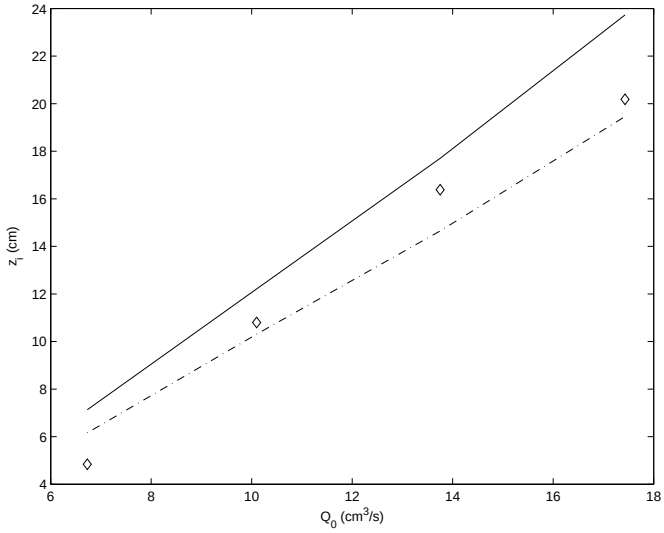

(a)

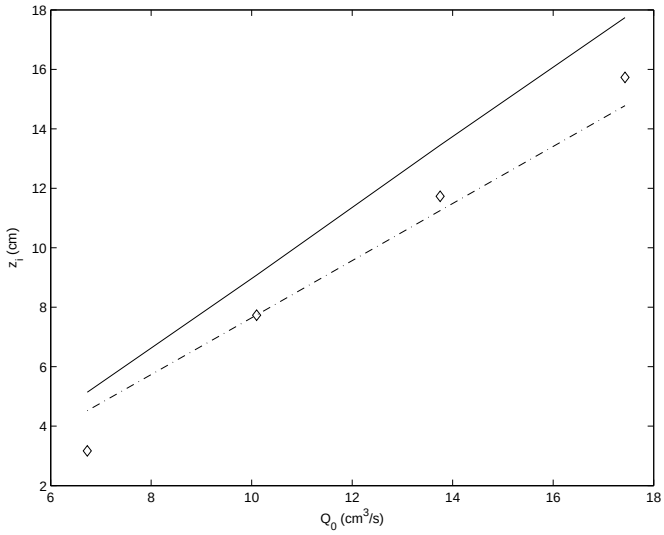

(b)

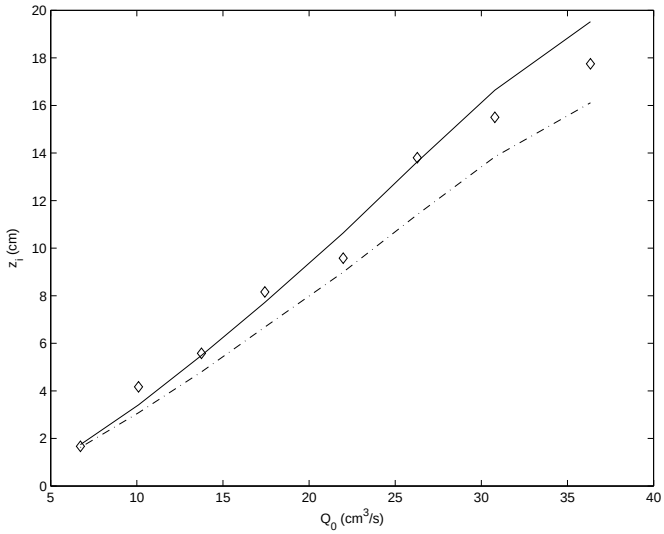

(c)

Figure 2.7: Fountains in a uniform environment. Experimental measurements (diamonds) are compared to theoretical predictions with $\alpha_f = 0.06$ (solid lines) and $\alpha_f = 0.095$ (dash lines). (a) Run 1 $\sim$ 4; (b) Run 5 $\sim$ 8; (c) Run 9 $\sim$ 16.

	Assumption "A"		Assumption "B"			
Run No.	$\alpha_f = 0.06$	$\alpha_f = 0.0848$	$\alpha_f = 0.06$	$\alpha_f = 0.075$	$\alpha_f = 0.0848$	$\alpha_f = 0.095$
1	4.84	4.45	7.13	6.65	6.4	6.16
2	8.78	7.84	12.21	11.26	10.82	10.31
3	13	11.49	18.15	16.23	15.44	14.65
4	17.81	15.48	17.7	21.59	20.46	19.46
5	3.39	3.17	23.73	4.83	4.68	4.52
6	6.33	5.72	5.14	8.44	8.09	7.74
7	9.7	8.62	9.08	12.35	11.8	11.25
8	13.11	11.52	13.45	16.26	15.47	14.78
9	1.05	1.01	1.74	1.68	1.66	1.62
10	2.17	2.05	3.41	3.26	3.17	3.08
11	3.64	3.38	5.49	5.17	4.96	4.8
12	5.3	4.83	7.72	7.2	6.94	6.68
13	7.51	6.77	10.64	9.85	9.39	8.99
14	9.77	8.69	13.63	12.52	11.89	11.41
15	12.21	10.78	16.64	15.24	14.49	13.84
16	14.44	12.72	19.52	17.81	16.96	16.11

Table 2.2: These are theoretical predictions of the initial maximum height for 16 runs. Assumption "A" and "B" refer to a uniform and a parabolic velocity at the source, respectively.

Comparing the initial maximum heights for each fountain experiment in table 2.1 with the theoretical predictions in table 2.2, we notice that the uniform source velocity assumption underestimates z_i, even if a small $\alpha_f = 0.06$ is used. With the parabolic orifice velocity assumption, z_i is well predicted if α_f is chosen in the range between 0.6 and 0.95 (figure 2.7). Therefore, instead of applying $\alpha_f = 0.085 \pm 0.01$ for a point source found by Bloomfield & Kerr (1998), I use $\alpha_f = 0.075 \pm 0.015$ for a non-point-source fountain. The value $\alpha_f = 0.075$ is within the uncertainty of Bloomfield & Kerr's (1998) estimate.

2.4.3 Penetrative entrainment rate of a fountain at a density interface

As discussed in §1.4.1, the penetrative entrainment refers to the entrainment by the fountain that brings a certain amount of upper zone warm fluid to the lower occupied zone. Experiments suggest that the entrainment rate of ambient fluid into the fountain at the interface changes with the local Richardson number Ri. At low Richardson numbers the entrainment rate is a constant between $0.55 \sim 0.65$ (Lin 2003). At higher Richardson number, the entrainment rate is a decreasing function of Ri (Ri^{-1} or $Ri^{-3/2}$). Here, we assume that E is proportional to Ri^{-1}. Then we need find the critical Richardson number Ri_c where the entrainment rate E starts to decrease with Ri since this is the only free parameter to determine E.

In figure 2.8, I have plotted the penetrative entrainment rate E vs. the interface Ri of my experiments. The entrainment rate E was selected when the value provides good agreement for the experimental data and the theoretical estimates. Those data shown in figure 2.8 suggests a formula of the penetrative entrainment rate at different range of Ri

$$E = \begin{cases} 0.6 \pm 0.1 & \text{if } Ri \leq 8 \\ 4.8\, Ri^{-1} \pm 0.1 & \text{if } Ri > 8 \end{cases} \tag{2.11}$$

It implies that at low Richardson numbers the entrainment rate tends to be a

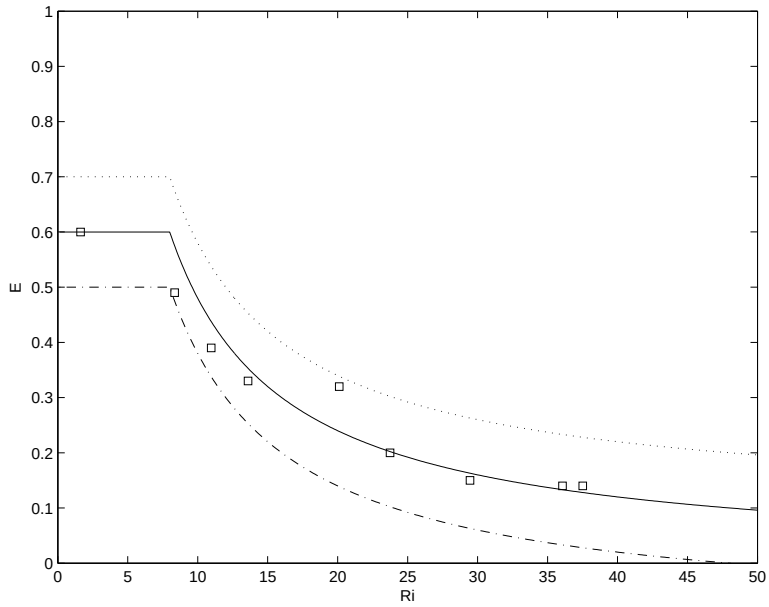

Figure 2.8: Empirical formula for penetrative entrainment rate. Experiments were shown in squares. Dotted line and dash-dot line are the upper and lower bounds in the empirical formula (2.11).

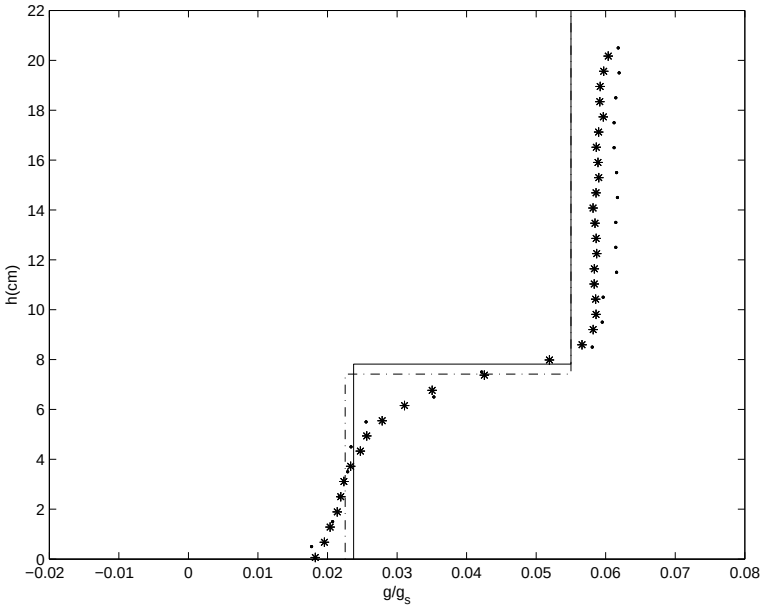

Figure 2.9: The theoretical model provides different estimates according to different critical Richardson numbers. $Ri_c = 8$ for the solid line. $Ri_c = 3$ for the dash-dot line. Dots and stars are experimental measurements.

constant, as found by Lin (2003). At higher Richardson numbers, when the density difference between the upper and lower zones is larger, the entrainment rate E is proportional to Ri^{-1}. Note that the constant value 0.56 given by Kumagai's (1984) empirical formula (1.43) is consistent with my formula.

Although my experimental data is not sufficient to verify (2.11), the formula works throughout this research. Figure 2.9 shows that different Ri_c did not make a big difference in the theoretical predictions.

2.4.4 Implementation

The object of the numerical model is to find the interface and temperatures in two layers that make the conservation laws valid in a UFAD system. The model has been programmed by using MATLAB. The fountain model (§2.4.1) was implemented as a subfunction to return the interface volume flux Q_i in the

fountain and the Richardson number Ri at the interface. Given the initial conditions of a fountain flow, the dimensionless governing equation (2.3), (2.4) and (2.5) can be solved using a routine based on a fourth-order Runge-Kutta method. This method is reasonably simple and robust given a small step. The penetrative entrainment Q_e is then determined by (1.39) and (2.11). The entrainment rate α_f for the fountain is in the range 0.075 ± 0.015 and the entrainment rate α for the plume is chosen to be 0.117.

Chapter 3

The Interior Zone Model — Single Source & Multiple Diffusers

In this chapter, we present experiments and develop a theoretical model of a UFAD system containing multiple cooling diffusers (figure 3.1 (b)) and a single heat source located at different heights above the floor(figures 3.1 (c) and (d)).

3.1 Theoretical Model about Multiple Cooling Diffusers

3.1.1 Fixed heat load and total ventilation rate

In this, and the next section, we discuss the effect of multiple diffusers. Consider a single UFAD space (figure 3.2), with a constant heat load B and total ventilation rate Q, at steady state. We assume that all cooling diffusers are identical. Since the flow through them is driven by the (assumed spatially uniform) plenum pressure, the flow from each diffuser Q_f is also the same [1]. At the interface height h, the plume and each fountain carry a volume flux Q_p and Q_i, respectively.

[1]Some commercial diffusers can be controlled by individual occupants, e.g. by partially closing the vent. In this case the different flows above each diffuser produces horizontal variations that are beyond the scope of this study.

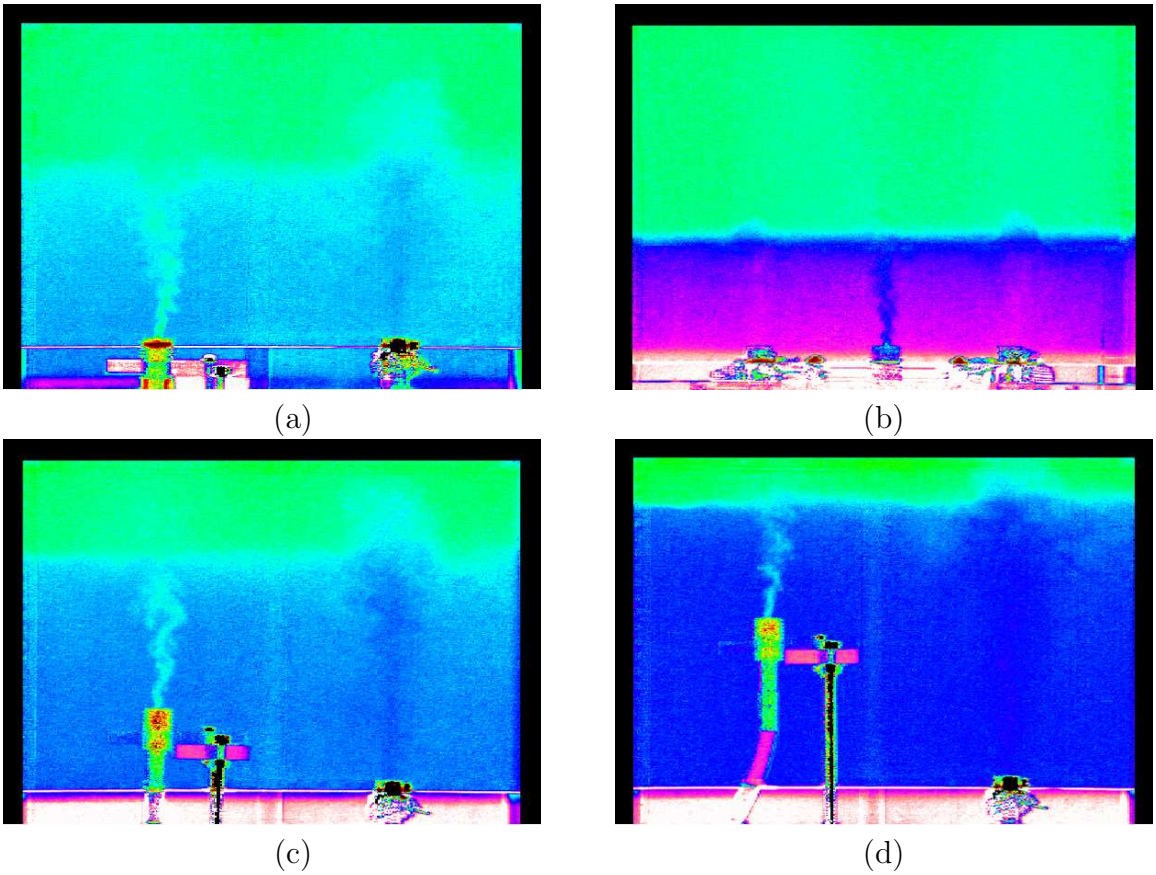

Figure 3.1: False colour images of the laboratory experiments in which water is used as the working fluid and saline and fresh water plumes and jets are used to represent thermal plumes and the flow from a cooling diffuser. The images have been inverted to represent the orientation appropriate to building ventilation (§ 2). (a) The basic case of one heat source and a single diffuser. (b) One heat source and two diffusers. (c) An elevated heat source at $1/4H$. (d) An elevated heat source at $1/2H$. In (c) and (d), the plume nozzle was fixed in the tank by a supporting bar. The effect of additional diffusers, for a given total flow rate, is to reduce the interface height and reduce the lower layer temperature, while raising the heat source above the floor raises the interface and and reduces the lower layer temperature.

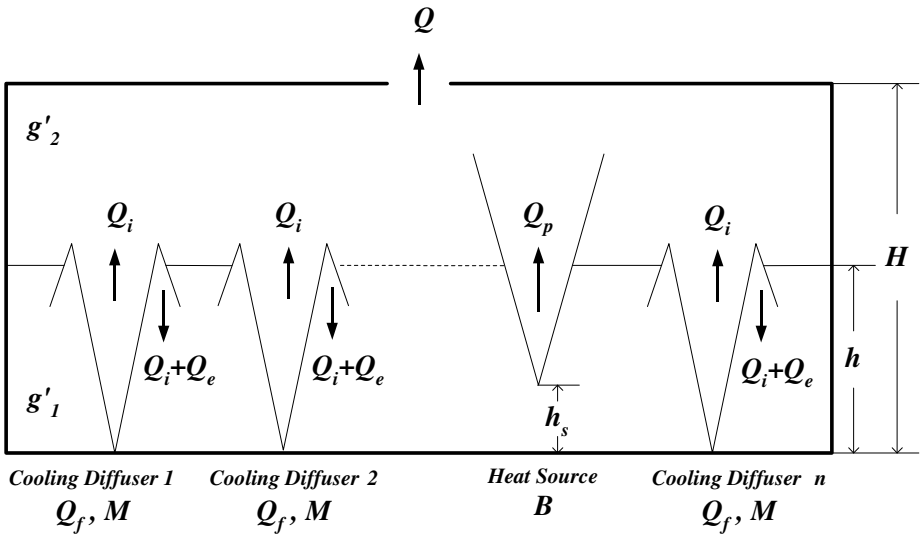

Figure 3.2: A UFAD model with a single heat source and multiple equal cooling diffusers. The vertical height of the heat source is h_s, and in the discussion of multiple diffusers is restricted to the case of the heat source on the floor ($h_s = 0$).

The plume volume flux is given by (1.21) at $z = h$. An amount of upper layer fluid Q_e is entrained back into the lower layer by the fountain above each cooling diffuser, leaving a net flow rate Q through the system.

Here we consider the effect of distributing the same total ventilation air among different numbers of diffusers. This calculation is important in the design of a UFAD system, where the optimal number of diffusers for a given space needs to be decided. We begin by supposing that the ventilation flow Q, originally supplied through one diffuser is now divided equally among n diffusers ($Q_f = \frac{1}{n}Q$). Since the momentum flux from an individual diffuser is proportional to Q_f^2, the momentum flux for each diffuser is $1/n^2$ of that of a single diffuser carrying the same ventilation flow. Hence, as more diffusers are opened, the fountain from each diffuser is weaker and the total entrainment of upper layer fluid into the lower layer will be reduced.

Since the vertical transfer of fluid across the stable interface can only take place within the plume, in steady state, conservation of volume flux gives

$$Q_p = n(\frac{1}{n}Q + Q_e), \tag{3.1}$$

In a steady state, the buoyancy flux carried out through the exit is equal to the buoyancy flux produced in the space by the heat source B since all walls are adiabatic, so that

$$g_2' = \frac{B}{Q}, \tag{3.2}$$

According to (3.2), the steady-state reduced gravity g_2' of the upper layer and, therefore, the return temperature (assumed here to the same as the upper layer temperature) depends only on the total heat load and the total ventilation rate for the space, and is independent of the number of (and the properties of the) cooling diffusers – a consequence of no heat losses.

The reduced gravity of the lower layer g_1', is determined by the fluid entrained by the cooling diffusers from the upper layer. We assume that this fluid is mixed uniformly throughout the lower layer, so the buoyancy conservation in the lower layer gives

$$(nQ_i - Q)g_1' + Q_p g_1' = (nQ_i - Q)g_1' + nQ_e g_2' + Qg_f', \tag{3.3}$$

where g_f' is the buoyancy of the diffuser flow. In the following, the reference density is chosen so that $g_f' = 0$, and all temperatures are relative to the supply temperature(taken as $T_s = 0$) . Therefore,

$$g_1' = \frac{g_2' Q_e}{Q_e + \frac{1}{n}Q}. \tag{3.4}$$

Hence

$$\frac{g_1'}{g_2'} = \frac{nQ_e}{nQ_e + Q}. \tag{3.5}$$

When n increases, the interface decreases so that Q_p decreases; thus, the total entrainment nQ_e decreases according to (3.1). Since the upper layer buoyancy

(the return temperature) g_2' does not change with n, the lower layer temperature g_1' will decrease as n increases. The total entrainment $nQ_e \to 0$, when $n \to \infty$ in which case the fountain diffuser flow entrains no air from the upper layer to the lower layer. Therefore, according to (3.5), $g_1' \to 0$ as $n \to \infty$ and the lower layer temperature equals the supply temperature. This limit recovers displacement ventilation in which the supply air enters the space without mixing.

3.1.2 Fixed heat load and underfloor pressure

In this section we continue the discussion of the effect of different numbers of diffusers. Here we are considering a functioning UFAD system with the underfloor plenum held at a fixed pressure and consider the effect of the occupants opening or closing diffusers to change the total number in operation. In this case, as more diffusers are opened, the total amount Q of air supplied to the room increases since $Q = nQ_f$, while the strength of each diffuser flow remains constant.

In this case, the equations (3.1), (3.2) and (3.4) become

$$Q_p = n(Q_f + Q_e), \tag{3.6}$$

$$g_2' = \frac{B}{nQ_f}, \tag{3.7}$$

$$g_1' = \frac{g_2' Q_e}{Q_e + Q_f}. \tag{3.8}$$

These equations show that, as more diffusers are opened and n increases, Q_p increases and the interface position is raised, and the upper layer buoyancy (the return air temperature) decreases, since $g_2' \sim \frac{1}{n}$. Further, since Q_f is constant with n, the lower zone temperature g_1' gets cooler as g_2' decreases. At the limit when $n \to \infty$, according to (3.7), $g_2' \to 0$, and $g_1' \to 0$ as a result from (3.8). The two-layer stratification disappears, and a uniform temperature at the supply air temperature is obtained. In this case, the limit as $n \to \infty$ is to mixing ventilation

caused by the large ventilation rate, with consequent loss of energy-efficiency. Such a system is said to be 'over-aired'.

3.1.3 An elevated heat source

Heat sources, such as lamps or computers, are usually not located on the floor. Even the thermal effect of a human may be considered as a plume rising from the upper part of the body, rather than from the feet. Here we study the effects of vertical locations of a heat source in a UFAD system, and introduce the vertical height h_s of the plume source as a parameter (figure 3.2).

The conservation relations (3.1), (3.2) and (3.4) remain valid. As discussed in §1.3.1, the volume flux Q_p in the plume at the density interface is related to the buoyancy flux B of the heat source and the distance of the interface from the source origin, which now is $h - h_s$, so

$$Q_p = C\left[B\left(h - h_s\right)^5\right]^{1/3}. \tag{3.9}$$

The effect of raising the heat source off the floor is to decrease the length of the plume over which entrainment can occur, and so compared to a heat source on the floor, the interface rises to provide the required volume flux Q_p. Since, changing the vertical position of the heat source does not change B or Q, the temperature of the upper layer remains the same. Further, since the velocity in all diffusers decreases with height, the stability of the interface increases as h_s increases. Consequently, the interfacial Richardson number Ri increases, and the entrainment rate E decreases, and the diffuser flows bring less upper-layer fluid to the lower layer, i.e. nQ_e is smaller. According to (3.4) the lower cooled zone temperature g_1' drops.

Exp. No.	B (cm^4s^{-3})	M (cm^4s^{-2})	Q_f (cm^3s^{-1})	No. of Diffusers	Tank Label
1	70.1	142	13.4	1	A
2	71.8	35.4	6.70	2	A
3	69.3	182	15.2	1	A
4	68.2	45.5	7.60	2	A
5	69.3	58.2	8.60	2	A
6	69.3	74.1	9.70	2	A
7	70.1	26.3	5.00	3	B
8	70.9	44.5	6.50	3	B

Table 3.1: 8 different experimental conditions for the multiple diffusers experiments. B is the buoyancy flux of the heat source, M and Q_f are the momentum fluxes and the volume fluxes of each cooling diffuser.

3.2 Experimental results & comparisons with the model predictions

Experiments were carried out with buoyancy fluxes B of the plume around 70 cm^4s^{-3} and the momentum fluxes M of the fountains varied from 25 to 243 cm^4s^{-2}. The plume and fountains were observed to be fully turbulent. The experimental conditions for each run with $h_s = 0$ were summarized in Table 3.1. The effects of an elevated heat source ($h_s \neq 0$) was investigated by changing the vertical position of the heat source for the parameters of Exp. 3.

A plume rising from a heat source (unless it is a convector heater with a fan, say) has zero volume flux Q_s and momentum flux M_s at the source. The effects of the non-ideal plume initial conditions can be corrected by introducing a virtual origin as discussed in §1.3.2. The virtual origin of the plume z_v for our experiments, determined by (1.32), ranges from 1.0 to 1.3 cm, which is small compared with the depths of the tanks.

The second effect of representing a heat source by a finite volume flux Q_s of salt solution with buoyancy g'_s, is that the buoyancy flux is $B = Q_s(g'_s - g'_1)$. Since g'_1 is not known *a priori*, the buoyancy flux needs to be calculated at the end of the experiment. Then the volume flux in the plume Q_p at the density interface,

is given by

$$Q_p \;=\; C\left[B\left(h+z_v\right)^5\right]^{1/3}. \tag{3.10}$$

Finally, the finite plume-source volume flux contributes to the overall volume flow through the tank. Hence, $Q \;=\; nQ_f + Q_s$. In the experiments $Q_s \approx 0.85\text{cm}^3/\text{s}$, which is less than 6% of the total volume flow rate through the tank, and always significantly less than Q_p at the interface. Thus, this small addition of volume does not affect the flow significantly, and we take it into account (by inclusion through conservation equations) in all comparisons between the theory and the experiments throughout this research.

The fountains are calculated by the numerical model discussed in §2.4.1.

3.2.1 Effects of multiple diffusers

The experiments with one or two diffusers were carried out in the smaller tank #A, and three diffusers in the larger tank #B. All these experiments have a single plume on the floor. In the following graphs, solid lines or '$\circ$' indicate the theoretical predictions, '$*$' are the experimental measurements obtained from dye concentration, and '$\cdot$' are the measurements of fluid samples. We define a dimensionless height

$$\hat{z} = \frac{z}{C^{-3/5}Q^{3/5}B^{-1/5}}, \tag{3.11}$$

where $C = 0.142$ is the universal plume constant and a dimensionless buoyancy

$$T/T_R \equiv \hat{g}' = \frac{g'Q}{B}. \tag{3.12}$$

Hence, $\hat{h} = 1$ corresponds to the interface height at which all the ventilation flow is carried by the plume (1.21), and $\hat{g}' = 1$ corresponds to the return temperature given by (3.2).

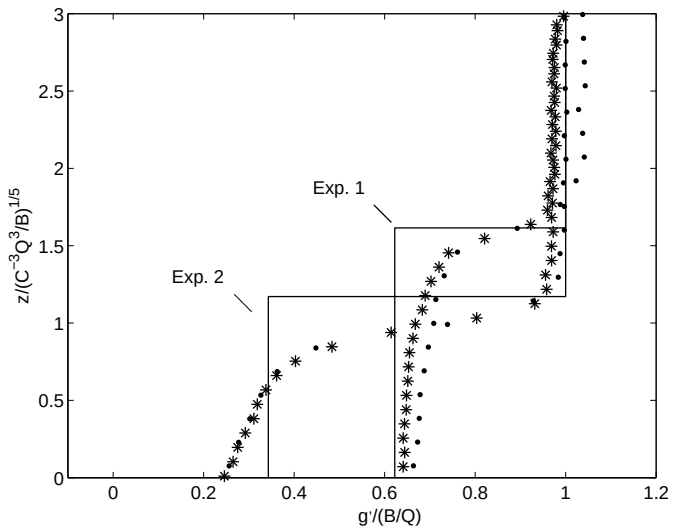

(a)

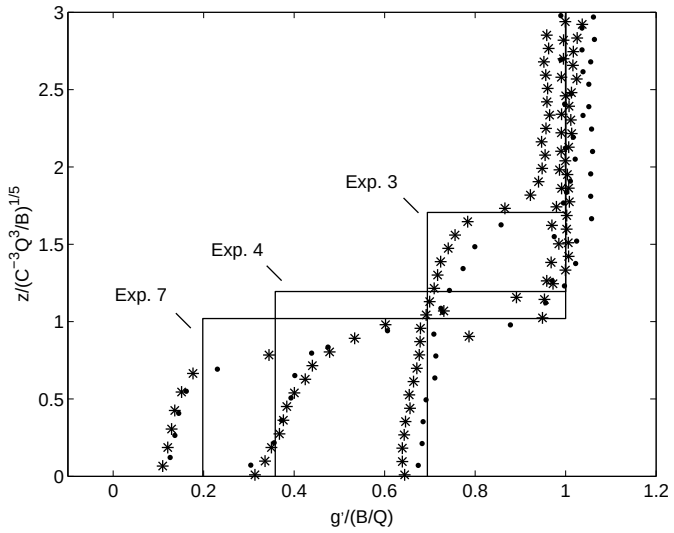

(b)

Figure 3.3: Buoyancy profiles obtained at steady state with multiple diffusers with fixed heat load and ventilation rate. The height is made dimensionless by the height scale $C^{-3/5}Q^{3/5}B^{-1/5}$ based on the total ventilation rate and buoyancy flux, and the buoyancy by the buoyancy scale B/Q. (a) Exp. 1 with a single diffuser and Exp. 2 with two diffusers; (b) Exp. 3 with one diffuser, Exp. 4 with two diffusers and Exp. 7 with three diffusers.

The first case concerns the behaviour when the number of diffusers increases, but the total ventilation rate remains unchanged. Exp. 1 and Exp. 2 (table 3.1) have almost the same plume buoyancy fluxes and total ventilation rate Q, while Exp. 2 has two cooling diffusers which split the total volume flux of the single diffuser in Exp. 1. In figure 3.3(a), we see that a two-layer temperature stratification forms in both cases, although there is some weak stratification in the lower layer. The upper layer temperature remains approximately the same, at the predicted return temperature $\hat{g}' = 1$, (3.2). When the ventilation flow is split between two diffusers, the lower layer temperature and the interface height both decrease. The theoretical predictions of the upper layer temperature and the interface position have the same behaviour, and they agree well with the experimental data. However, the lower layer in Exp. 2 is more stratified than in Exp. 1 because, in the experiments, it is difficult to obtain exactly the same flow from each diffuser. Consequently, one diffuser might entrain more upper warm-layer fluid than the other, thereby producing slightly different downward heat fluxes at each diffuser and producing some weak stratification. However, this was always observed to be a relatively small effect, and the density in the lower layer is fairly uniform. The experimental data confirm the theoretical predictions of §3.1.1 that the interface height and the lower layer temperature decrease as the number of diffusers increases.

Note further that the dimensionless interface height in Exp. 1 is $\hat{h} \approx 1.6$, and this value is reduced to $\hat{h} \approx 1.2$ in Exp. 2. Values above the theoretical value of $\hat{h} = 1$, at which all the ventilation flow is carried by the plume, are a result of entrainment of upper layer fluid back down into the lower layer. Further, since $Q \sim h^{5/3}$, this change shows that splitting the ventilation flow between the two diffusers reduces the total entrainment by a factor of about 7, which is caused by a reduction in the momentum flux of each diffuser to about one-quarter of that of a single diffuser. This sensitivity to the diffuser flow shows the importance of the penetrative entrainment from the upper layer. The reduction in the lower

layer temperature is also a consequence of the decreased total entrainment from the upper layer. figure 3.3(b) shows the effect of changing the number of diffusers from 1 to 3, again at the same heat load and ventilation flow rate. The same trends for variations in temperature in both layers and the interface position with increasing number of diffusers were observed and there is good agreement with the theoretical model.

In these cases, the interface position measured in the experiments falls below the theoretical value. The entrainment rate E, given by (2.11), is tuned to the case of a single diffuser and, as can be seen in these figures, the agreement is best for these cases (Exp. 1 and Exp 3). The lower layer temperature is well predicted in each case.

The second case where the underfloor pressure remains fixed, so that increasing the number of diffusers increases the total ventilation flow rate Q, is shown in figure 3.4, which compares Exp. 2 and Exp. 8. The two experiments have almost the same buoyancy flux B from the heat source, and volume flux Q_f from each diffuser. In figure 3.4(a), the profiles are non-dimensionalised using B and Q_f, and as these are fixed, the changes in the profiles reflect those observed in the physical variables. We observe that, with increasing number of diffusers and, consequently, increasing Q, the temperature in both layers decreases and the interface height increases, as expected from the model described in §3.1.2. Quantitative agreement with the model is also found in this case. In figure 3.4(b), the profiles are non-dimensionalised by the total ventilation rate Q, and the profiles collapse on to a single curve. The use of Q ensures that the dimensionless return temperature $\hat{g_2'} = 1$. The dimensionless occupied zone temperature $\hat{g_1'}$ can be obtained using (3.6), (3.7) and (3.8)

$$\hat{g_1'} = \hat{g_2'} \frac{Q_e}{Q_e + Q_f} = \hat{g_2'}(1 - \frac{nQ_f}{Q_p}), \tag{3.13}$$

and the dimensionless interface height

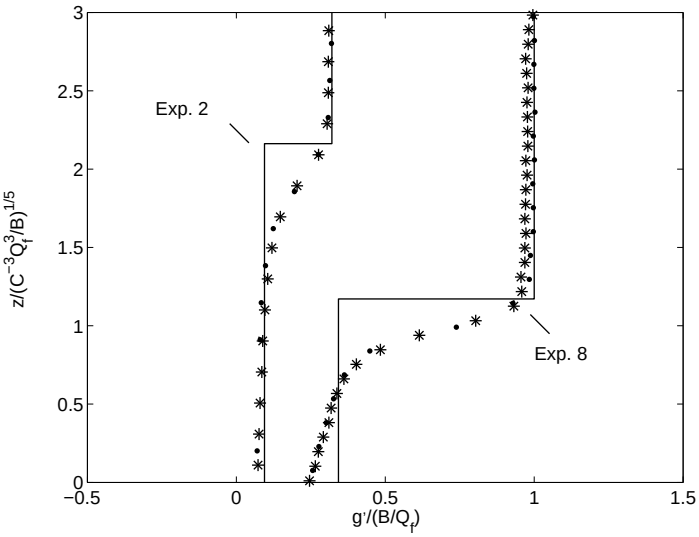

(a)

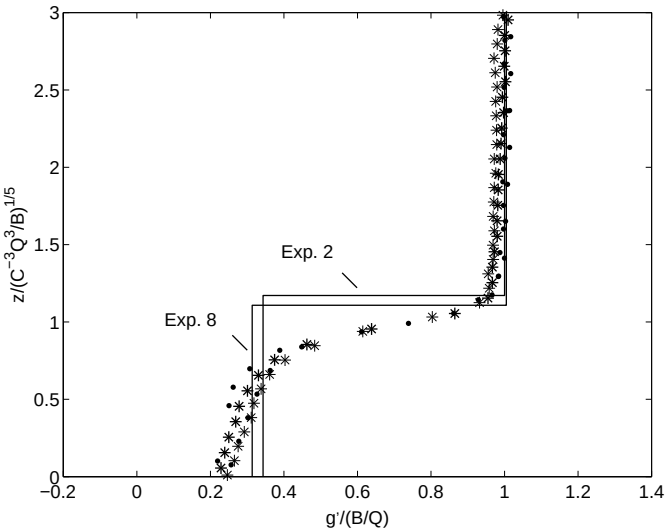

(b)

Figure 3.4: Dimensionless buoyancy profiles obtained at steady state with multiple diffusers for fixed heat load and underfloor pressure; Exp. 2 with 2 diffusers and Exp. 8 with 3 diffusers. (a) The buoyancy non-dimensionalized with the volume flux Q_f from each diffuser. (b) The buoyancy non-dimensionalized with the total ventilation volume flux Q.

$$\hat{h} = \frac{h}{C^{-3/5}(nQ_f)^{3/5}B^{-1/5}}. \tag{3.14}$$

Therefore, both $\hat{g_1'}$ and $\hat{h}$ are constant, if $h \sim n^{\frac{3}{5}}$, a result we will derive later.

The theoretical predictions of the dimensionless buoyancy profiles, for a fixed heat load with different numbers of cooling diffusers, are shown in figure 3.5. Figure 3.5(a) shows profiles for fixed total ventilation flow rate, but with the supply air divided equally between n diffusers, as discussed in §3.1.1. As we can see in this figure, the upper layer buoyancy (i.e. the return temperature) remains constant. When $n = 1 \sim 4$, the interface descends and the lower layer temperature decreases rapidly with increasing n. When $n \geq 5$, the effect of additional diffusers on the interface position and the lower layer density is minimal. For these large numbers of diffusers, the entrainment of upper layer fluid becomes negligible, and the system operates as a displacement ventilation system with no appreciable mixing of the supply air. Hence, the lower layer temperature approaches the supply temperature ($g'_1 = 0$), and the interface height approaches that at which the plume carries the total ventilation rate ($\hat{h} = 1$), as $n \to \infty$.

Figure 3.5(b) shows the buoyancy profiles given the same heat load and underfloor pressure, but with the total ventilation rate increasing with n, as discussed in §3.1.2. In this case, we observed a decrease in temperature in both layers, and a higher interface as n increases. In the limit of large n, the increase in the ventilation flow rate destroys the stratification, and mixing ventilation occurs.

In order to calculate the effects of changing the number of diffusers, we examine the two cases as n varies. Consider, first, the case where the total ventilation flow rate is held fixed. Figure 3.6 shows (a) the dimensionless interface height $\hat{h}$ and (b) the dimensionless buoyancy difference, plotted against n. As expected, $\hat{h}$ decreases with increasing n, approaching the displacement limit $\hat{h} = 1$ at large n, and the buoyancy difference increases to $\hat{g_2'} - \hat{g_1'} = 1$ for large n. For small values of $n \leq 4$, $\hat{h}$ and $(\hat{g_2'} - \hat{g_1'})$ vary as $n^{-0.5}$ and $n^{0.8}$, respectively, as n increases. In order to understand these trends we present some scaling relations.

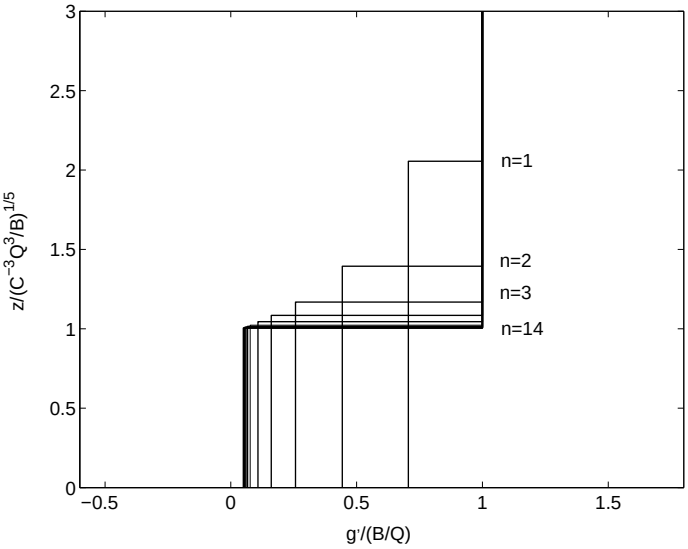

(a)

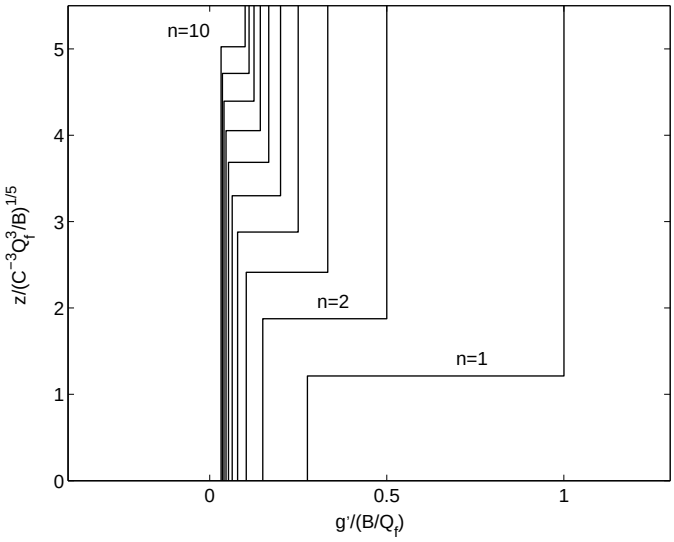

(b)

Figure 3.5: (a) Theoretical predictions for n equal cooling diffusers in the conditions of constant ventilation flow rate, $n = 1$, ..., 14; (b) Theoretical predictions for n equal cooling diffusers in the conditions of constant under floor pressure, $n = 1$, ..., 10.

We assume that the virtual origin of the plume z_v is small compared to the height of the interface h. From (3.10), for a fixed heat load, $Q_p \sim h^{\frac{5}{3}}$. As a first approximation, we further assume that the diffuser flow acts like a jet, so that the momentum flux M of the fountain is conserved. Dimensional analysis shows that at each height z, the mean vertical velocity w, the radius b of the fountain, and the volume flux Q are given by

$$w \sim M^{\frac{1}{2}} z^{-1}, \quad b \sim z \quad Q \sim wb^2 \sim M^{\frac{1}{2}} z. \tag{3.15}$$

Since $M \sim n^{-2}$ when the total ventilation rate is fixed, the volume flux of the diffuser flow and the Richardson number at interface are $Q_i \sim \frac{Qh}{n}$, and $Ri \sim \frac{g' h^3 n^2}{Q^2}$, respectively.

Experiments suggests that the interfacial Richardson number is in the region where $E \sim \frac{1}{Ri}$. Therefore, $Q_e \sim \frac{Q^3}{g' h^2 n^3}$, and (3.1) becomes

$$c_1 h^{\frac{5}{3}} = c_2 + \frac{c_3}{n^2 h^2}, \tag{3.16}$$

where, c_1, c_2 and c_3 are constants. Approximately, (3.16) can be written as

$$c_1' \hat{h}^2 \approx c_2' + \frac{c_3'}{n^2 \hat{h}^2}. \tag{3.17}$$

The quadratic (3.17) has the non-trivial root $\hat{h}^2 = \frac{c_2' + \sqrt{c_2'^2 + 4c_1' c_3'/n^2}}{2c_1'}$. Therefore, when n is large, $\hat{h} = \sqrt{c_2'/c_1'}$ implies that the interface height is independent of n. More precisely, (3.1) reduces to $Q_p = Q$, so $\hat{h} = 1$ when n is large. On the other hand, when n is small,$4c_1' c_3'/n^2 \gg c_2'^2$. Hence, $\hat{h} \sim n^{-\frac{1}{2}}$.

The non-dimensional density difference $\hat{g_2'} - \hat{g_1'} = \frac{Q}{Q_p}$ and, therefore, is independent of n, at large values of n, as observed. With small n, $(\hat{g_2'} - \hat{g_1'}) \sim \hat{h}^{-\frac{5}{3}} \sim n^{\frac{5}{6}}$. The observed power laws $\hat{h} \sim n^{-0.5}$ and $(\hat{g_2'} - \hat{g_1'}) \sim n^{0.8}$ shown in figure 3.6(a) and (b), respectively, although based on a fit to only a few points, are consistent with above scaling.

We now turn to the second case where the underfloor plenum pressure is held fixed. Since, in this case the flow across each diffuser is fixed, we replace Q

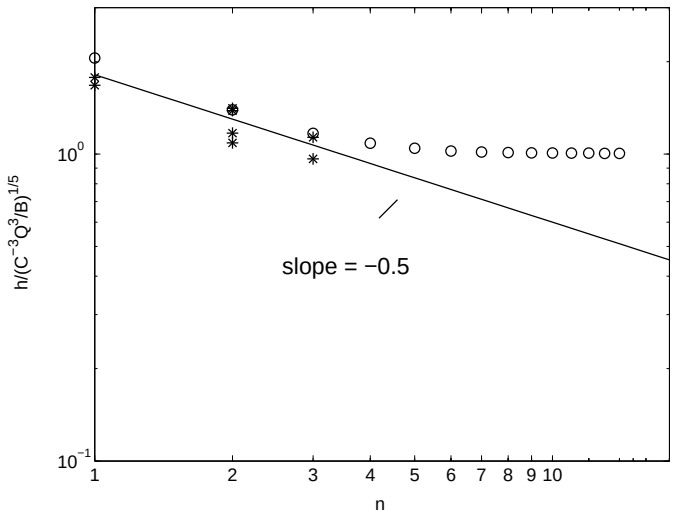

(a)

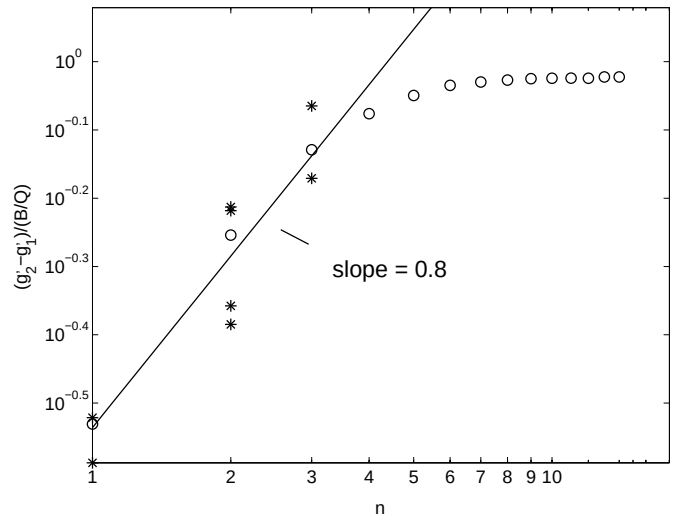

(b)

Figure 3.6: (a) The dimensionless interface height $\frac{h}{(C^{-3}Q^3/B)^{1/5}}$ and (b) the non-dimensional density difference between two layers $\frac{g_2'}{B/Q} - \frac{g_1'}{B/Q}$ plotted against the number of diffusers n when the total ventilation rate is fixed. The stars are the experimental results and the open circles are the results from the model.

by Q_f in (3.11) and (3.12), so that the dimensionless height is

$$\hat{z_f} = \frac{z}{C^{-3/5}{Q_f}^{3/5}B^{-1/5}}, \tag{3.18}$$

and a dimensionless buoyancy

$$\hat{g'} = \frac{g'Q_f}{B}, \tag{3.19}$$

so that $\hat{g_2'} = 1$ corresponds to the single-diffuser case ($n = 1$), where $Q_f = Q$.

As before, when n is large, $nQ_e \ll Q_p$ and $Q_p = nQ_f$ from (3.6). Since Q_f is a constant, $\hat{h} \sim n^{\frac{3}{5}}$. If n is small, nQ_f and nQ_e are comparable. Then, $Q_p = ncQ_f$, where, c is a constant. So, again, $\hat{h} \sim n^{\frac{3}{5}}$ and, consequently $\hat{h} \sim n^{\frac{3}{5}}$. Thus, this analysis shows that the dimensionless stratifications are the same using the definitions of dimensionless height and temperature, (3.11) and (3.12), based on Q, in agreement with the results shown in figure 3.4(b). The dimensionless density difference between two layers is obtained, using (3.19), as $\hat{g_2'} - \hat{g_1'} = \frac{Q_f}{Q_p}$. Therefore, $(\hat{g_2'} - \hat{g_1'}) \sim \hat{h}^{-\frac{5}{3}} \sim n^{-1}$.

The experimental results and model predictions are shown in figure 3.7, where the dimensionless interface height and the dimensionless buoyancy are plotted logarithmically against n. The best line fits show that $\hat{h} \sim n^{0.5}$ and $(\hat{g_2'} - \hat{g_1'}) \sim n^{-0.8}$. These results are reasonably consistent with the above scaling analysis.

3.2.2 Effects of an elevated heat source

Figure 3.8, shows the experimental results from four experiments with identical conditions except for different heights of the heat sources. These experiments were restricted to a single plume and a single diffuser. We use a new dimensionless height $\hat{z} = z/H$, since the source height relative to the room height scale H is a significant parameter.

Following the same strategy of scaling analysis in §3.2.1, (3.1) becomes

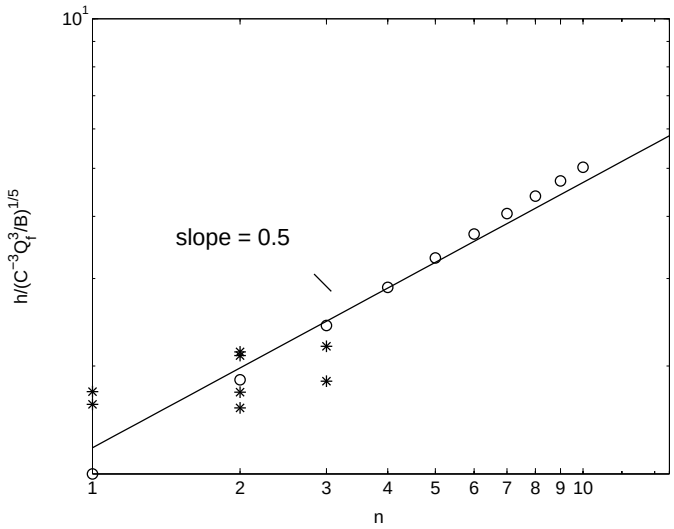

(a)

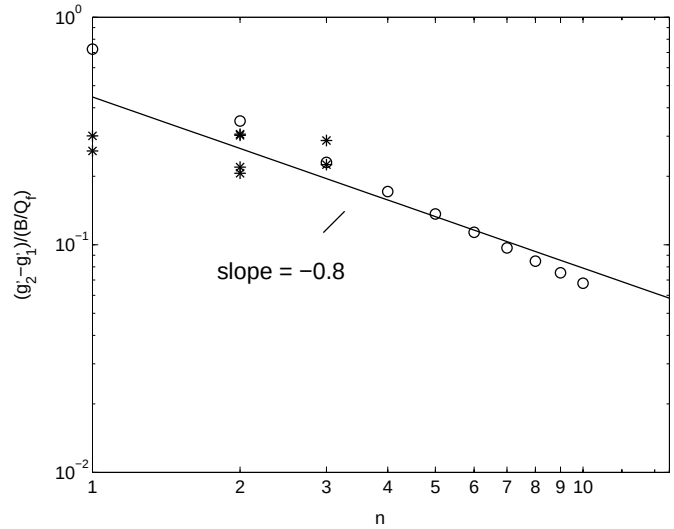

(b)

Figure 3.7: (a) The dimensionless interface height $\frac{h}{(C^{-3}Q_f^3/B)^{1/5}}$ and (b) the non-dimensional density difference $\frac{g_2'}{B/Q_f} - \frac{g_1'}{B/Q_f}$ plotted against n with fixed underfloor pressure. The stars are the experimental results and the open circles are the results from the model.

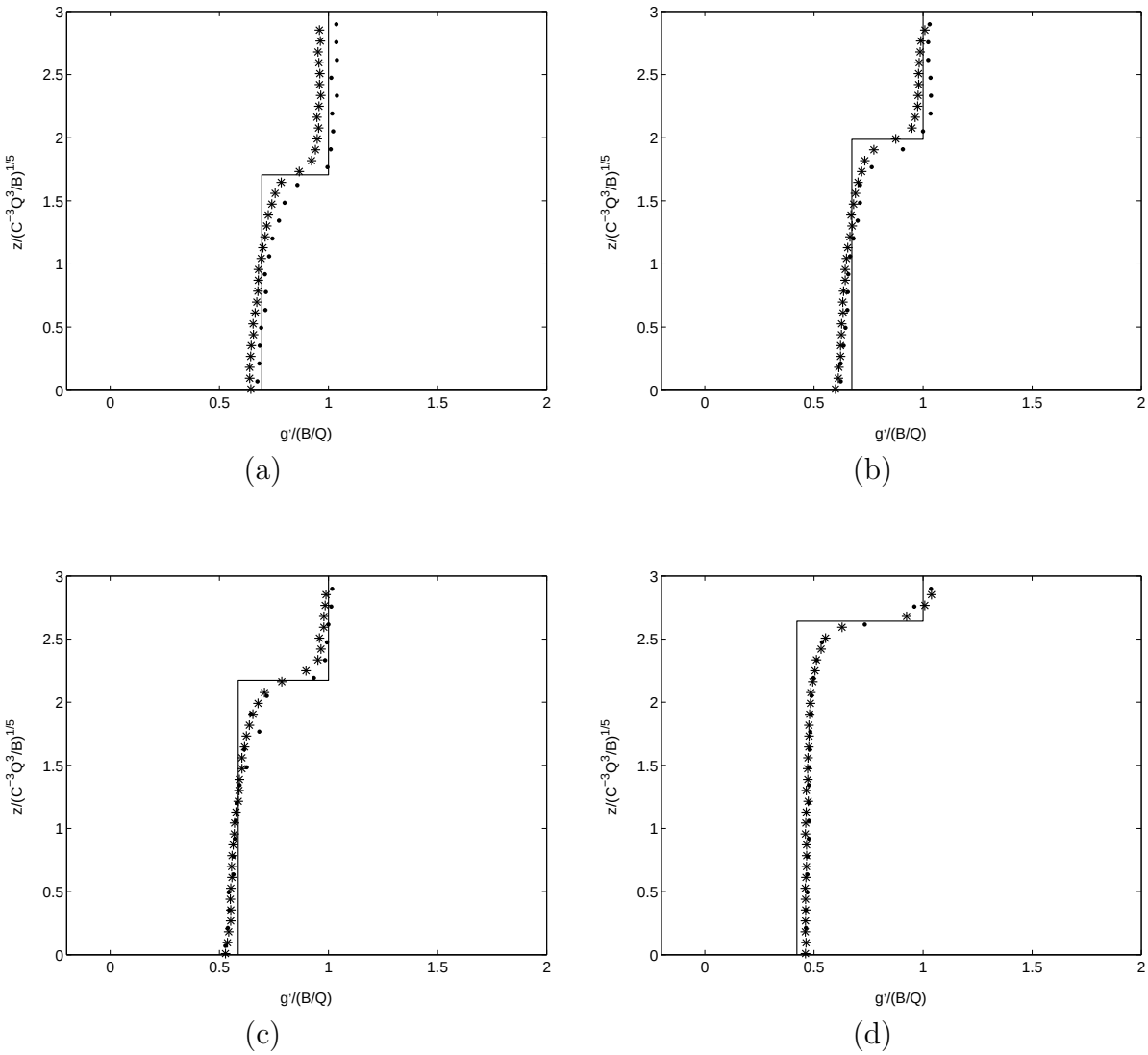

Figure 3.8: Experiment Exp. 3 with its heat source (a) on the floor; (b) at $1/8H$; (c) at $1/4H$; (d) at $1/2H$.

$$\hat{h} - \hat{h_s} \approx c_2^{''} + \frac{c_3^{''}}{\hat{h}}. \tag{3.20}$$

When $\hat{h_s} \ll c_2^{''}, c_3^{''}$, the quadratic (3.20) has the roots $\hat{h} = \frac{1}{2}\hat{h_s} + c_2^{'''}$, where $c_2^{''}$, $c_3^{''}$ and $c_2^{'''}$ are constants. Therefore, the effect of an elevated heat source is to produce a linear increase in the interface height, by about one-half the height of the heat source. A least-square fit to the experimental data is $\hat{h} = 0.6\hat{h_s}$, as shown in figure 3.9(a).

Using (3.12), the non-dimensional density difference between two layers $\hat{g_2^{'}} - \hat{g_1^{'}} = \frac{Q_f}{Q_p} \sim (\hat{h} - \hat{h_s})^{-\frac{5}{3}}$. The experiments in figure 3.9 show that $(\hat{g_2^{'}} - \hat{g_1^{'}}) \sim (\hat{h} - \hat{h_s})^{-1.6}$, consistent with this scaling.

3.3 Conclusions

The simplest model of a UFAD system consists of a single heat source and a single diffuser. The performance of the whole system depends on entrainment: entrainment into the rising plume above the heat source, entrainment into the negatively-buoyant jet above the diffuser, and finally penetrative entrainment of upper-zone high-temperature air into the lower zone as the diffuser flow reverses and falls downwards. Perhaps somewhat surprisingly, provided the diffuser flow has a positive vertical momentum, it always rises high enough to impact the interface, and there is some non-zero penetrative entrainment. Only in the limit of displacement ventilation, where the supply to the lower layer has no vertical momentum, is there zero penetrative entrainment. Then, of course, all the lower zone is at the supply temperature, and the input fluid is neutrally buoyant. Any vertical momentum in this limit will allow the diffuser flow to cross the lower zone until it reaches the warmer upper zone. Thus the controlling feature of the system is the magnitude of the penetrative entrainment E.

The behavior of UFAD enclosures containing multiple cooling diffusers has been investigated both experimentally and theoretically. A model of Lin &

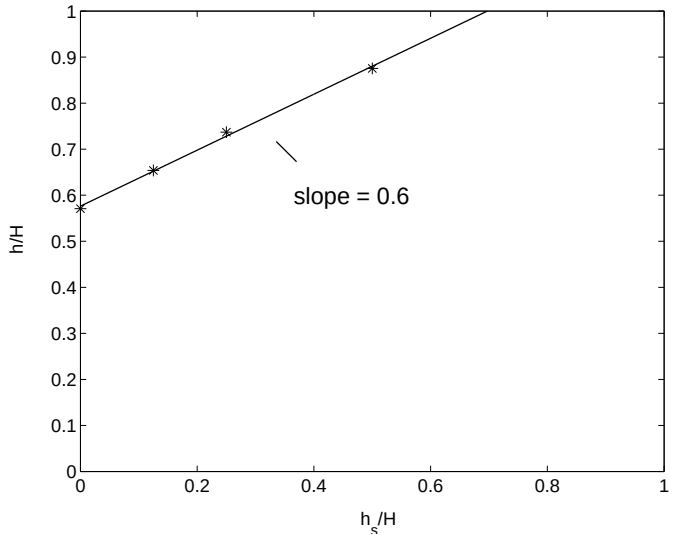

(a)

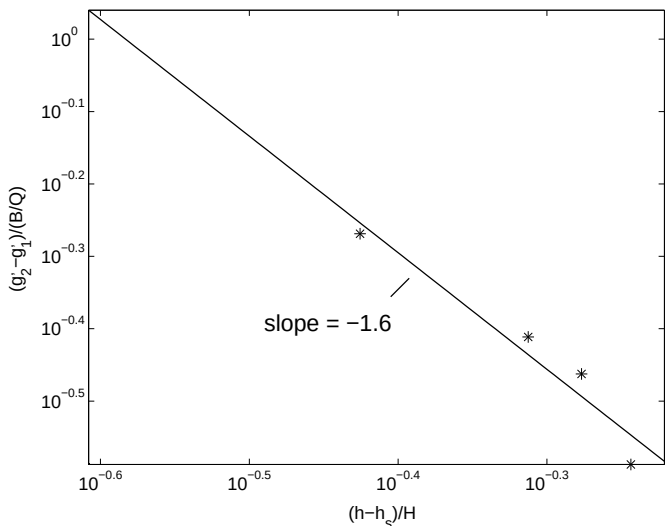

(b)

Figure 3.9: (a) The dimensionless interface height $\frac{h}{H}$ changes with $\frac{h_s}{H}$ linearly; (b) The dimensionless buoyancy difference between the two layers $\frac{g_2'}{B/Q} - \frac{g_1'}{B/Q}$ changes with $\frac{h-h_s}{H}$.

Linden (2005) for a single plume and single diffuser, in which it is assumed that a two-layer stratification forms, has been extended to predict the room stratification and gives good agreement with the experimental measurements for the layer temperatures and the interface heights.

The basic rules that govern the interface height and the temperatures of the two layers as functions of the number of diffusers in multi-diffuser systems, or with the heat source position in elevated-source model, have been determined by scaling analysis and verified by the experiments. These rules link our extended model to the work of Lin & Linden (2005) quantitatively, and allow the determination of the stratification for any number of diffusers, or for any vertically positioned heat source in elevated-source systems.

In terms of design, these rules are helpful in determining the optimized number of diffusers. In order to do so we divide a space into subregions with one plume in each. Consider, for example, the situation where the total number of diffusers needs to be estimated for the subregion with a given heat load and ventilation flow rate. It may be appropriate that for cost reasons, the number of diffusers should be minimized. The limit of this case is displacement ventilation, $\hat{g_2'} - \hat{g_1'} = 1$, when n is a large. We find the intersection of this point with the scaling law $\hat{g_2'} - \hat{g_1'} \sim n^{0.8}$, as shown in figure 3.10. Thus, the crossing point gives the optimized number $n = 4$, of diffusers per heat source, in terms of maximizing the temperature difference and, therefore, the energy savings. For smaller numbers of diffusers, indicated by the shaded region in figure 3.10, the stratification can be used to make an estimate of the thermal comfort of the space.

The implementation of this model into energy simulation codes requires algorithms for the temperatures and the interface height, in terms of the input parameters such as the supply temperature, the heat load and ventilation rate. The model described in this paper calculated the diffuser flow by solving the negatively buoyant jet equations numerically. However, it is possible to treat the diffuser flow simply as a jet using similarity theory and this turns out to give a reasonably

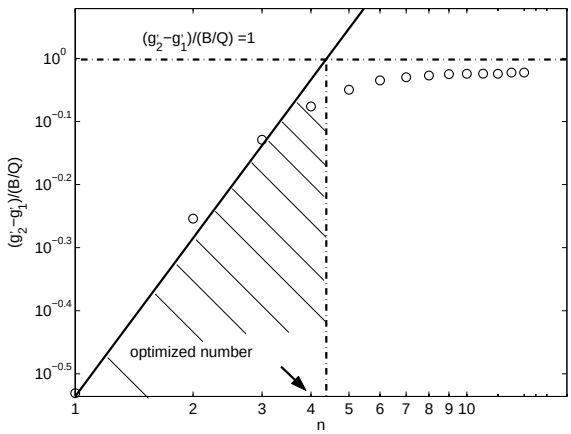

Figure 3.10: A regime diagram showing the region (shaded) where the diffusers work efficiently with a given heat load and ventilation flow rate.

accurate estimate of the volume flux and, therefore, of the penetrative entrainment rate E. From a practical viewpoint different diffuser geometries, such as those that induce significant swirl in the flow, can be treated by adjusting the diffuser entrainment constant α_f.

This approach of using a simplified model, based on the building blocks of layered stratification and plumes and jets using integral plume equations, provides a rational basis for predicting the performance of UFAD systems. Supported by comparisons with experiments, and comparisons with full-scale data (not reported here), these models allow the performance to be optimized in terms of both energy savings and thermal comfort. This approach also allows other effects, for example the treatment of sources sufficiently close together that their plumes coalesce (Kaye & Linden 2004), to be included in a consistent manner. Other effects, such as using radiant cooling of floors or ceilings can also be included by adding the appropriate heat transfers into the layers. As in the case of natural ventilation these models provide design guidance and a basis for calculating the energy performance of low energy ventilation systems in buildings, based on a rational representation of the physics of the ventilation fluid dynamics.

Chapter 4

The Interior Zone Model — Single Diffuser & Multiple Sources

In Chapter 3, we studied the effects of multiple diffusers and a single plume in a UFAD system. We proposed to divide the room into zones with one single plume in each so that the multi-diffuser model is applicable when there are multiple plumes of equal strength in the room. However, in the situations where the number of plumes exceeds the number of diffusers, it is more reasonable to divide the room into regions around each single diffuser. Further, in practice, heating occurs because of distributed sources of buoyancy of different strengths located at various positions within a space. This is one of the reasons why a more gradual change of thermal stratification is observed in practical situations. The effects of vertical position of a buoyancy source has been studied in Chapter 3. Discussions of interacting jets and plumes, of relevance when a diffuser is located close to a heat source or when heat sources are close together, can be found in Hunt, Linden & Cooper (2001) and Kaye & Linden (2004). For the sake of simplicity, here all sources are assumed to produce plumes that rise without interaction throughout the enclosure. Cooper & Linden (1996) described experiments and theoretical

modelling of two point sources of buoyancy in a natural ventilation system to determine the flow driven by two unequal sources of buoyancy. Then they extended the analysis to multiple sources and presented an approximate model of the flow and stratification in Linden & Cooper (1996).

In an attempt to address the two issues above, we first consider a UFAD enclosure of multiple sources of equal strength and then extend the model to cover multiple sources of buoyancy of different strengths. The fluid mechanics are complicated by the fact that the stronger plumes rise through a stratified region and spread at higher levels due to their buoyancy, and the fact that a strong diffuser penetrates all interfaces and brings the warm fluid from the top of the space back to the lower layers, while a weak diffuser only passes through some interfaces and entrains the fluids from middle layers. We will study both cases of a strong and a weak diffuser for two unequal buoyancy sources. For the case of multiple sources of different strengths, we restrict our analysis to that of a strong diffuser.

4.1 Theoretical model for multiple heat sources of same strength

The ability to divide the room into zones with one source in each zone is only possible if all the sources are of equal strength. Therefore, we first consider multiple equal sources in a UFAD system. Figure 4.1 shows a schematic diagram of multiple point sources of equal buoyancy fluxes in a UFAD system with a single cooling diffuser. All plumes are separated horizontally sufficiently far apart to ensure they develop independently. Sources 1, 2..., m are assumed to be "ideal point sources" in that they each release a finite buoyancy flux but zero mass and momentum. Non-ideal sources an be corrected using virtual origins as in Chapter 3.

Using similar reasoning to the two cases studied in Chapter 3 on distributing the ventilation air between multiple diffusers, here we discuss the effects

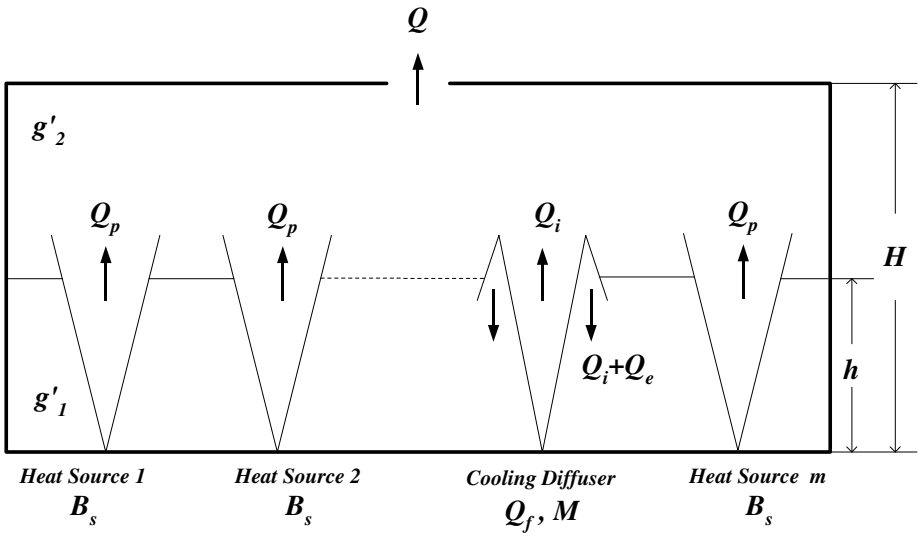

Figure 4.1: A UFAD model with multiple equal heat sources and single cooling diffuser.

of distributing the total heat load among multiple plumes. First, we investigate the case with the total heat load fixed and then we consider the case of different numbers of heat sources with the strength of each heat source unchanged. In both cases, each plume has the same buoyancy flux B_s, and carries equal amounts of volume flux Q_p at an interface height h. The single diffuser flow penetrates the interface with a volume flux Q_i, and entrains an amount of upper layer fluid of Q_e back to the lower zone. As in Chapter 3, we assume $Q_e = EQ_i$ where E is the penetrative entrainment rate determined by (2.11). At the ceiling, $Q = Q_f$ is extracted out of the enclosure.

We divide the number of diffusers $n = 1$ up into a number of separate heat sources m as n', thus $n' = 1/m$. Therefore, the two cases described above, respectively, are the extension ($0 \leq n' \leq 1$) for multiple diffusers with fixed ventilation rate and fixed underfloor pressure described in § 3.1.2, where $n' \geq 1$.

4.1.1 Fixed heat load and total ventilation rate

When the total heat load B and total ventilation rate Q are fixed, the total heat load B is equally distributed into m heat sources, so that $B_s = B/m$ (figure 4.1). Conservation of volume flux in steady state is

$$mQ_p = Q + Q_e, \tag{4.1}$$

and conservation of buoyancy flux gives that the upper layer reduced gravity

$$g_2' = \frac{B}{Q}. \tag{4.2}$$

By balancing the buoyancy into and out of the lower layer as shown by (3.3), we find that the reduced gravity of the lower layer is given by

$$g_1' = \frac{g_2' Q_e + g_f' Q + g_1' (Q_i - Q)}{Q_e + Q + (Q_i - Q)}, \tag{4.3}$$

where g_f' is the buoyancy of the diffuser flow. Again, the reference density is chosen so that $g_f' = 0$, and all temperatures are referenced to the supply temperature. Thus,

$$g_1' = \frac{g_2' Q_e}{Q_e + Q} = \frac{g_2' Q_e}{mQ_p}. \tag{4.4}$$

In a large stationary uniform ambient fluid, the volume flux in a buoyant plume at the interface, according to (3.10), is

$$Q_p = C\,(\frac{1}{m} B\, h^5)^{1/3}, \tag{4.5}$$

where $C = \frac{6}{5}\alpha(\frac{9}{10}\alpha)^{\frac{1}{3}}\pi^{\frac{2}{3}}$. The entrainment rate α of the plume was chosen to be 0.117 as in Chapter 3.

Theoretical predictions of the buoyancy profiles using dimensionless height (3.11) and dimensionless buoyancy (3.12), where $C = 0.142$ is the universal plume constant and B is the total buoyancy fluxes are shown in figure 4.2(a). The figure shows that for the same total heat load and ventilation flow rate, the upper layer

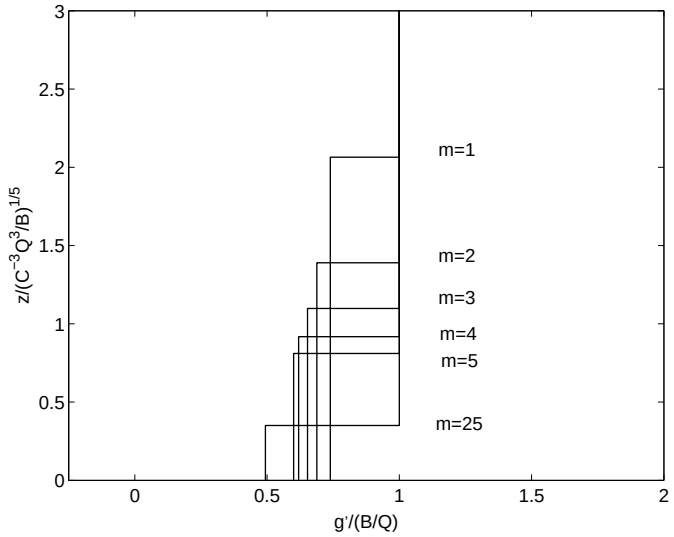

(a)

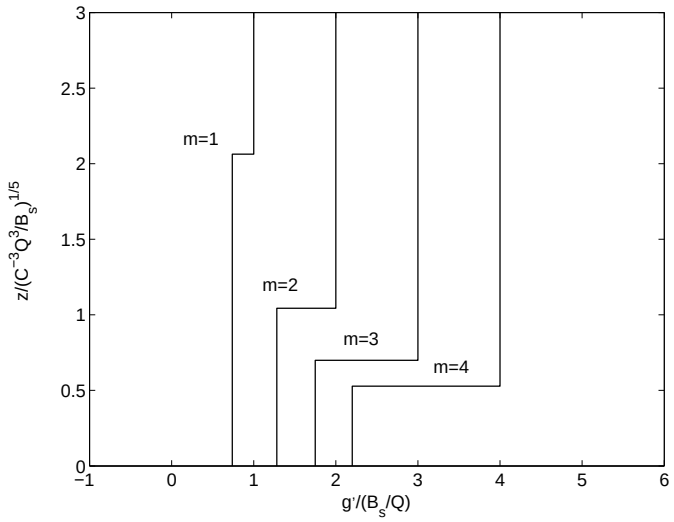

(b)

Figure 4.2: Theoretical model predictions for m equal plumes and a single diffuser (a) in the conditions of constant total heat load, $m = 1, ..., 5$, and $m = 25$; (b) in the conditions of constant heat load per plume, $m = 1, ..., 4$. The dimensionless parameters $\hat{z}$ and $\hat{g'}$ are obtained in terms of the total buoyancy flux B in (a), and buoyancy flux per plume B_s in (b). Q is the total ventilation rate in both cases. The buoyancy profiles for $m = 1$ in both cases are the same (note the different scales on the abscissa), since $B = B_s$ when $m = 1$.

buoyancy remains the same, which is consistent with (4.2) and the multiple diffusers case in § 3.1.1. Further, as the number of heat sources increases, the interface height decreases and the lower layer buoyancy reduces. From volume conservation (4.1), we get $Q_p = 1/m(Q + Q_e)$. Thus, when m increases, Q_p decreases and the interface drops correspondingly. The equation $mQ_p = C\,(m^2 B\, h^5)^{1/3}$ means that $mQ_p \sim m^{2/3}h^{5/3}$. So, mQ_p decreases with m if h decreases faster than $m^{-2/5}$, which will be shown in §4.4. From (4.4) the lower layer reduced gravity is

$$g_1' = \frac{B}{Q}\frac{Q_e}{mQ_p} = \frac{B}{Q}(1 - \frac{Q}{mQ_p}).$$

Therefore, g_1' decreases due to a smaller mQ_p. At the limit $m \to \infty$, g_1' approaches g_2', and the interface drops to the floor level, i.e., the whole enclosure has a uniform temperature determined by (4.2), so there is no stratification in the space. It is equivalent to having a uniformly heated floor in the room. This problem in a natural ventilation system has been studied by Gladstone & Woods (2001).

4.1.2 Fixed heat load per heat source and total ventilation rate

In this section, we consider the case where the total heat load B changes with the number of heat sources, $B = mB_s$. Since the total ventilation rate Q is fixed, this is equivalent to decreasing the ventilation rate per heat source. The upper layer reduced gravity is then

$$g_2' = \frac{mB_s}{Q}, \tag{4.6}$$

which grows at the same magnitude as the total heat load. The increased heat load does not affect the volume flux conservation, so (4.1) remains valid. And, the lower lower layer temperature g_1' is calculated by the same equation as (4.4).

Figure 4.2(b) shows the theoretical buoyancy profiles by considering additional equal plumes added into the UFAD system. Or, because the buoyancy flux in each plume and the volume flux in the diffuser remains unchanged, which is the case with constant underfloor pressure as discussed in § 3.1.2, we can also

consider the addition of more equal plumes as equivalent to having fewer diffusers in constant underfloor pressure systems. In this case, the dimensionless buoyancy (3.12) uses the single plume buoyancy flux B_s since B_s is now fixed. In the figure, the dimensionless upper layer reduced gravity $\hat{g_2'}$ has the same value as the number of plumes m, which can be seen from (4.6) and (3.12). With the same conservation equation (4.1) and the same reasoning in §4.1.1, the interface decreases when m increases. Since the heat load for each source stays the same, the total heat load B in the room and the upper layer reduced gravity g_2' increases with the number of sources m. The lower layer reduced gravity g_1' also increases because the fountain entrains warmer upper layer fluid back to the lower layer. Therefore, given the same ventilation rate Q and the same supply air temperature, the ability of the fountain flow to cool the room decreases. With $m \to \infty$, we expect that the enclosure will be filled up with the upper warm air determined by (4.6) and the two-layer stratification will vanish with the interface approaching to the floor.

4.2 Theoretical model for multiple heat sources of different strengths

In reality, heat sources in a room are not likely to have the same strength. In this section, we study the effects of multiple unequal-strength plumes in a UFAD system. For the sake of simplicity, we first consider two plumes with unequal buoyancy fluxes (B_1 and B_2, with $B_1 = \psi B_2$, where $B_2 = B$ and $0 \leq \psi \leq 1$). Since the stronger plume reaches the ceiling, while the weaker plume may not have sufficient buoyancy to penetrate through the upper buoyant layer, it is likely that a three-layer stratification will form. An analogous form of stratification was found in a naturally ventilated enclosure (Cooper & Linden 1996). It is assumed that all the fluid of the stronger plume passes through the upper interface, and the weaker plume and the fountain reach some level below the upper interface. Further, we take the approximation that the buoyancy flux in the strong plume B_2

remains unchanged as it rises through the middle layer. Although the buoyancy flux changes in reality, since the volume flux in the plume $Q \sim B^{1/3}$, taking the buoyancy flux in the plume as constant is a good approximation. Linden & Cooper (1996) have shown that this approximation, which depends on the volume flux of a plume being relatively insensitive to the buoyancy flux and relatively sensitive to the height, provides an accurate description of the behavior of the lower interface and reasonably good descriptions of the upper interface, and the relative buoyancies of the upper two layers is the same as the exact result.

In the case of a three-layer stratification there are two possibilities to consider. If the diffuser flow is weak then it may only have sufficient upward momentum to penetrate into the second layer (figure 4.3). On the other hand, if the diffuser flow is strong it may have sufficient upward momentum to pass through the middle layer into the upper layer (figure 4.5). This, obviously, depends on the stratification.

In the former case, the entrainment flux from the diffuser returns to the lower layer as in the two-layer cases discussed in Chapter 3. However, in the case where the diffuser penetrates into the top layer, the hot air entrained by the diffuser may either be brought down into the lower layer or discharged into the middle layer. The analysis of these situations are considered in detail in the next sections.

4.2.1 Weak diffuser

We first consider the case of a weak diffuser in which the diffuser flow only reaches the middle layer then falls back to the lower layer. Volume conservation implies

$$Q_f = Q_{22} = Q, \tag{4.7}$$

and

$$Q_{22} = Q_{21} + Q_{11} - Q_e, \tag{4.8}$$

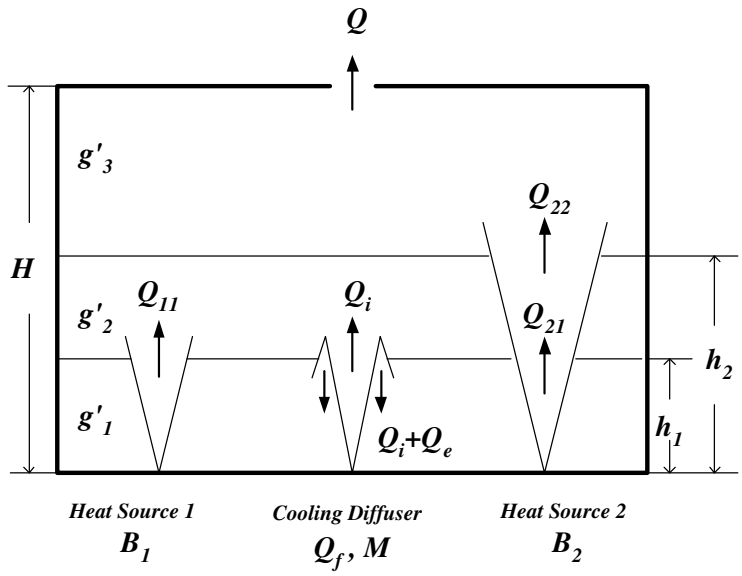

Figure 4.3: A three-layer model of a UFAD system with two plumes and one cooling diffuser which only penetrates the lower interface.

where, as shown in figure 4.3, the volume fluxes in plumes 1 and 2 passing through the lower interface are

$$Q_{11} \;=\; C\,(\,\psi B\,h_1^5)^{1/3}, \tag{4.9}$$

and

$$Q_{21} \;=\; C\,(\,B\,h_1^5)^{1/3}, \tag{4.10}$$

respectively. These equations do not rely on the approximation referred to above and are exact. In order to estimate the volume flux in plume 2 passing through the upper interface, we take

$$Q_{22} \;=\; C\,(\,B\,h_2^5)^{1/3}, \tag{4.11}$$

where, as discussed above, we assume that B is constant with height.

In steady state buoyancy conservation applies. For the entire space,

$$(\psi + 1)B \;=\; g_3^{'} Q, \tag{4.12}$$

which gives the steady-state reduced gravity of the upper layer

$$g_3^{'} \;=\; \frac{(\psi + 1)B}{Q_{22}}. \tag{4.13}$$

For the middle layer,

$$\psi B + Q_{11} g_1^{'} - Q_e g_2^{'} - (Q_{22} - Q_{21}) g_2^{'} = 0, \tag{4.14}$$

Substituting (4.8) into (4.14) gives

$$g_2^{'} = \frac{\psi B}{Q_{11}} + g_1^{'}. \tag{4.15}$$

For the lower layer

$$-Q_{11} g_1^{'} + Q_e g_2^{'} - Q_{21} g_1^{'} = 0, \tag{4.16}$$

i.e.

$$g_1^{'} = \frac{Q_e g_2^{'}}{Q_{11} + Q_{21}}. \tag{4.17}$$

Substitute (4.17) and (4.8) into (4.15) to get

$$g_2^{'} = \frac{\psi B (Q_{11} + Q_{21})}{Q_{11} Q_{22}}. \tag{4.18}$$

Therefore, using (4.9), (4.10), (4.11), (4.13) and (4.18), the buoyancy of middle layers relative to the upper layer is

$$\frac{g_2^{'}}{g_3^{'}} \;=\; \frac{\psi}{\psi + 1} + \frac{\psi^{2/3}}{\psi + 1}. \tag{4.19}$$

Equation (4.19), plotted in figure 4.4(a), shows that the buoyancy of the top two layers is independent of the penetrative entrainment Q_e. This is consistent with the fact that the circulation of the weak diffuser flow only affects the lower layer. When $\psi = 0$, the results reduce to the case with one single heat source and one single cooling vent developed by Lin & Linden (2005). In this case, (4.19) gives $\frac{g_2^{'}}{g_3^{'}} = 0$ as expected, which means there is no middle layer consistent with a

two-layer stratification. When $\psi = 1$, it represents a UFAD system with two equal heat sources and one single cooling diffuser discussed in § 4.1.2. From (4.19), we get $g_2^{'} = g_3^{'}$. Therefore, the middle layer and the upper layer merge into one layer to form a two-layer stratification as observed in experiments, which means that $Q_{11} = Q_{21}$ and Q_{22} vanishes. Then, (4.8), (4.13) and (4.17) reduce to $2Q_p = Q+Q_e$, $g_3' = 2B/Q$ and $g_1' = g_3' Q_e/(2Q_p)$, respectively, which are the same as (4.1), (4.6) and (4.4) with $m = 2$. Figure 4.4(a) shows that increasing ψ, thereby making the plumes more equal in strength, diminishes the density difference between the middle layer and the upper layer.

We now consider the interface positions. Since $Q_f = Q_{22} = C\,(\,B\,h_2^5)^{1/3}$, the upper interface position is determined by

$$h_2 \;=\; \frac{Q_f^{3/5}}{C^{3/5}B^{1/5}}, \tag{4.20}$$

which shows that the upper interface only depends on the ventilation flow rate and the buoyancy of the stronger plume, and does not depend on any geometry parameter, such as the room height or the opening area of the diffuser. It is because the diffuser does not affect the upper layer and all fluid is recirculated in the lower layers. This is the same result as in a displacement system.

At the lower interface h_1,

$$Q_f + Q_e \;=\; Q_{21} + Q_{11} \;=\; CB^{1/3}(1+\psi^{1/3})h_1^{5/3}. \tag{4.21}$$

So,

$$h_1 \;=\; \frac{(Q_f + Q_e)^{3/5}}{C^{3/5}B^{1/5}(1+\psi^{1/3})^{3/5}}. \tag{4.22}$$

For a fixed ventilation flow rate Q_f and a fixed ratio of buoyancies of two plumes ψ, the lower interface h_1 has the minimum height at the limit $Q_e = 0$ (which corresponds to displacement ventilation) and, since h_2 is independent of Q_e (see (4.20)), this provides an upper bound for the thickness of the middle layer $h_2 - h_1$ in UFAD cases. Other cases are too complicated to get closed expressions. Now we

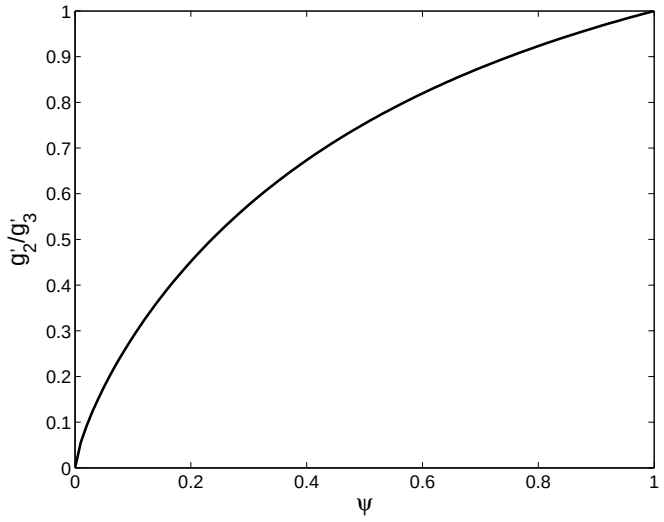

(a)

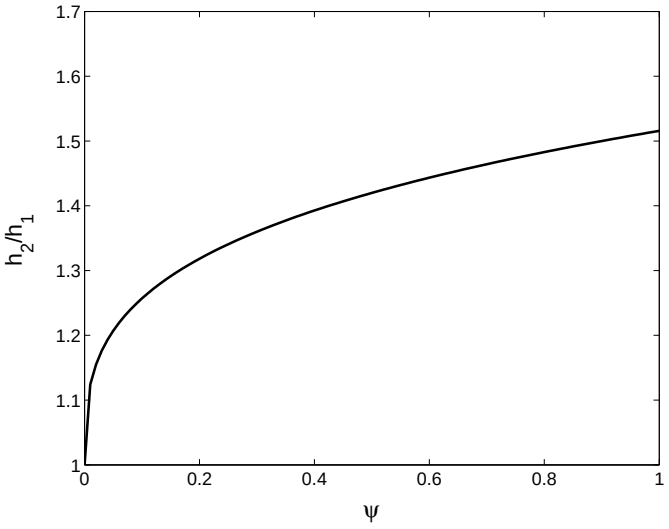

(b)

Figure 4.4: With two unequal plumes and a single weak diffuser, (a) density contrast between the middle and upper layers $\frac{g_2^{'}}{g_3^{'}}$ with ψ in a UFAD enclosure; (b) the thickness of the middle layer $\frac{h_2}{h_1}$ change with ψ in a displacement ventilation system.

study, in displacement ventilation cases ($Q_e = 0$), how the middle layer thickness changes with ψ. For these cases, (4.22) reduces to

$$h_1 = \frac{Q_f^{3/5}}{C^{3/5}B^{1/5}(1+\psi^{1/3})^{3/5}}, \tag{4.23}$$

and since the upper interface is calculated by (4.20), the ratio of the layer thickness is given as

$$\frac{h_2}{h_1} = (1+\psi^{1/3})^{3/5}, \tag{4.24}$$

which has been plotted in figure 4.4(b). Therefore, (4.24) implies $1 \leq \frac{h_2}{h_1} \leq 1.52$ with $0 \leq \psi \leq 1$ in displacement ventilation. Figure 4.4(b) shows in displacement ventilation the thickness of the middle layer increases with bigger ψ. So, in a UFAD system with the same Q_f and ψ, $\frac{h_2}{h_1}$ is even smaller than that in displacement ventilation due to the effect of the penetrative entrainment by the diffuser flow Q_e. Therefore, we expect that the thickness of the middle layer decreases when ψ decreases, as shown in figure 4.4(b).

In conclusion, in a UFAD system with two unequal plumes and a weak diffuser, the weaker plume, with the smaller buoyancy flux, terminates in the middle layer, and the stronger plume with the larger buoyancy flux rises higher up before discharging its buoyant fluid into the space. The weak diffuser has sufficiently low momentum so that it only passes through the lower interface and entrains the fluid in the middle layer back to the bottom layer. This penetrative entrainment increases the lower interface but does not affect the upper interface. Therefore, the displacement ventilation where the penetrative entrainment is turned off, has the upper limit of the thickness of the middle layer for UFAD systems. Although large ψ increases the thickness of the middle layer, the densities in middle and upper layer approach each other as $\psi \to 1$. Therefore, we either have a thin middle layer ($h_2/h_1 \sim 1$) or close densities of the upper two layers ($g_2^{'}/g_3^{'} \sim 1$).

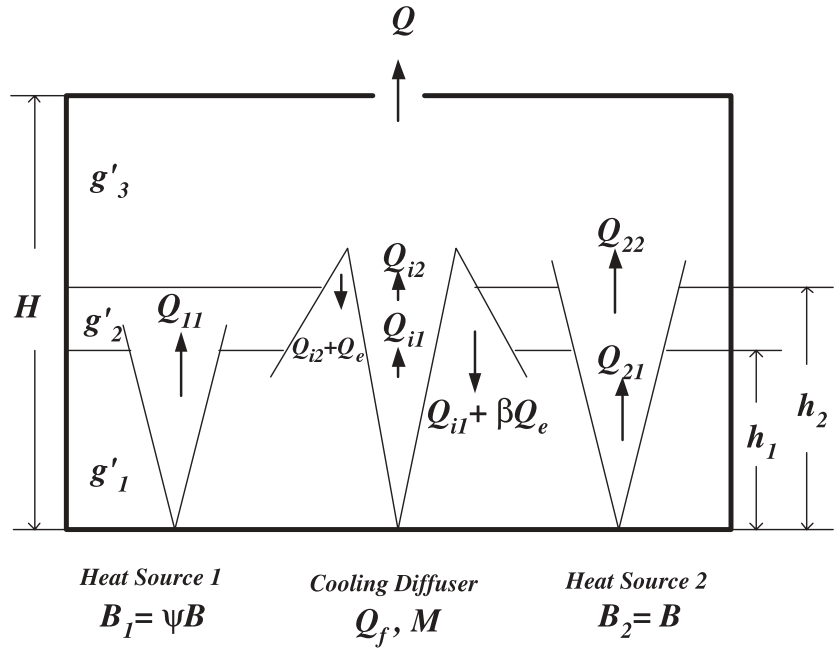

Figure 4.5: A three-layer model of a UFAD system with two plumes and one cooling diffuser which penetrates both interfaces.

4.2.2 Strong diffuser

In this section, we consider a fountain with sufficient momentum flux so that it penetrates both interfaces and reaches the upper layer (figure 4.5). Further, we take the approximation that the stratification is neglected both in the strong plume (as before) and the strong diffuser as they rise through the middle layer. Finally, since it is difficult to determine the amount of diffuser flow that stays in the middle layer when the fountain reverses, we assume that the diffuser flow has a total of $Q_{i1} + \beta Q_e$ $(0 \leq \beta \leq 1)$ entering the lower layer, in which Q_e is the entrainment of upper layer fluid by the fountain and Q_{i1} is the volume flux at the lower interface in the diffuser flow when it rises.

Steady state conservations of volume flux for the whole enclosure, the top layer and the middle layer are

$$Q_f = Q, \tag{4.25}$$

$$Q_{22} - Q_e = Q, \tag{4.26}$$

and

$$Q_{22} = Q_{21} + Q_{11} + (1-\beta)Q_e. \tag{4.27}$$

Conservation of buoyancy in the entire chamber gives

$$g_3^{'} = \frac{(\psi+1)B}{Q}. \tag{4.28}$$

For the lower layer,

$$-Q_{11}g_1^{'} + \beta Q_e g_3^{'} - Q_{21}g_1^{'} = 0, \tag{4.29}$$

so

$$g_1^{'} = \frac{\beta Q_e}{Q_{11}+Q_{21}}\, g_3^{'}. \tag{4.30}$$

For the middle layer,

$$\psi B + Q_{11}g_1^{'} + (1-\beta)Q_e g_3^{'} - (Q_{22}-Q_{21})g_2^{'} = 0. \tag{4.31}$$

Therefore,

$$g_2^{'} = \frac{\psi B + Q_{11}g_1^{'} + (1-\beta)Q_e g_3^{'}}{Q_{22}-Q_{21}}. \tag{4.32}$$

In order to investigate trends we first plot the effect of different values of β for the case where $B_1 = 1/2B_2$ ($\psi = 0.5$). Figure 4.6 shows that the middle layer thickness and the density difference between the upper two layers decrease as β increases. When $\beta = 1$ the ratio of the layer thicknesses h_2/h_1 has the minimum value and the buoyancy difference between upper two layers is smallest. The case $\beta = 0$ (not shown in the figure) implies that all the entrainment by the fountain stays in the middle layer. In that case, from (4.30), $g_1^{'} = 0$, which means that the lower layer has the same temperature as the supply air as in displacement ventilation case, because no entrainment of warm air gets into the lowest layer.

The middle layer buoyancy can be obtained by (4.32) for the case of two unequal plumes. With more plumes of different strengths, the calculation for the buoyancies of the middle layers is complicated because buoyancy conservation for

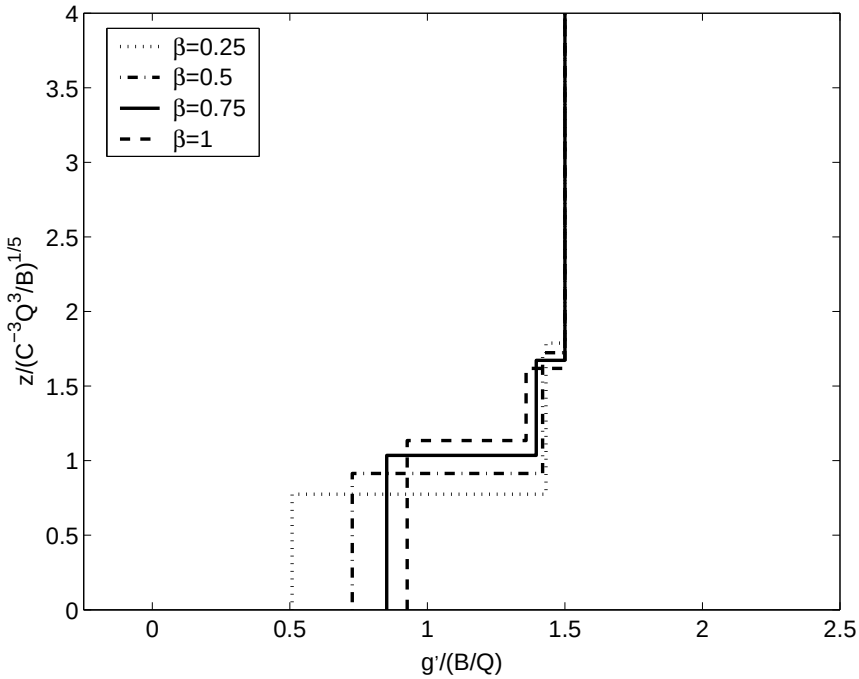

Figure 4.6: Strong diffuser model predictions for 2 unequal plumes ($\psi = 0.5$) and a single diffuser in a UFAD system. Both the middle-layer thickness and the density difference between the upper two layer decrease with β.

each layer is needed. However, in the case $\beta = 1$, where the entrainment all goes into the lower layer, the middle layers play only a small role on the stratification. This fact provides the possibility to use an quasi-two-layer model (ignore buoyancy calculation for the middle layers) to predict the stratification which will be discussed in the next section. Now we consider $\beta = 1$ for the case of two unequal plumes. Volume flux conservation equation (4.27) reduces to

$$Q_{22} = Q_{21} + Q_{11}. \tag{4.33}$$

Consequently, the ratio of layer thicknesses is

$$\frac{h_2}{h_1} = (1 + \psi^{1/3})^{3/5}, \tag{4.34}$$

which is the same as (4.24). Therefore, with $\beta = 1$, the ratio of the layer thicknesses h_2/h_1 has the upper bound $1 \leq \frac{h_2}{h_1} \leq 1.52$ over the range of flux ratio $0 \leq \psi \leq 1$ as shown in figure 4.4(b). Further, with $\beta = 1$, the reduced gravities of the middle layer and the lower layer are

$$g_2^{'} = \frac{\psi B}{Q_{11}} + g_1^{'}, \tag{4.35}$$

and

$$g_1^{'} = \frac{Q_{22} - Q_f}{Q_{22}} g_3^{'}, \tag{4.36}$$

and the buoyancy of middle layer relative to the upper layer is

$$\begin{aligned} \frac{g_2^{'}}{g_3^{'}} &= 1 + \frac{\psi}{\psi + 1}\frac{Q_f}{Q_{11}} - \frac{Q_f}{Q_{11} + Q_{21}}, \\ &= 1 + \frac{(\psi Q_{21} - Q_{11})Q_f}{(\psi + 1)(Q_{11} + Q_{21})Q_{11}}, \\ &= 1 + \frac{Q_f}{Q_{21}}\frac{\psi^{2/3} - 1}{(\psi + 1)(1 + \psi^{1/3})}. \end{aligned} \tag{4.37}$$

We first consider the limiting case of a single plume, $\psi = 0$. In this case (4.34) implies that $h_2 = h_1$. All the ventilation flow Q_f is carried by the plume

at the interface height h_1, i.e., $Q_f = Q_{21}$. Thus, $g_2^{'}/g_3^{'} = 0$, by (4.38), which suggests that the middle layer has vanished. Therefore, the two-layer case for a single-plume single-diffuser system (Lin 2003) is recovered, as expected. For the case of two equal plumes $\psi = 1$, (4.38) gives that $g_2^{'}/g_3^{'} = 1$. Consequently, the stratification turns to a simple two-layer form for a two-equal-plume single-diffuser system because the buoyancy of the upper two layers are the same. Therefore, similar to the weak diffuser model, either the middle layer is thin or the density differences between the upper two layers are small.

4.2.3 Approximate multi-unequal-plume model with a strong diffuser flow

Now we extend this approach to the case of m unequal plumes of buoyancy fluxes $B_1 < B_2 < ... < B_m = B$, and denote the relative strengths by $\psi_j = B_j/B_m,\ j = 1, ..., m-1$. It is assumed that all the plumes are on the floor and the flow develops into a series of $m+1$ layers separated by interfaces at $z = h_j$ (figure 4.7). For the sake of simplicity, we only consider the strong diffuser case, in which the diffuser flow penetrates all interfaces. This is the only situation in which the upper layer temperature is affected. Other cases are very complicated, and beyond the range of this study. Further, as before the stratification is neglected to calculate the volume fluxes in the stronger plumes and the diffuser, and the entrainment by the fountain in the middle layers when it falls is ignored. Finally, we assume that the diffuser flow has a total of $Q_{i1} + \beta Q_e$ entering the lower layer, where ($\beta = 1$), Q_e is the entrainment of upper layer fluid by the fountain and Q_{i1} is the volume flux at the lowest interface in the diffuser flow when it rises.

Mass conservation gives that

$$Q_f = Q, \tag{4.38}$$

$$Q_{mm} - Q_e = Q, \tag{4.39}$$

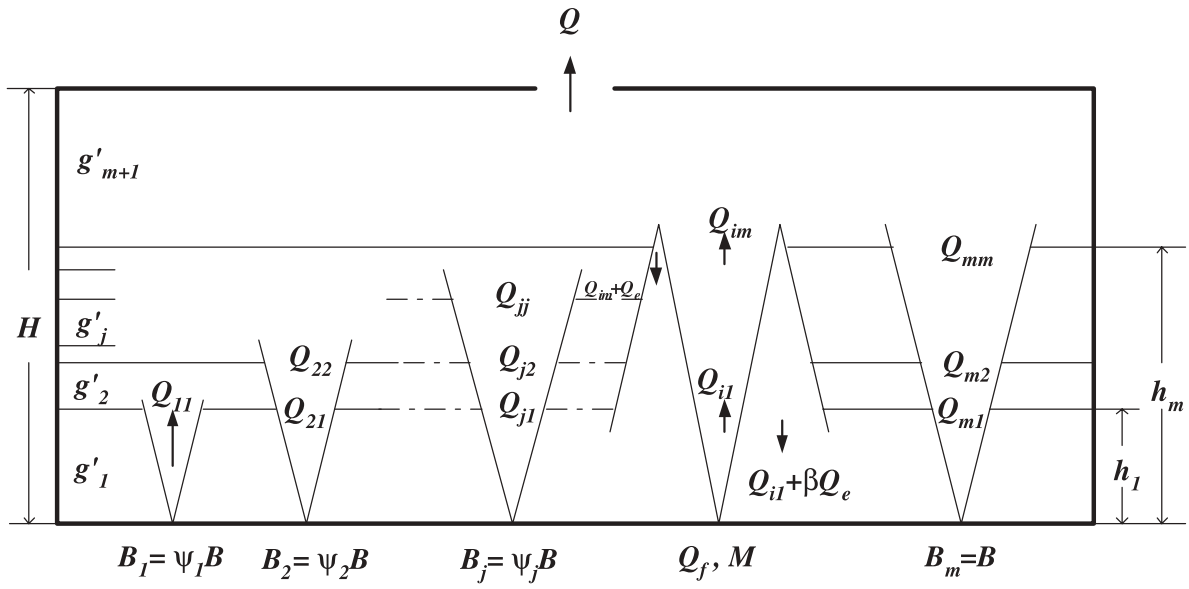

Figure 4.7: A multi-layer model of a UFAD system with m plumes of unequal strengths and one strong cooling diffuser which penetrates all interfaces.

and

$$\begin{aligned} Q_{mm} &= Q_{11} + Q_{21} + ... + Q_{j1} + ... + Q_{m1} \\ &= \sum_{j=1}^{m} Q_{j1}. \end{aligned} \tag{4.40}$$

Note (4.41) is a generalization of (4.27). Similarly to § 4.2.2, the penetrative entrainment Q_e is given by

$$Q_e \;=\; E \cdot Q_{im}, \tag{4.41}$$

where, the penetrative entrainment rate E is determined by (2.11), and the volume flux of the diffuser Q_{im} at the highest interface is calculated by the fountain model described in § 2.4.1.

From (4.41)

$$\begin{aligned} C\,(\,B\,h_m^5)^{1/3} &= C\,(\,\psi_1 B\,h_1^5)^{1/3} \;+\; C\,(\,\psi_2 B\,h_1^5)^{1/3} + ... + \; C\,(\,B\,h_1^5)^{1/3} \\ &= C\,(\sum_{j=1}^{m-1} \psi_j B\,h_1^5)^{1/3} + \; C\,(\,B\,h_1^5)^{1/3}. \end{aligned} \tag{4.42}$$

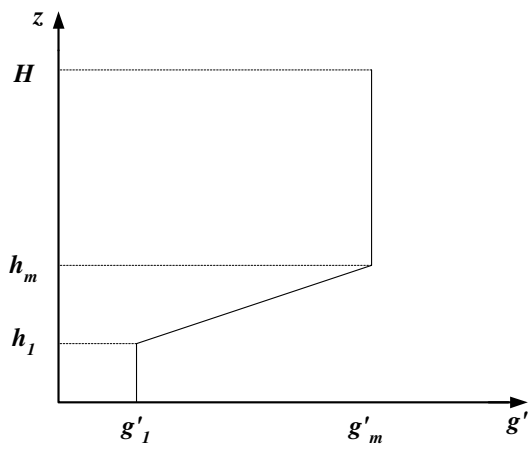

Figure 4.8: An approximate two-layer stratification for a UFAD system with multiple plumes of unequal strength and one strong cooling diffuser.

Consequently,

$$\frac{h_m}{h_1} = (1 + \sum_{j=1}^{m-1} \psi_j^{1/3})^{3/5}, \tag{4.43}$$

where, the highest interface h_m is determined by the conservation equation (4.39). Buoyancy flux conservation gives the buoyancy of the top layer as

$$g'_{m+1} = \frac{(1 + \sum_{j=1}^{m-1} \psi_j)B}{Q}. \tag{4.44}$$

and the buoyancy of the bottom layer as

$$g'_1 = \frac{Q_{mm} - Q_f}{Q_{mm}} g'_{m+1}. \tag{4.45}$$

A general quasi-two-layer stratification for m plumes of unequal strengths is obtained as shown in figure 4.8, based on the assumptions that the interior stratification is ignored when the dynamics of the plumes and the diffuser are calculated and that the fluid entrained by the fountain falls from the top layer to the bottom layer. Without these assumptions, the calculation of the plumes and the fountain as they pass through successive interfaces are extremely complicated. Further the

amount penetrative entrainment fluid that goes to each layer is very difficult to determine. This quasi-two-layer model only requires the lowest and highest interface positions and the buoyancies of the bottom and top layers. Compared with the two-layer model for single-plume single-diffuser case, the lowest interface h_1 is the only additional parameter, which can be calculated by (4.43). From the viewpoint of design, the position of the lowest interface h_1 is the critical parameter that designers care most about. Therefore, this quasi-two-layer approximation model includes the most critical characters of the stratification without introducing complicated calculations. From (4.43), h_1 increases with larger h_2. The amount of the change for h_1 depends on the number of the sources m, and the strengths ratio of each source ψ_j.

4.3 Experimental results

Experiments are limited, for practical reasons, for two plumes only. These experiments were conducted in tank #B (58.5 cm long, 28 cm wide and 58.5 cm deep). In the qualitative experiments, shadowgraphs were used to visualize the flow and interfaces. The experimental setup is similar to that described in Chapter 2 except that the salt-solution coming from the constant head, gravity-fed system was now distributed into two plume nozzles. Each plume nozzle was connected with a calibrated flow meter (GF-1360) which controls the flow rate. Experiments with unequal strength plumes were carried out to compare with the theory presented in §4.2. Since the reduced gravity of the salt-solution for both plumes are the same and $B = g_s^{'} Q_s$, the ratio of buoyancy fluxes of the two plumes is determined by the ratio of the flow rates. Flux ratios in the range $0.2 \leq \psi < 1$ were considered (see table 4.1).

We have also carried out experiments with two unequal plumes in displacement enclosure by setting up a flat metal plate about 2.5 cm underneath the fountain nozzle in the same tanks, in order to observe the maximum middle layer

Exp. No.	B (cm^4s^{-3})	M (cm^4s^{-2})	Q_f (cm^3s^{-1})	ψ	No. of Plumes	Q_e	Tank Label
1	69.3	182	15.2	0	1	$\neq 0$	A
2	67.2	177	15.0	1.00	2	$\neq 0$	B
3	36.5	177	15.0	1.00	2	$\neq 0$	B
4	68.2	177	15.0	0.50	2	$\neq 0$	B
5	69.3	32.7	6.44	0.50	2	$\neq 0$	B
6	69.3	32.7	6.44	0.25	2	$\neq 0$	B
7	70.1	50.4	9.00	0.50	2	$\neq 0$	B
8	71.0	50.4	9.00	0.13	2	$\neq 0$	B
9	65.6	78.7	10.0	0	1	$\neq 0$	B
10	327	78.7	10.0	0.20	2	$\neq 0$	B
11	64.0	544	26.3	0.26	2	$=0$	B

Table 4.1: 11 different experimental conditions for multiple plume studies. B is the buoyancy flux of each source (equal plumes cases) or is the buoyancy flux of the stronger heat source (unequal plumes cases); M and Q_f are the momentum fluxes and volume fluxes of the cooling diffuser. ψ is the buoyancy fluxes ratio between the weaker plume and the stronger plume. Q_e is the penetrative entrainment at the interface by the fountain flow.

for certain ψ as described in § 4.2.1. The plate prevents the fountain flow growing vertically to the interface, thus turning off the penetrative entrainment Q_e and providing a model of displacement ventilation.

In table 4.1, B is the buoyancy flux of each heat source (equal plumes cases) or is the buoyancy flux of the stronger heat source (unequal plumes cases). Exp.$1-3$ are the experiments that examine the effect of two equal plumes, while Exp. $4-11$ consider two unequal plumes. Exp. 11 is the experiment operated in a displacement mode.

Again, all experimental data were measured at steady state. In the following graphs, lines or '$\circ$' indicate the theoretical predictions, '$*$' are the experimental measurements analyzed by *DigImage*(Dalziel 1992-1998, Dalziel 1992-1998), and '$\cdot$' are the measurements of fluid samples by an Anton Paar DMA 5000 density meter, accurate to 10^{-5} g cm^{-3}.

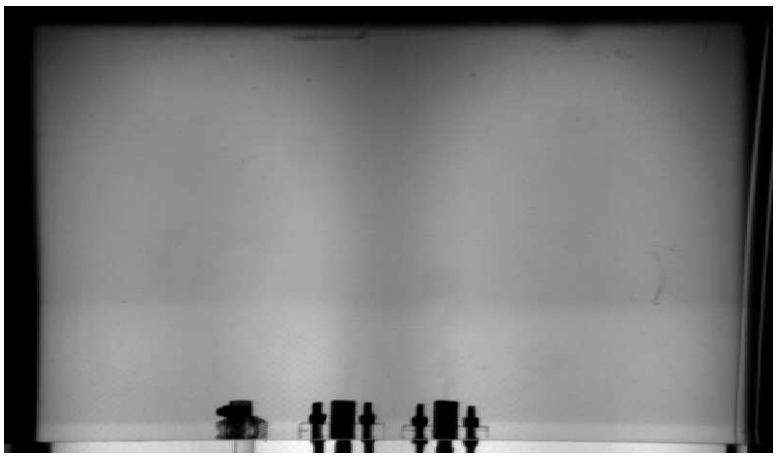

Figure 4.9: A steady-state experimental image of a UFAD system with two equal plumes (the right two) and one single diffuser (the left one).

4.3.1 Two plumes of same strength

Figure 4.10 shows the two cases for equal plumes discussed in § 4.1. Figure 4.10 (a) compares Exp.1 with Exp.3. Exp.3 has two plumes which distribute the buoyancy flux of the single plume in Exp.1 and has almost the same total ventilation rate Q as in Exp.1. The upper layer buoyancy of both experiments are the same as predicted by (4.2). The lower layer buoyancy and the interface height decrease when the total heat load has been distributed into two plumes as expected from (4.1) and (4.4).

Exp.2 has a doubled total buoyancy flux with two equal plumes, with each plume having about the same buoyancy as that of the single plume in Exp.1. The comparisons were shown in figure 4.10(b). The upper layer buoyancy of Exp.2 is twice that Exp.1, which is consistent with (4.6). The lower layer buoyancy also increases while the interface drops with an additional heat source added into the system. The theoretical predictions of the lower layer buoyancy and interface position agree well with the experimental measurements. The offset of the upper layer buoyancy predictions is due to the neglect of the source volume flux of each plume.

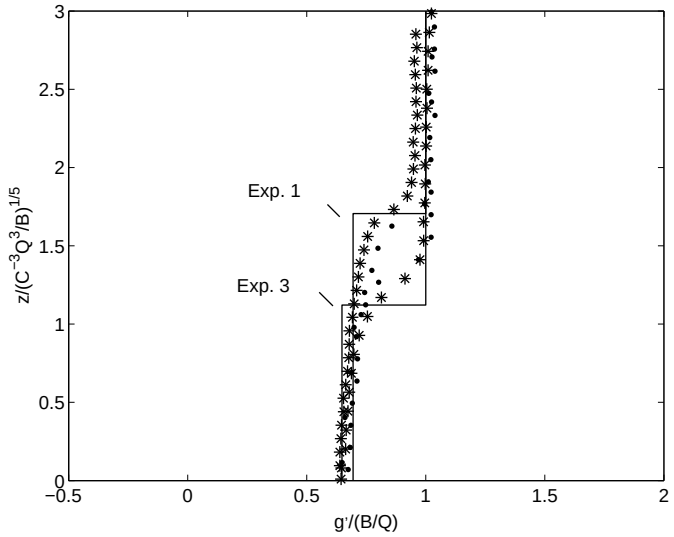

(a)

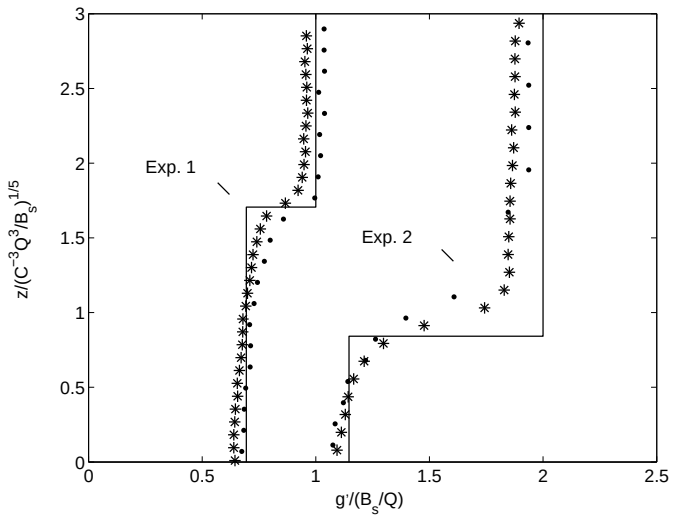

(b)

Figure 4.10: Buoyancy profiles obtained at steady state with two equal plumes. In the height scales and the buoyancy scales, $C = 0.142$, B and Q are the total buoyancy flux and the total ventilation rate, and B_s is the buoyancy flux per plume. (a) Comparisons between Exp.1 with a single plume and Exp.2 with two plumes when the total heat load is fixed; (b) comparisons between Exp.1 with a single plume and Exp.3 with two plumes when the heat load per plume is fixed.

4.3.2 Two plumes of unequal strengths

In order to get qualitative observations of the effects of two plumes with unequal strengths, we started an experiment with a single plume and a single fountain (Exp.9) and, after the system reached the steady state, we turned on another plume with a larger buoyancy flux (Exp.10) to make the ratio of the buoyancy fluxes $\psi = 0.2$. With the single plume and single fountain, a sharp interface formed as shown in figure 4.11(a). After the second plume turned on, we observed that the stronger plume made the sharp interface lower, and the upper layer warmer. However, a second interface was not observed in the experiment (figure 4.11(b)). The ratio of the buoyancy fluxes $\psi = 0.2$ in the experiment tends to give a thin middle layer according to figure 4.4. This could be the main reason why a three-layer stratification is invisible in the experiment. I have also carried out other experiments with larger values of ψ. Unfortunately, the middle layer was not observed in these cases either. Both dye observations, combined with shadowgraph images, consistently showed only a basic two-layer stratification.

To obtain the maximum thickness of the middle layer and to attempt to observe a middle layer, the penetrative entrainment Q_e should be turned off as discussed in § 4.2.1. In our laboratory experiments, we stopped the penetrative entrainment by setting up a metal plate a short distant 2.5 cm from the fountain nozzle as shown in figure 4.12. When the fountain flow hit the metal plate, it spread horizontally across the tank. Therefore, the fountain flow did not reach the interface to entrain the upper layer fluid back to the lower layer, which acts as a displacement ventilation diffuser flow. Hence, the penetrative entrainment $Q_e = 0$.

We carried out one displacement ventilation experiment with $\psi = 0.57$. However, in the experiment the weaker plume was observed to reach the ceiling, which is beyond the restrictions of this Chapter. So, a smaller ratio of the buoyancy fluxes $\psi = 0.26$ was chosen as Exp.11 in table 4.1. The upper interface $h_2 = 10.0$ cm from (4.20). Since $h_2/h_1 = 1.52$, the lower interface $h_1 = 6.6$ cm, and the middle layer thickness is predicted to be $h_2 - h_1 = 3.4$ cm. During the displacement

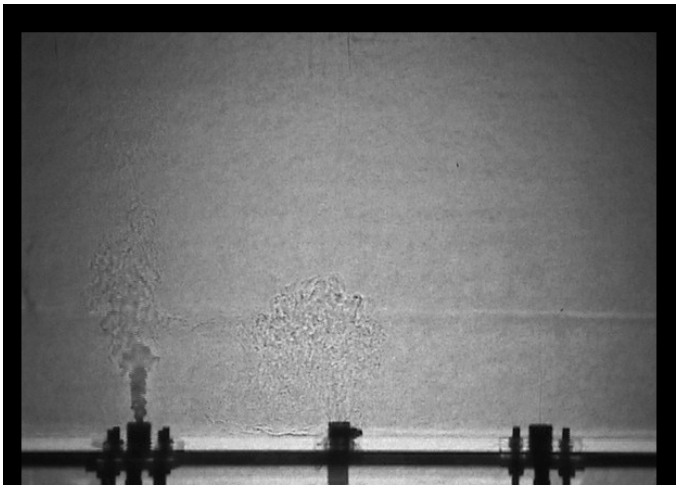

(a)

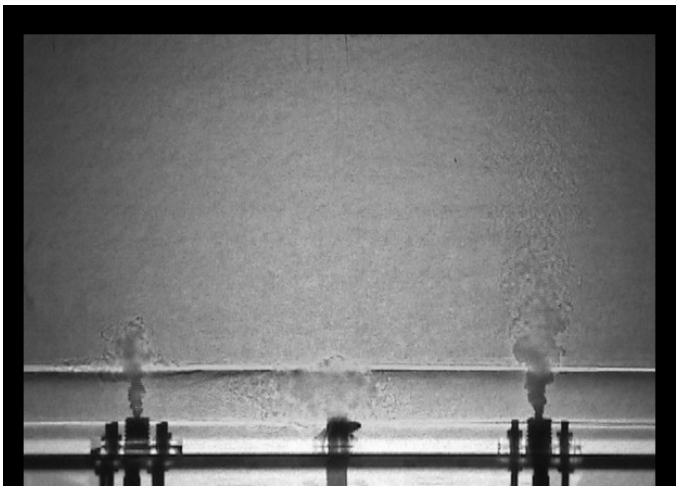

(b)

Figure 4.11: Shadowgraphs of flow within the UFAD enclosure. Two-layer stratification observed in (a) Exp.9 with a single plume and a single diffuser; (b) Exp.10 with a two unequal plumes and a single diffuser ($\psi = 0.2$).

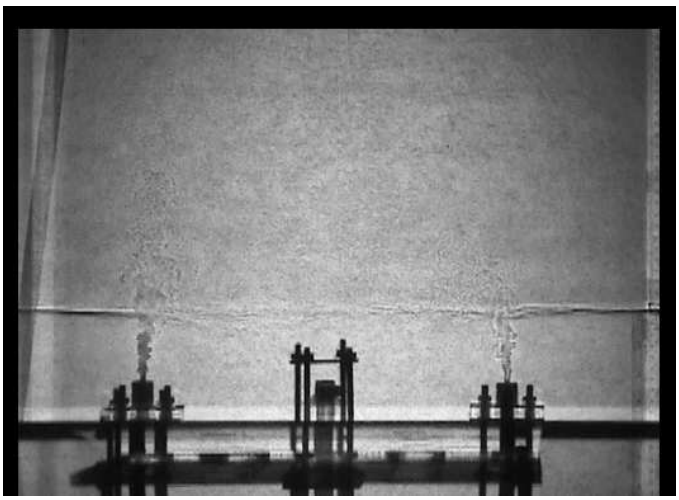

Figure 4.12: Shadowgraph of Exp.11 within the displacement ventilation enclosure, where a metal plate was set beneath the diffuser. The left shadow of a tube is the siphon. Only two-layer stratification was observed when the two plumes have unequal strength ($\psi = 0.26$).

ventilation experiment, we could not see two sharp interfaces (figure 4.12). Since the middle layer in the UFAD case is thinner than that in a displacement ventilation case, it is more difficult to obtain a three-layer stratification in UFAD experiments.

The quantitative comparisons of experimental measurements and theoretical predictions for Exp.4 and Exp.7 are presented below. Non-dimensional height and buoyancy are defined as in (3.11) and (3.12), where B now is the buoyancy strength of the stronger plume.

We first applied the weak diffuser model discussed in § 4.2.1. Figure 4.13 shows the comparisons for Exp.7. It is seen in the figure that the interfaces are predicted very close. This implies that the middle layer is too thin to be resolved by the experiments. And the buoyancy in the middle layer is in the transition from the lower layer buoyancy to the upper layer buoyancy, all of which are well estimated compared with the experimental data. For all the different combinations of parameters, such as ψ, source fluid density g'_s, and the volume flux of the fountain

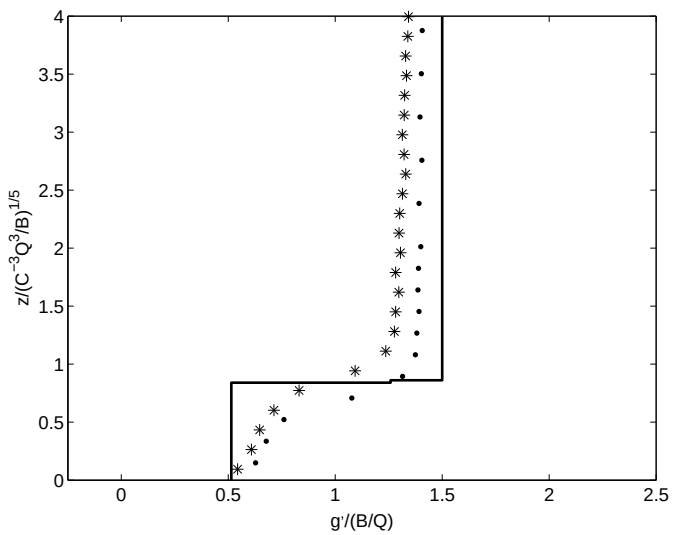

Figure 4.13: The three-layer theoretical predications of Exp.7 ($\psi = 0.5$) when the weak-fountain model is applied.

Q_f, in Table 4.1, the middle layer was not observed. For Exp.4 when the weak-diffuser model is used, no three-layer stratification is obtained. This is because that the diffuser flow in Exp.4 is sufficiently high to penetrate both interfaces, and no interfaces can be found at which the mass conservation equations (4.7) and (4.8) in the weak-diffuser model are valid.

We now compare use the strong-diffuser model described in § 4.2.1. The distribution of entrained fluid is unknown and it was not possible to determine the coefficient β from the experiments. Consequently, different values of β were used to span the possible range for β for the strong-diffuser model. As shown in figure 4.14, theoretical predictions can be obtained by the strong-diffuser model for both experiments. For both experiments, $\beta = 1$ provides good agreements between the predictions and experimental data. Therefore, it seems to be a good assumption to use $\beta = 1$ in the model. This is also consistent with the absence of a middle layer in the experiments.

The theoretical stratification was obtained by using the approximate theoretical model discussed in § 4.2.2. As shown in figure 4.15, the approximate the-

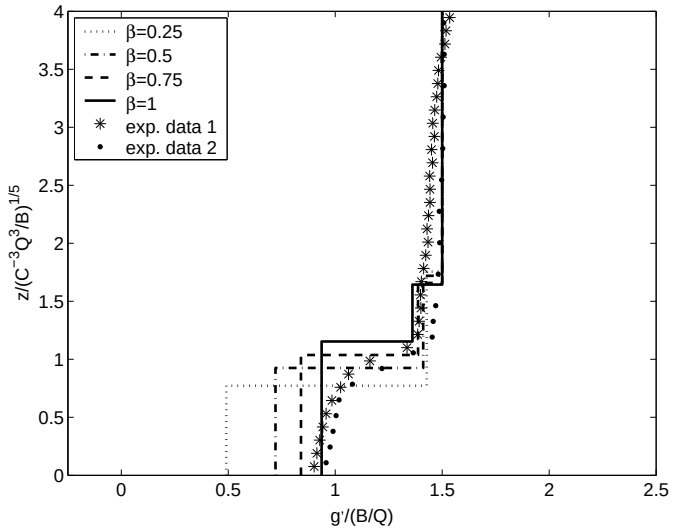

(a)

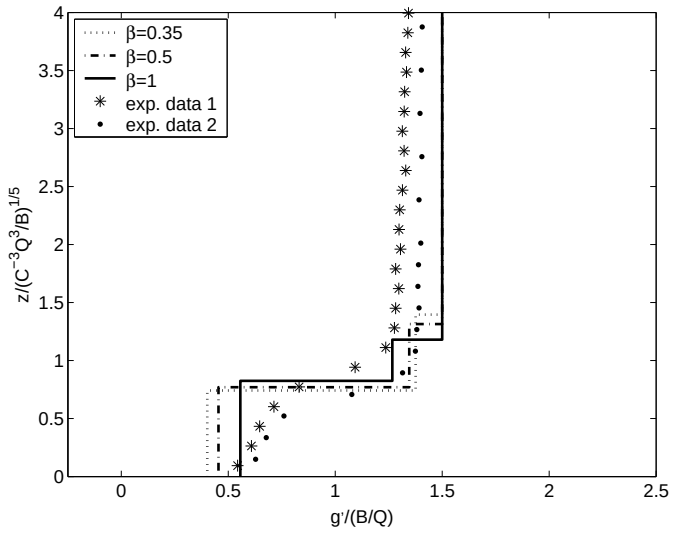

(b)

Figure 4.14: The three-layer theoretical predications of (a) Exp.4 and (b) Exp.7 when the strong-diffuser model is applied. In each plot, experimental data 1 are the measurements using dye attenuation, and experimental data 2 are the measurements with fluid samples.

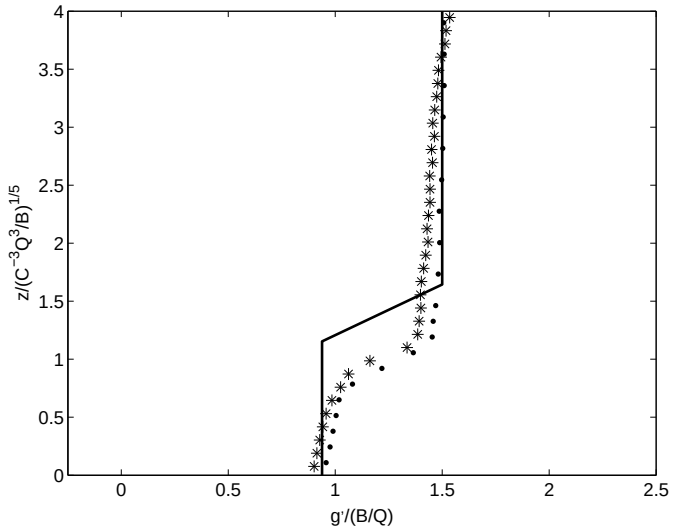

(a)

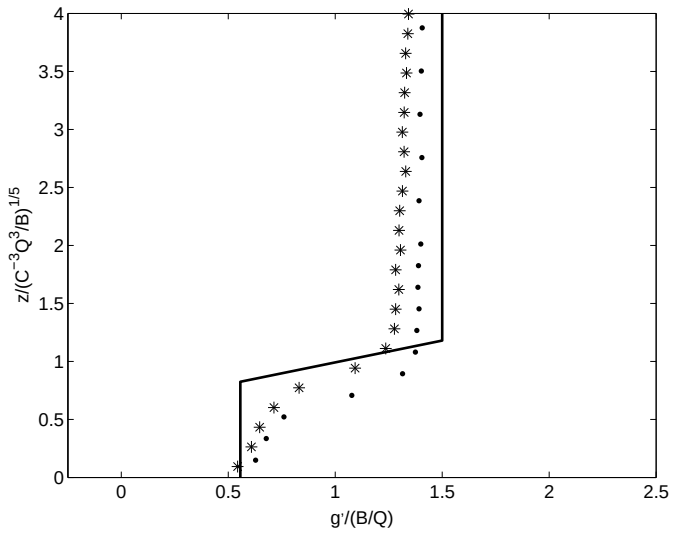

(b)

Figure 4.15: The buoyancy profiles obtained by the approximation model (§4.2.3) for (a) Exp.4 (b) Exp.7.

oretical model for unequal plumes gives good predictions of the buoyancy stratifications for both experiments. The middle layer is predicted to be in the transition region, which agrees well with the experimental measurements. The theoretical non-dimensional reduced gravity of the upper layer is $1 + \psi$ as a result of (4.28). The overestimation of the upper layer reduced gravity mainly comes from the neglect of the source volume fluxes from each plume.

4.4 Scaling analysis

We now consider the situation where the number of plumes exceeds the number of diffusers, thus completing the basic rules found by § 3.2.1 that control the interface height and buoyancy in both layers as a function of n'.

Consider the case where the total heat load is fixed. When m is large, Q_e is small. From (4.1), $mQ_p \sim Q$, thus $\hat{h} \sim m^{-3/5}$. When m is small, Q_e and Q are comparable, which also gives $\hat{h} \sim m^{-3/5}$. Consequently, $\hat{h} \sim n'^{3/5}$. The buoyancy difference between the two layers is obtained by (4.2), (4.4) and (4.1): $\hat{g_2'} - \hat{g_1'} = Q/(mQ_p)$, which implies $\hat{g_2'} - \hat{g_1'} \sim$ constant.

The dimensionless interface height and buoyancy difference are plotted against n' respectively in figure 4.16 (a) and (b). Comparing figure 4.16 with figure 3.6, we note that $n' > 1$ are the multi-diffuser systems, while $n' < 1$ are the multi-plume cases. The case $n' = 1$ is the basic model with one single plume and single diffuser developed by Lin & Linden (2005). As shown in in figure 4.16, the basic model ($n' = 1$) has the largest dimensionless interface height and the smallest dimensionless buoyancy difference. To its left ($n' < 1$), the least-square fit lines imply that $\hat{h} \sim n'^{0.5}$ and $\hat{g_2'} - \hat{g_1'} \sim n'^{-0.2}$. These results are consistent with the power laws we derived above.

Following the same strategy, we obtain $\hat{h} \sim n'^{3/5}$ and $\hat{g_2'} - \hat{g_1'} \sim n'^{-1}$ for the case where the heat load per plume is fixed or the underfloor pressure is constant. These power laws are exactly the same as those for multi-diffuser

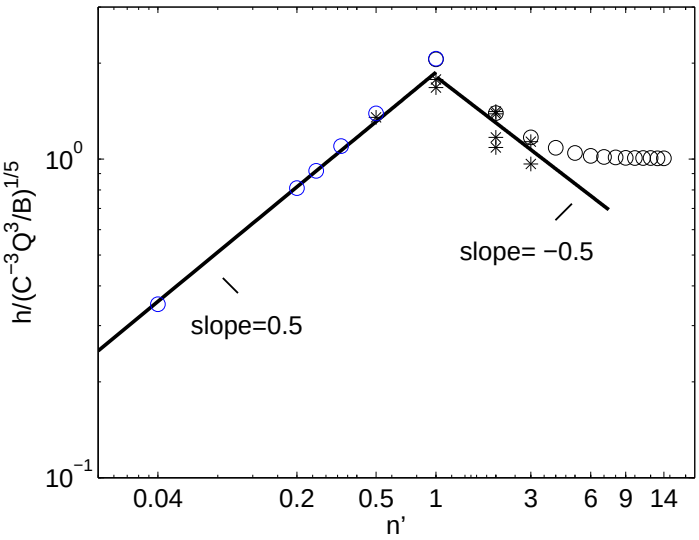

(a)

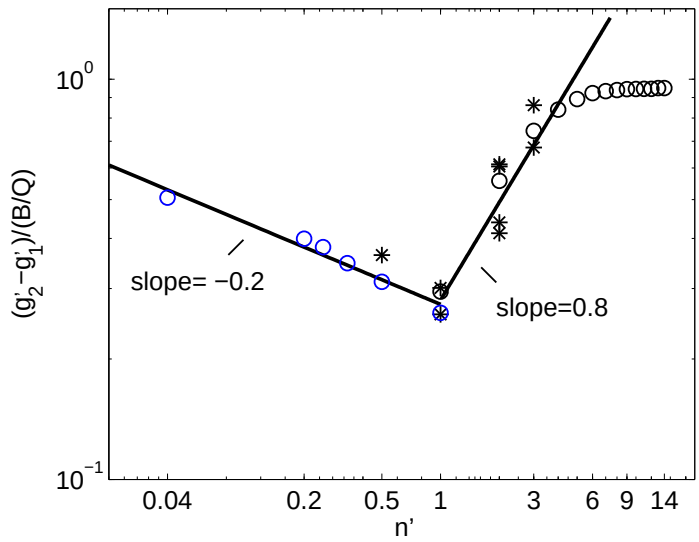

(b)

Figure 4.16: (a) The dimensionless interface height $\frac{h}{(C^{-3}Q^3/B)^{1/5}}$ and (b) the non-dimensional density difference between two layers $\frac{g_2'}{B/Q} - \frac{g_1'}{B/Q}$ plotted against the number of diffusers per plume n' when the total ventilation rate is fixed. The stars are the experimental results and the open circles are the results from the model.

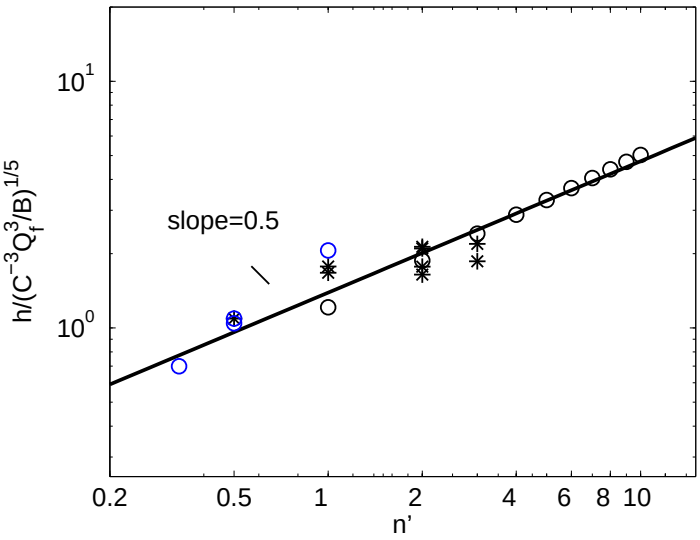

(a)

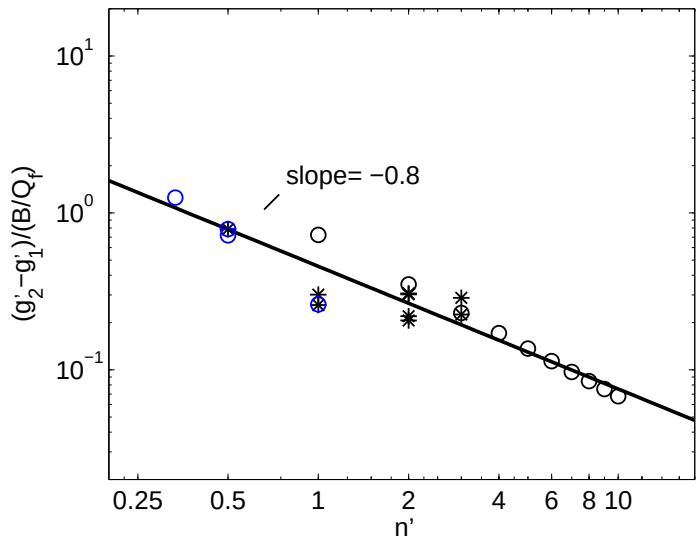

(b)

Figure 4.17: (a) The dimensionless interface height $\frac{h}{(C^{-3}Q_f^3/B)^{1/5}}$ and (b)the non-dimensional density difference $\frac{g_2'}{B/Q_f} - \frac{g_1'}{B/Q_f}$ plotted against the number of diffusers per plume n' with fixed underfloor pressure. The stars are the experimental results and the open circles are the results from the model.

case (Liu & Linden 2006). Figure 4.17 is the extended plot of figure 3.7, which shows the dimensionless interface height and buoyancy difference against n with fixed underfloor pressure. We note that all the data including multi-diffuser and multi-plume systems obey the same rules. Further, the best line fits indicate that $\hat{h} \sim n'^{0.5}$ and $\hat{g_2'} - \hat{g_1'} \sim n'^{-0.8}$, which is consistent with the above scaling analysis.

4.5 Conclusions

In this chapter, we have investigated the behavior of UFAD enclosures containing multiple buoyancy sources. For multiple equal sources, a two-layer model to describe the buoyant stratification within those enclosures has been developed which gives good predictions for the layer buoyancies and interface heights by our laboratory experiments. The model is based on the work of Lin & Linden (2005) for single-source single-diffuser systems, and is the extension of the multi-diffuser model discussed in Chapter 3 since it covers the situation where there are more heat sources than cooling diffusers. In those situations, the number of diffusers per buoyancy source n' is less than 1. The basic scaling rules, that uses the power laws to link the their multi-diffuser model to the single-source single-diffuser model quantitatively, have been extended to cover the entire region of n', where $0 < n' < \infty$.

According to the strength of the diffuser flow, we developed two theoretical three-layer stratification models for UFAD enclosures with two unequal buoyancy sources and single diffuser. With the weak-diffuser model, the diffuser flow only penetrates the lower interface. The ratio of the buoyancy strengths of two plumes ψ ($0 \leq \psi \leq 1$), is found to decrease the middle layer thickness if ψ is small; and to diminish the density contrast of the upper two layers if ψ is large. This explains the fact that a three-layer stratification for two unequal buoyancy sources could not be resolved in our laboratory experiments. With a strong-diffuser model, the diffuser flow impinges to the top layer. In this case, the amount of the

entrainment by the diffuser flow back to the bottom layer β which is an empirical coefficient, is hard to determine. Therefore, we presented an approximate two-layer model with the assumption that $\beta = 1$ for the stratification, which is equivalent to assuming that all the penetrative entrainment goes back to the bottom layer. With this model, only the lowest and highest interfaces and buoyancies of the top and bottom layers are calculated, and the interior stratification is considered to be a transition region. The model is compared with the experimental measurements for the case of two plumes (figure 4.15). It is found that the two interfaces have predicted the transition region accurately. Although the behavior of the entrainment fluid by the diffuser flow in a multi-layer configuration is not yet understood, the analysis in this paper shows that it is possible to calculate the flow stratification for multiple unequal buoyancy sources within UFAD enclosures. From the practical point of view, the height of the lowest interface is the critical parameter. As shown in figure 4.15, the approximate model has given reasonable predictions on the lowest interface position. This estimate should be adequate to calculate the stratification for any number of unequal sources of buoyancy within a UFAD space.

Chapter 5

The Perimeter Zone Model — Line Source & Single Diffuser

In previous two chapters, we discussed the interior zone model in a UFAD system. In this chapter, the perimeter zone in a UFAD enclosure will be modelled by introducing a line source to represent the radiation by the sun into the space.

Nowadays, architects tend to use glass for the facade design. The huge use of glazing in buildings causes large solar heat gains on the windows, the walls and the floors in the perimeter zone of a room. The perimeter zone is typically considered to be the region up to 5 m from the wall. The accumulated heat load on large surfaces is quite different from the separated heat sources in the interior zone, and it is difficult to simulate this surface heating in our laboratory experiments. In the laboratory experiments, we use a line plume to simulate this window/floor heating. Thus we are representing the solar gains on a window say as originating at the base of the window. This is done for convenience because it is very difficult to simulate heated surfaces using salt fluxes. Another difference between the interior zone and the perimeter zone is that the swirl Krantz diffusers are the only way cool air is introduced into the interior zone. In addition, linear bar grilles (figure 5.1) are commonly installed close to the wall. Visual observation of the performance of linear grilles suggests they disrupt the operation of a UFAD system during cooling.

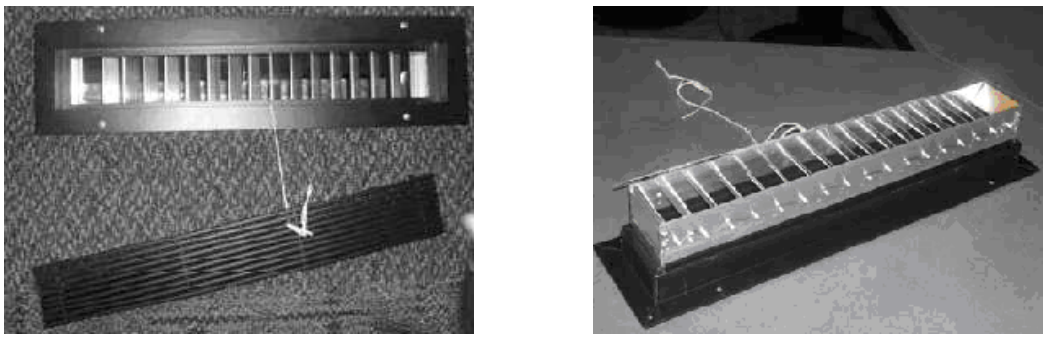

(a) (b)

Figure 5.1: (a) A Titus CT-481 linear bar grille; (b) the linear bar grille equipped with optional adjustable vanes. It is 0.46 m (18 in) long, and 0.09 m (3.5 in) high, with a 15° discharge angle. The vanes are used to change the direction of air flow to either the right or the left. An adjustable damper assembly was attached to the bottom of the diffuser via a string which could be used to change the amount of air going through the bar grille (Webster *et al.* 2006).

Consequently, we restrict our study to interior cooling diffusers.

5.1 Theoretical model about a UFAD perimeter zone

5.1.1 Line plumes

We assume that the solar heat gains on the windows and walls can be aggregated over the wall height and represented by a line source of heat at the base of the wall. A two-dimensional line plume with the source buoyancy flux per unit length B_L has velocity, buoyancy and width given by

$$w \sim B_L^{1/3}, \;\; g' \sim B_L^{2/3} z^{-1}, \;\; b \sim z,$$

which indicate that the velocity scale is independent of height z, the density difference varies inversely as z, and the transverse dimension b is linear with z.

The volume flux per unit length

$$Q_L \; = \; D B_L^{1/3} z, \tag{5.1}$$

where, z is the vertical height and $D = (2\alpha_l)^{2/3}$ is a universal constant dependent on the entrainment coefficient of a line source α_l (Linden *et al.* 1990), which is determined by experiments.

Rouse, Yih & Humphreys (1952) conducted experiments with two-dimensional plumes, which suggest that the full solutions with Gaussian profiles are

$$\begin{aligned} w &= 1.8 B_L^{1/3} \exp\left(-32x^2/z^2\right), \\ g' &= 2.6 B_L^{2/3} z^{-1} \exp\left(-41x^2/z^2\right), \end{aligned} \tag{5.2}$$

where, x is the horizontal distance from the plume center. However, Turner (1973) does not think that these experiments are accurate enough to be sure that the suggested greater spread of velocity relative to buoyancy is real, and indeed the fluctuations of these plumes makes the estimate of an entrainment constant from the profiles very inaccurate.

A direct estimate of entrainment was suggested by the experiments of Ellison & Turner (1959) as $\alpha_l = 0.08$ for top hat profiles. I have tested our theoretical model, which will be described in next section, against experimental data for different α_l. Figure 5.2 shows the comparisons for Exp.1 in table 5.1. We found that the interface position is very sensitive to α_l while the lower layer buoyancy is relatively insensitive, and $\alpha_l = 0.06$ whon as the solid profile, which is not very different from Ellison & Turner's (1959) value, provides a fairly good agreement between the theoretical predictions and the results of the experiment. The sensitivity of the interface height results from the different entrainment rates into the fountain for different values of α_l. Comparisons with all the other experiments in table 5.1 show similar results, and the best agreement is found with $\alpha_l = 0.06$. Thus, $\alpha_l = 0.06$ is used throughout this study for a UFAD system containing a line plume source.

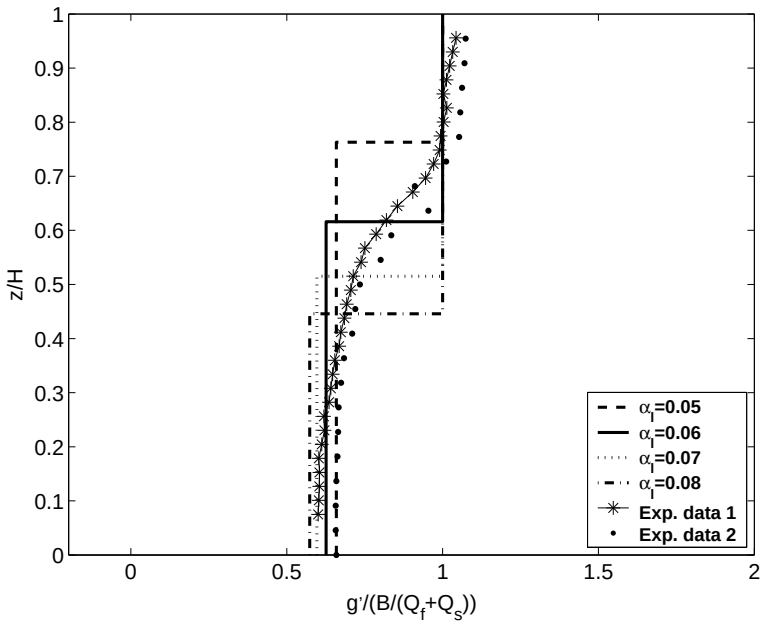

Figure 5.2: The theoretical stratification predictions for Exp.1 in table 5.1 with different values of α_l. As shown in the figure, $\alpha_l = 0.06$ gives the best agreements with experimental data. The experimental data were obtained with dye attenuation technique (data 1) and with fluid samples measurements (data 2).

5.1.2 UFAD perimeter zone model

In a UFAD system, walls and the floor are heated by the sun, thus affecting the stratification in the space. The effects of these distributed sources in the perimeter zone has not been theoretically studied, although they are important to estimate the cost and the efficiency of the system. In this section, we describe a model of a UFAD enclosure with a line plume against a sidewall, and a single cooling diffuser, which is the simplest case we can consider (figure 5.3). This setup allows the line plume to be compared with or treated as extension of a point plume. However, since a real perimeter zone which includes wall plumes and linear bar grilles, this model only provides preliminary understanding of the perimeter zone stratification, and more realistic things need to be done in future.

Linden *et al.* (1990) proposed that if a horizontal line source is against a vertical wall since the wall acts as a plane of symmetry, the plume can be considered as half of a line source whose buoyancy flux is twice that of the true source. When we add the reflection of the line source on the other side of the wall as shown in figure 5.3, the total buoyancy flux will be $2B$, and the total volume flux in the plume is $2Q_p$, where Q_p is the volume flux of the real line plume in the tank at the interface height h. Therefore, based on (5.1),

$$Q_p = \frac{1}{2}D(2B/d)^{1/3}hd = \frac{1}{2^{2/3}}DB^{1/3}hd^{2/3}, \tag{5.3}$$

where, B and d are the total initial buoyancy flux and the length of a line plume, respectively. Here, the buoyancy per unit width $B_L = B/d$. We used the total buoyancy flux B because the return temperature T_r is determined by B instead of B_L. In a real room, usually the heat per unit area B_a(W/m^2) is given. Then, the total heat load is the product of the heat per unit area and the wall/floor area, i.e., $B = B_a \times A_{wall}$.

A two-layer stratification is assumed to form at steady state, and further confirmed by our experiments as shown in figure 5.5. Volume conservation gives that, as in the case of a point source plume,

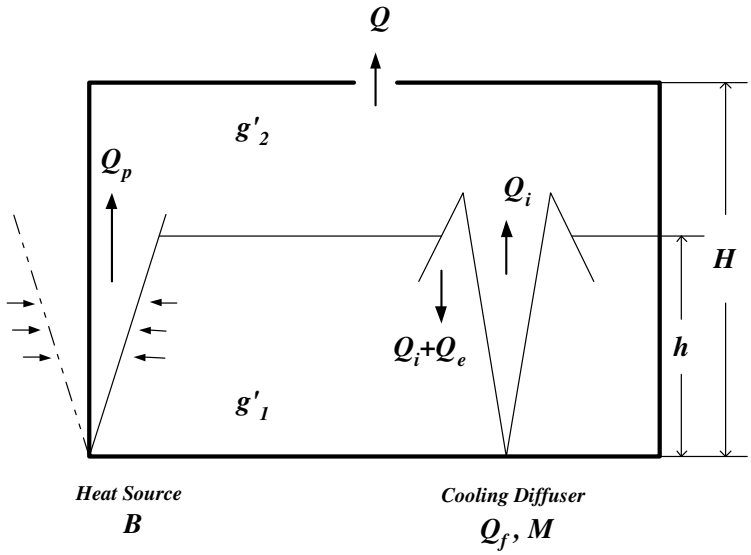

Figure 5.3: A UFAD system with a line plume and a single cooling diffuser.

$$Q_p = Q + Q_e, \tag{5.4}$$

where, $Q = Q_f$ is the total ventilation flow rate in the room, Q_p in this case is defined in (5.3) and Q_e is the penetrative entrainment by the fountain, defined in (1.39).

The reduced gravity of these two layers are

$$g_2^{'} = B/Q, \tag{5.5}$$

and

$$g_1^{'} = \frac{g_2^{'} Q_e}{Q_e + Q_f}. \tag{5.6}$$

Here, (5.5) and (5.6) are the same as those in a simplified UFAD model containing one point source and one fountain by Lin & Linden (2005). The reason for the unchanged formulas is that the reduced gravities of both layers are only determined by the buoyancy flux of the source, and the momentum flux of the

fountain, which is independent of the form of the buoyancy source. The difference between the two types of buoyancy sources is the equation to determine Q_p, thus the entrainment behavior by different plumes. We retain the same parameterization for the penetrative entrainment rate $E(Ri)$ for the fountain at the interface as (2.11) in the interior zone because of the use of the same diffuser.

5.2 Experimental results

Our line-plume experiments were carried in the smaller tank "A" with uniform cross-sectional area 30.6 cm $\times$15.3 cm and 30.6 cm deep. The distributed plume nozzles are 31 straight tiny holes (diameter 1 mm) with 5 mm interval on a thin tube (diameter 6 mm). The thin tube with the length 15 cm, as shown in figure 5.4 was fitted to a end wall of the tank to provide the wall plume shown in figure 5.3. Salt solution from a constant-head system comes into the thin tube and flows out from holes to form a two-dimensional plume flow. It was observed in initial experiments that a region of laminar streams occurred below the orifices of the holes, even though the tube has been wrapped by a piece of mesh. Therefore, a pulse generator was used in order to make the flow coming out of the line source turbulent. This pulse generator uses a voltage of 30 V, and was placed under a tube which connects between a flowmeter and the line source. The pulse frequency is about 2/s, and with each pulse, a tip on the pulse generator pushes the tube. We made sure that the shaking is very gentle but is enough to make the laminar streams at the orifices vanish.

The diffuser nozzle is the same as that described in §2. It was located far enough from the line plume to avoid direct interference. In some experiments the diffuser was located close to the line source to study the effects of the interference between the wall plume and the diffuser flow, because in a real UFAD room, usually linear bar grilles are installed very close to the wall. The interference of the flows by the line sources and the diffuser was qualitatively examined in this research.

Exp. No.	ρ_s (g/cm^3)	Q_s (cm^{3}s^{-1})	B (cm^{4}s^{-3})	Q_f (cm^{3}s^{-1})	plume form	diffuser and line/point plume
1	1.06435	1.89	122.9	21.9	line	apart
2	1.06468	1.89	122.9	23.9	line	apart
3	1.06497	1.68	108.9	21.9	line	apart
4	1.06537	0.98	64.8	12.1	line	apart
5	1.06560	0.98	65.1	9.10	line	apart
6	1.04072	1.97	83.2	15.5	line	apart
7	1.04089	1.97	83.2	15.5	line	close
8	1.04170	1.76	75.5	15.5	line	apart
9	1.08120	0.85	69.3	15.2	point	apart

Table 5.1: Nine different experimental conditions for the line plume studies. ρ_s, Q_s and B are the densities, buoyancy fluxes and volume fluxes at the source of the line plume; Q_f are the initial volume fluxes of the cooling diffuser.

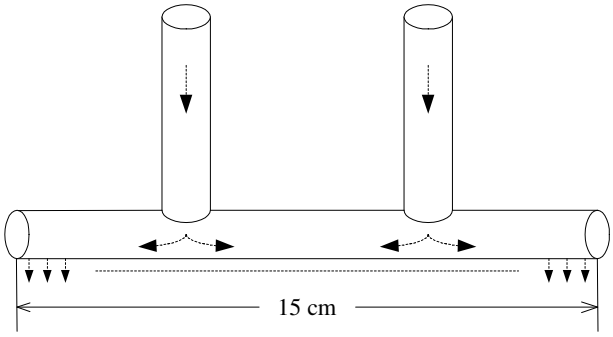

Figure 5.4: A line plume nozzle used in a salt-tank experiment. Arrows show the flow direction. All holes are facing down along a straight line.

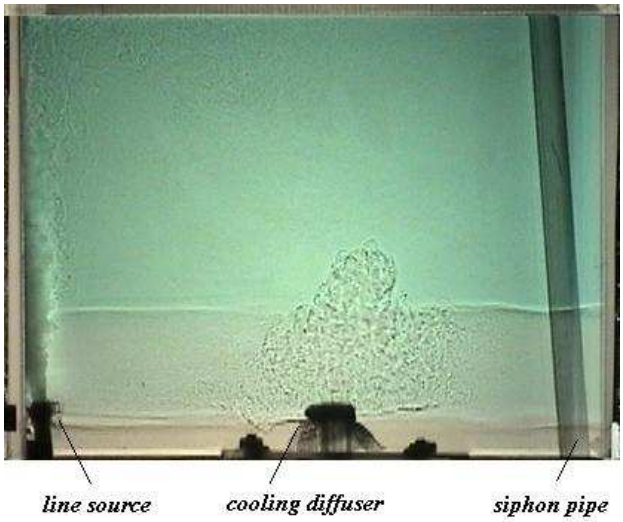

Figure 5.5: An image of a salt tank UFAD experiment with a line plume and a diffuser far in the steady-state.

To be consistent with previous chapters, in the following graphs, solid lines or '$\circ$' indicate the theoretical predictions, '$*$' are the experimental measurements analyzed by *DigImage* (Dalziel 1992-1998, Dalziel 1992-1998), and '$\cdot$' are the measurements of fluid samples by an Anton Paar DMA 5000 density meter, accurate to 10^{-5} g cm^{-3}.

The same dimensionless height and buoyancy as defined in §3.2.2 are used here so that

$$\hat{z} = \frac{z}{H}, \tag{5.7}$$

and

$$T/T_R \equiv \hat{g}' = \frac{g'Q}{B}. \tag{5.8}$$

5.2.1 Qualitative observations

The line plume was placed beside the left side wall (figure 5.5), and the fountain was located at the center of the tank. The two sources were both at

the floor level and horizontally far enough from each other so that they did not interact. After the sources were turned on, the fluid from the distributed source entrained the ambient fluid as it rose, and spread out to the right when it reached the top of the tank. Thus, the ambient fluid was pushed down and a density interface established in the tank in the same fashion as for a point source. The flow from the fountain nozzle penetrates the interface and entrained some of the upper layer fluid to the lower layer. A two-layer stratification was observed in all experiments listed in table 5.1.

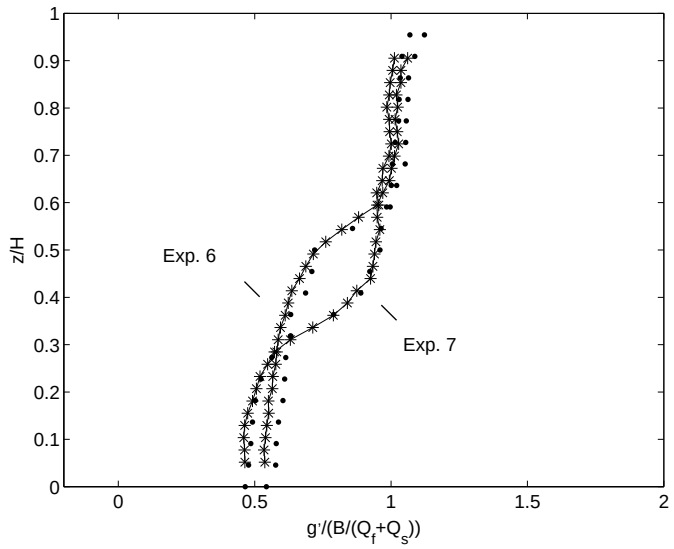

Figure 5.6: The effects of the position of a cooling diffuser – comparisons between Exp.6 with the diffuser apart from the wall and Exp.7 with the diffuser close to the wall.

We studied qualitatively the effects of the horizontal position of a diffuser on the stratification in a UFAD system. Figure 5.6 shows the measured profiles of Exp.6 and Exp.7. These two experiments have the same total heat load B and ventilation flow rate Q, but the cooling diffuser was positioned away from the line plume in Exp.6, while in Exp.7, it was 1.5 cm away from the line plume. We show the interaction between the line plume and the diffuser flow in figure 5.7. As we see in figure 5.6, the return temperature $g_2^{'}$ is the same in both experiments since

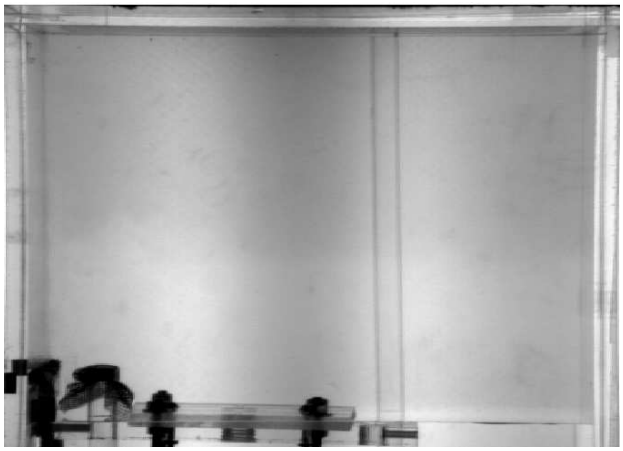

Figure 5.7: An image of a salt tank UFAD experiment with a line plume and a diffuser close in the steady-state.

B and Q are the same and the occupied zone temperature $g_1^{'}$ does not change significantly. However, the temperature interface (the occupied zone height) drops significantly when the diffuser is located close to the line source. In this case, the fountain flows entrains not only the ambient fluid but also the light fluid in the two-dimensional plume as it ascends. The mixing of the ambient fluid and the plume fluid reduces the fountain negative source buoyancy flux, thus forcing the fountain fall back at a lower level with a smaller Q_i and Q_e. According to (5.4), Q_p decreases, and consequently, h decreases. This comparison suggests that in a real UFAD room, placing diffusers close to the wall is not beneficial to the occupants since this arrangement lowers the interface, thereby causing problems of comfort and efficiency.

5.2.2 Quantitative comparisons

In this section, we will compare our experiments containing a line plume with the model discussed in §5.1. Exp.1 and Exp.2 are two experiments with the same total heat load B but different ventilation flow rate Q ($Q = Q_f$). Figure 5.8(a) shows the comparisons of the steady-state buoyancy profiles of this pair of

experiments. From the figure, we see that Exp.2 with a larger Q has a higher interface position. This is because Q_e increases with Q_i which increases with a higher source momentum flux of the diffuser flow. Therefore, the interface rises as a result of a larger Q_p based on (5.4). The same dimensionless return temperature $\hat{g_2'}$ was observed, which is consistent with the non-dimensional buoyancy definition (5.8). The dimensionless occupied zone temperature ($\hat{g_1'} = Q_e/Q_p$) was found to be close in these two experiments. The same trends are found in another comparisons between Exp.4 and 5, as shown in figure 5.8(b). The interface is higher in Exp.4 with a larger ventilation flow rate, but the lower layer temperature does not change much. This means that increasing the ventilation air flow can increase the interface height effectively, with only a small effects on the lower layer temperature. It may cause system inefficiency in case of large ventilation air flow since upper space is cooled unnecessarily.

Now we will study the effect of different heat loads with the same ventilation rate. As shown in figure 5.9, Exp.1 and Exp.3 have the same ventilation rate Q, but the total heat load B in Exp.1 is larger than that in Exp.3. The non-dimensional buoyancy profiles of these two experiments almost collapse. The upper layer buoyancy $\hat{g_2'}$ is the same as expected. The slight difference change in $\hat{g_1'}$ and $\hat{h}$ can be explained by the small change of B from 122.9 cm^{4}s^{-3} to 108.9 cm^{4}s^{-3}. Although the difference is small, we noticed that Exp.1 with a larger B has a lower interface. Thus, the interface height is more sensitive to the change of the total heat load B compared with the lower zone buoyancy g_1'.

Finally, we study the effect of different plume forms. Exp.8 and Exp.9 are two experiments with a line plume and a point plume, respectively. The same point diffuser was used in the experiments. Ideally, all parameters for a perimeter zone should be expressed per unit length if linear bar grille diffusers are used. However, this case has not been simulated in our laboratory experiments. Thus we use total buoyancy B and total ventilation rate Q, which are similar in these two experiments, to compare the non-dimensional stratification profiles as shown

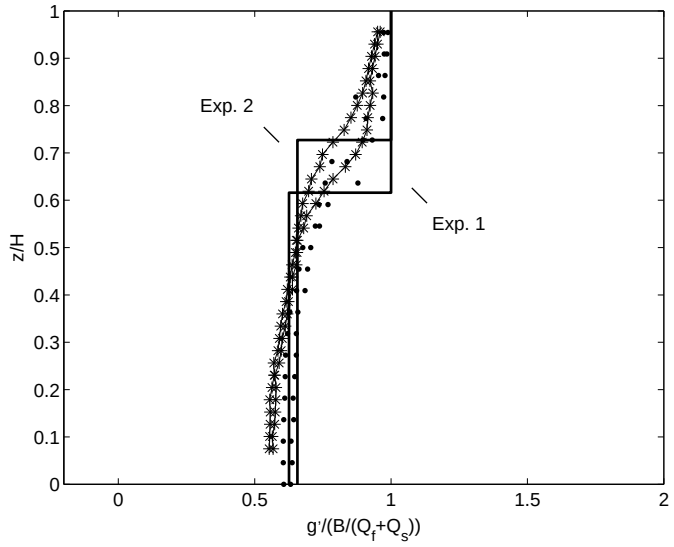

(a)

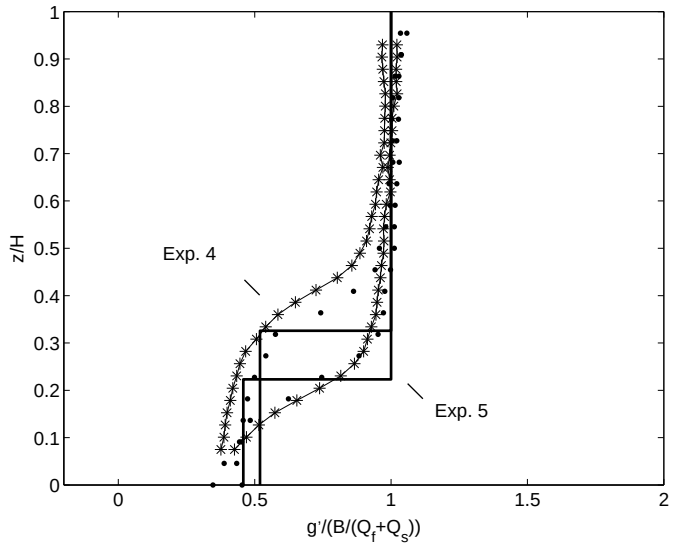

(b)

Figure 5.8: Buoyancy profiles obtained at steady state with a line plume. Each pair of experiments have the same total heat load (B), but different total ventilation flow rate (Q). The height is made dimensionless by the height scale H, and the buoyancy by the buoyancy scale B/Q. (a) Comparisons between Exp.1 and Exp.2; (b) Comparisons between Exp.4 and Exp.5.

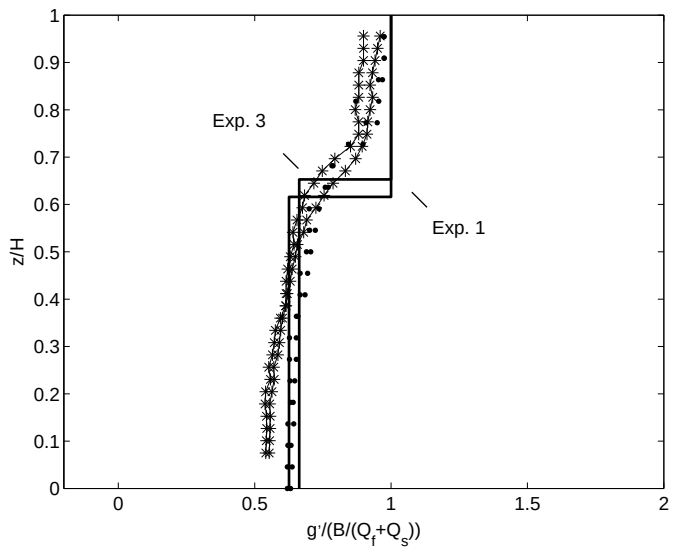

Figure 5.9: Non-dimensional buoyancy profiles comparisons between Exp.1 and Exp.3.

in figure 5.10. The upper layer reduced gravity is about the same, for these two experiments as expected. The interface is lower for a line plume experiment case because of a larger entrainment behavior of a line plume. Also the lower layer temperature is reduced compared with the point-source plume. This behaviour is noted in both the experiments and the theoretical models. However, the theoretical predictions for Exp.9 with a point plume agree better with the experimental data.

Our theoretical model gives good agreements with all experimental data.

5.3 Conclusion

A UFAD perimeter zone needs a separate study because it is different from the interior zone in that the heat source is not a point source, but a area source. Since it is difficult to do experiments with a wall plume to simulate the area source, we assumed that the heat on a surface accumulates to an end line so that a line plume source is used in our small-scale laboratory experiments. We did experiments to study the effects of the distance between the diffuser and the wall,

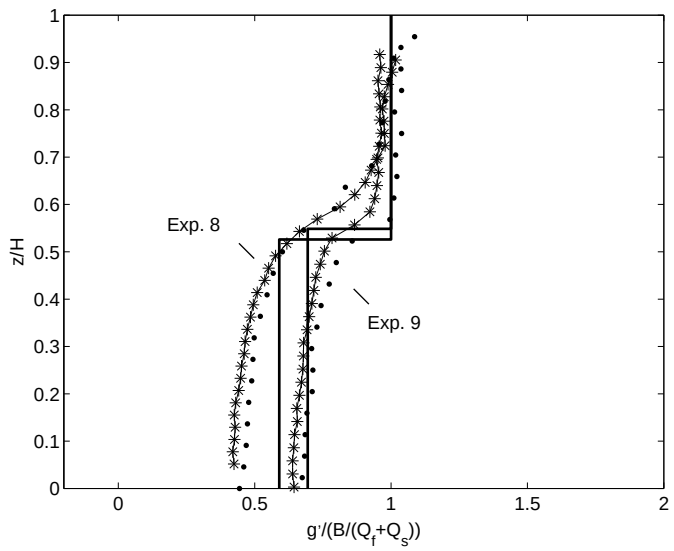

Figure 5.10: Non-dimensional buoyancy profiles comparisons between Exp.8 with a line plume and Exp.9 with a point plume.

of the ventilation flow rate and the type of heat sources. We developed a UFAD perimeter zone model for the flow at steady state generated by a single distributed source and a single cooling diffuser in the space in order to provide a better understanding of the perimeter zone in the model. Both qualitative observations and quantitative predictions of the UFAD system are presented. The theoretical model gives reasonable agreements with our experimental data.

Chapter 6

The Comparisons between Small-scale & Full-scale Experiments

In this chapter, we will present comparisons between small-scale salt tank experiments and full-scale real room tests, with the objective of determining whether the laboratory scaling matches the full-scale scaling of a room. The conditions in the test chamber (as well in a real room) are considerably more complicated compared with those in our small-scale salt tank, because of heat exchanges through walls and floors, because of the fact that the heat sources are different from ideal plumes and because the diffuser flows have uneven supply air temperatures. In addition, airflow leakage occurs from the plenum both into the test chamber and to the exterior. The objective is to determine whether the salt-tank experiments and the theoretical model have captured the most critical characters of the stratification of a full-scale UFAD system and to test the non-dimensional scalings, in the laboratory and the test room.

In this chapter we describe some comparisons, both qualitative and quantitative, between the flow and stratification in the laboratory and the test room. First, we compare pictures from experiments at both scales. This shows that two-

zone stratification forms at steady state. Secondly, we test our theoretical model against the test chamber experiments. Finally, for multiple-diffuser cases, the same changing trend of the stratification profiles were found in experiments with both scales. Non-dimensional scaling comparisons were described for both interior and perimeter zones. In each zone, we define non-dimensional parameters Γ and ϕ describing the inputs of the system and the resulting stratification of the space, respectively. The experimental data from the laboratory experiments and the test room fall on a unique relationship of Γ and ϕ, which provides explicit equations to determine the room stratification. These equations have been used in EnergyPlus, a whole-building software developed by the U.S. Department of Energy for building energy simulation.

The effects of floor airflow leakage, which is a major concern in the design of a UFAD system, were also studied theoretically and experimentally.

The analysis of the full-scale test data is still continuing. We have only chosen some of the more simple tests to compare with our laboratory experiments. Therefore, all the comparisons presented in this chapter are preliminary.

We have worked closely with Fred Bauman and Tom Webster, from the Center for the Built Environment (CBE) at the University of California, Berkeley, in this comparison project on UFAD systems. We are grateful for the intellectual companionship they have provided in this work.

6.1 Full-scale tests

The full-scale room air stratification tests were carried out in a 63 m^2 (676 ft^2) test chamber with a height of 2.7 m (9 ft) operated by York International (figure 6.1). Temperature sensors, manikins, personal computers, desk lamps and other equipment were placed in the room to simulate typical office arrangements. Interior spaces were simulated by putting foam insulating panels on the west window wall and over the windows on the south wall. For perimeter zone tests, the west window

panels were removed and the window was heated by solar-simulation lamps. There are 6 workstations in the test room. Each workstation consists of a manikin, a personal computer and a desk lamp (figure 6.2). Four different types of diffusers were used – Krantz standard swirl (up to 16 in total in the room) (figure 6.3), Krantz Displacement Ventilation swirl (up to 14), York MIT (up to 10), and Titus linear bar grille (up to 10). Linear bar grille diffusers are typically used to perimeter zones in UFAD systems. They are usually installed close to the perimeter wall. In order to measure the vertical temperature distribution, thermocouples were installed at different heights on a mast to form a so-called "thermocouple tree". This mast was clamped between the ceiling and the floor. There were a total of 7 thermocouple trees in the room as shown in figure 6.1, one of which is on movable stand. For perimeter tests, shields were installed on the thermocouples to mitigate the effects of radiation biases.

The Center for the Built Environment (CBE) at the University of California, Berkeley was responsible for those tests. They kindly provided us with some of the experimental measurements which are shown in tables 6.1 and 6.3.

Test No.	W(kW)	SAT(K)	Q_t(m^3/s)	Q_r(m^3/s)	Q_d(m^3/s)	m	n
PG-H5-9	1.22	292	0.139	0.135	0.129	4	8
PG-H5-10	1.23	292	0.163	0.146	0.122	4	2
PG-H5-11	1.22	292	0.144	0.133	0.118	4	6

Table 6.1: UFAD room test results provided by CBE. W is the heat load. SAT is the supply air temperature. Q_t, Q_r and Q_d are the total supplied airflow, the airflow into the room and the airflow coming from the diffusers, respectively. The number of the heaters and diffusers are m and n, respectively.

In order to provide data for comparison with the laboratory experiments a series of tests was done with convector heaters providing the heat sources. Up to 4 heaters were used to give a maximum total heat load 1250 W. The heaters were placed on the floor or on a table, facing in at corner or distributed out in the center of the room chamber. Up to 8 diffusers were used, and the room airflow ranged

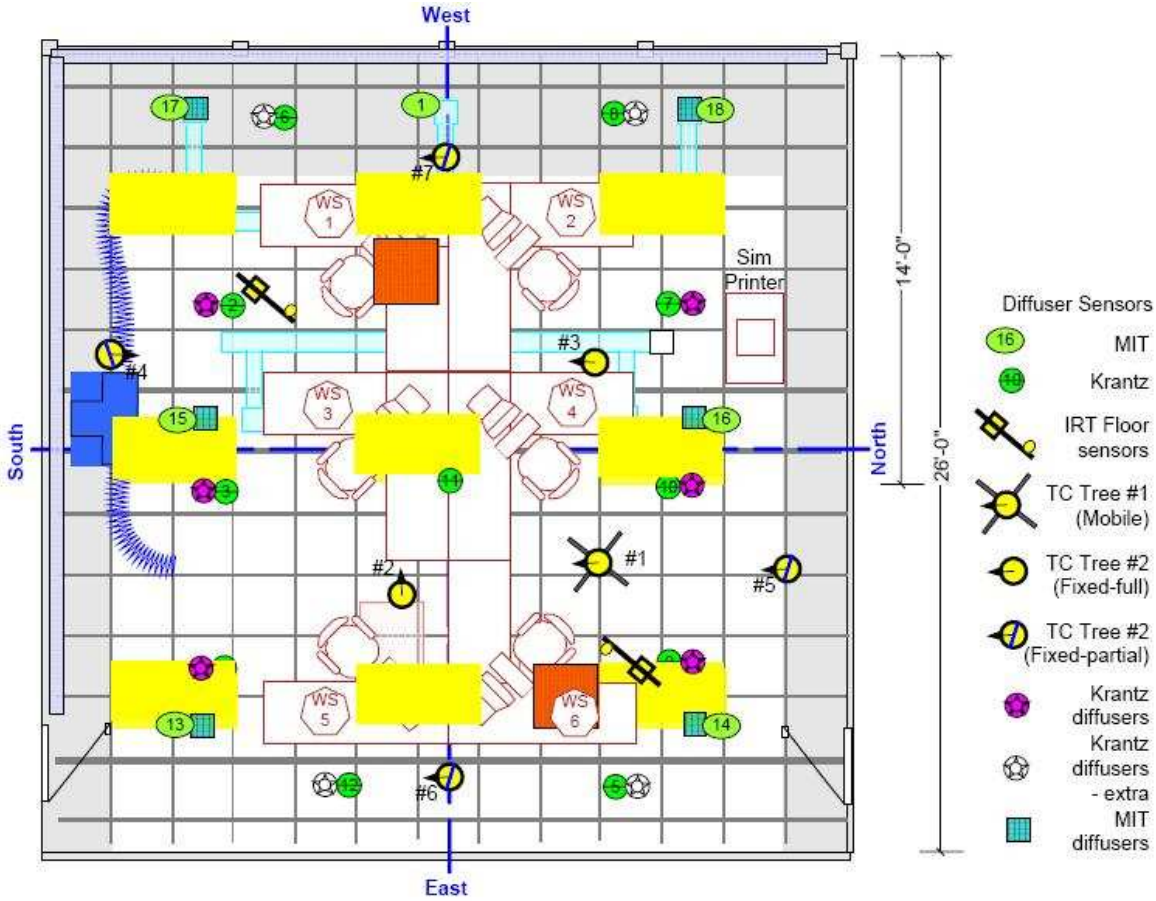

Figure 6.1: The office test chamber layout for interior zone testing (Webster *et al.* 2006).

between 0.71×10^{-1} to 1.63×10^{-1} m^3s^{-1}. The tests that most closely correspond to the laboratory experiments are those in which, the heaters were placed on the floor, standard Krantz swirl diffusers were used, overhead lighting was turned off, and the chamber was empty apart from the heaters. The selected three tests are listed in table 6.1. All room temperature profiles in the following comparisons are the average measurements from the 7 thermocouple trees.

Figure 6.2: A typical workstation in the test chamber (Webster *et al.* 2006).

6.1.1 Equivalent parameters

Consider a UFAD room with a heat load W(kW); the buoyancy flux $B(\mathrm{m}^4\mathrm{s}^{-3})$ can be converted by the formula

$$B = 0.0281W, \tag{6.1}$$

if a single heat source or a set of isolated heat sources are considered. The momentum flux

$$M = \frac{Q_d^2}{A_d}, \tag{6.2}$$

where Q_d is the flow rate through a single diffuser (i.e. the total airflow rate divided by the number of the diffusers), and A_d is the open area of a single diffuser.

Figure 6.3 shows a Krantz standard swirl diffuser. The open area of this diffuser includes 16 small slots and 16 big slots. I measured an area of the slots. The area of each small slot is about $(7.0 \times 10^{-3}) \times (3.90 \times 10^{-2}) = 2.7 \times 10^{-4}$ m^2

Figure 6.3: A Krantz floor swirl outlet. The outlet is installed in the upper surface of the underfloor plenum, called the "raised floor". The surface of the diffuser is flush with the floor and not tilted as shown here. The orientation of the slots (at an angle of 35°) imports swirl to the flow. In typical operation the Reynolds number of the flow from the slots is approximately 8300, and the flow is observed to be turbulent (see figure 6.4).

and each big slot has the area of $(7.0 \times 10^{-3}) \times (6.40 \times 10^{-2}) = 4.5 \times 10^{-4}$ m^2. So the total open area of the outlet is $A_d = (2.7 + 4.5) \times 10^{-4} \times 16 = 1.2 \times 10^{-2}$ m^2 so that the effective radius $b_0 = \sqrt{\frac{A_d}{\pi}} = 6.2 \times 10^{-1}$ m.

Because all slots are made with an angle θ to vertical direction, the supply air is swirling through the outlet. I measured θ, and obtained that $\cos\theta = \frac{14}{17}$. Therefore, the vertical component of the momentum flux is

$$M = \frac{Q_d^2}{A_d}\cos\theta = \frac{14}{17}\frac{Q_d^2}{A_d}. \tag{6.3}$$

6.1.2 Airflow leakage

In pressurized plenums, the central air handling unit (AHU) is controlled to maintain a typically small but positive pressure in the underfloor plenum com-

Figure 6.4: The diffuser flow visualized by smoke tests comes from a swirl Krantz diffuser in the test room (Webster *et al.* 2006).

pared to the conditioned space. However, a substantial air leakage from pressurized plenums, if uncontrolled, can impair system performance. Leakage occurs from the plenum into the test chamber through cracks between raised floor panels, and to the exterior region. Installing carpet tiles on top of the raised floor serves to reduce leakage from the plenum into the room. A pressurized plenum was used in the test chamber. From the data in table 6.1, the leakage outside the room is about 3.1% $\sim$ 10% of the total room airflow; and the leakage through the floor is 7.2% $\sim$ 25% of the total room airflow. These values, especially the latter, are typical of most installations.

6.1.3 Heat loss

In order to calculate the heat loss through the walls of the chamber, series of idealized plume ("plume generator" tests) tests were conducted by using the same heaters to generate plumes. The profiles for this case were more classically shaped. These tests were carried out in open loop control mode; i.e., uncontrolled at a given entering airflow and supply temperature. The heat loss was determined by measuring the difference between the heat extracted $Q(T_{return} - T_{supply})$ and the

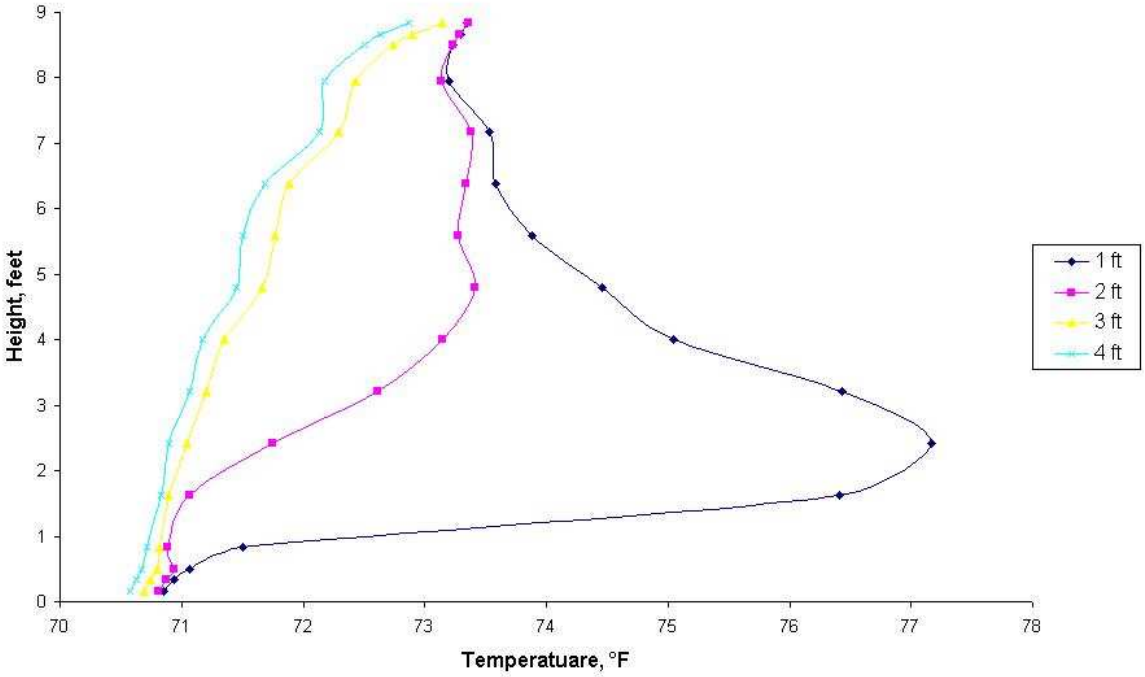

Figure 6.5: The temperature profile in front of a heater with the power of 315W (provided by CBE).

power of the heaters. This is a difficult measurement to make accurately, especially as some of the test room was exposed to the exterior.

CBE estimates that the heat loss is in the range $8.07 \times 10^{-3} \sim 1.08 \times 10^{-2}$ kW/m^2 (0.75 $\sim$ 1.00 w/ft^2).

In our model, we assumed that 9.15×10^{-3} kW/m^2 (0.85 w/ft^2) were lost through the floor. Since the room area is 63 m^2, the total heat loss

$$W_l \;=\; 9.15 \times 10^{-3} \times 63 = 5.76 \times 10^{-1} kW, \tag{6.4}$$

which is almost 50% of the total heat load. This large proportion implies that there is considerable uncertainty in these comparisons.

6.1.4 Virtual origin

The convector heaters had fans to force the air horizontally through the heating element. The warm air travelled horizontally for about 1 m before it rose vertically in a turbulent plume. Figure 6.5 shows the temperature profile with different distances from a heater with the power of 315 W. As shown in the figure, the temperature reduced dramatically away from the heater as a result of entrainment. The horizontal jet has disappeared by the third vertical profile, indicating that a plume was generated about 1 m away from a heater. For the sake of simplicity, we assume that the virtual origin of the heater is that horizontal distance, which is taken as 1 m. Although the assumption based on visual observations causes uncertainty, it gives reasonable predictions of the room air stratification.

6.2 Stratification comparisons – interior zone

In this section, we compare the stratification measured in the laboratory experiments and the room tests. Smoke was used to make the temperature stratification visible in the test chamber, and food dye was used in salt water for flow visualization in our laboratory (figure 6.6). Quantitatively, we applied our theoretical model to provide reasonable predictions for room stratification. Further, we observe the same effects of multiple diffusers for experiments of both scales.

6.2.1 Stratification in small-scale and full-scale experiments

A well-distinguished two-layer stratification was observed in our small-scale salt tank experiments, in which all walls are insulated. However, in a real building other factors such as heat exchanges with the surfaces and radiation, the non-uniform temperature under the floor, and the differences in heat sources, etc, alter the stratification. Therefore, a complicated stratification occurs in the room test chamber. In spite of these differences of the stratifications between experiments at two scalings, figure 6.6 shows some common features from the

(a)

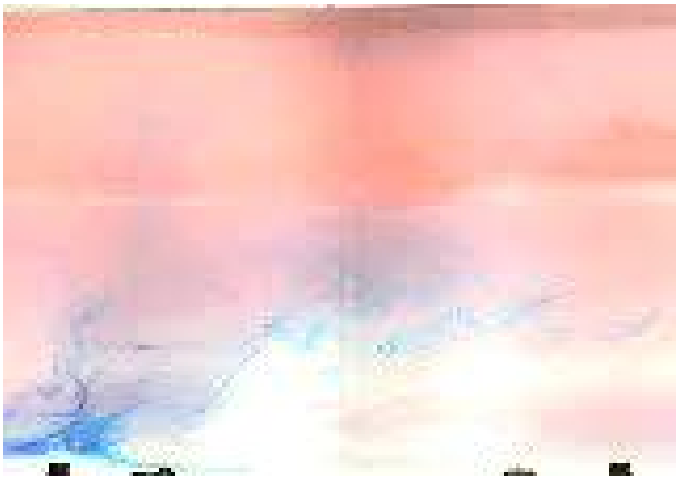

(b)

Figure 6.6: Visualized stratification comparisons between (a) a full-scale room test with smoke; and (b) a small-scale experiment with blue food dye.

visualized stratification comparisons between a salt tank experiment and a room chamber test. Smoke was injected out of a diffuser, and stays in the lower zone of the room. Similar observation was seen in the salt tank. The blue dye injected at the orifice of a diffuser nozzle does not penetrate the upper region of the tank, but stays in the lower region.

We assume that all diffusers are identical, and all heat sources are the same. Then, we divide the entire space into sub-regions by the number of the heat sources. Each sub-region has the same number of diffusers. Therefore, the stratification in each sub-region is no different from the others, thus giving the same stratification for the entire space. For the tests PG-H5-9 and PG-H5-11 (2 and 1.5 diffusers per heater, respectively), in which cases the number of diffusers is larger than that of heat sources, we used the multiple-diffuser model discussed in Chapter 3. For the test PG-H5-10 with 0.5 diffusers per heater, the multiple-source model presented in Chapter 4 is considered since the number of diffusers per heat source is less than 1.

Quantitatively, our model provides reasonable two-layer representation of the stratification for the room tests in table 6.1 shown in figure 6.7. It is seen in figure 6.7 that the upper-layer temperature has been well predicted, which gives better results for heat balance calculation compared with the averaged temperature in the entire room used by EnergyPlus. The lower-layer is more stratified in reality, and is hard to be represented by one uniform temperature as we did in our simple model. The reason for these generally smoother temperature profiles in the test chamber is complicated, such as the heat transfer through the floor; the non-uniform supplied air temperature from each diffuser; and the location of the sources, etc. However, the predicted lower zone temperature is a good estimate for the averaged temperature in the occupied zone. The interface height calculated by our two-layer model is in the transition region. This simplified two-layer model provides fairly good results for energy calculations, but is not so good for comfort studies.

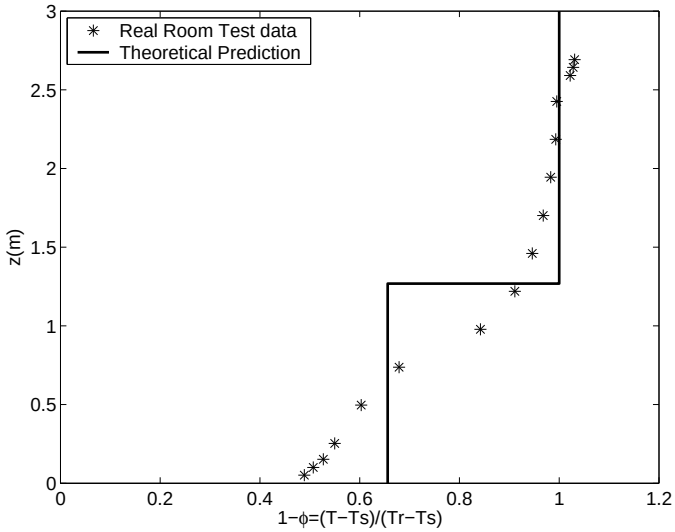

(a)

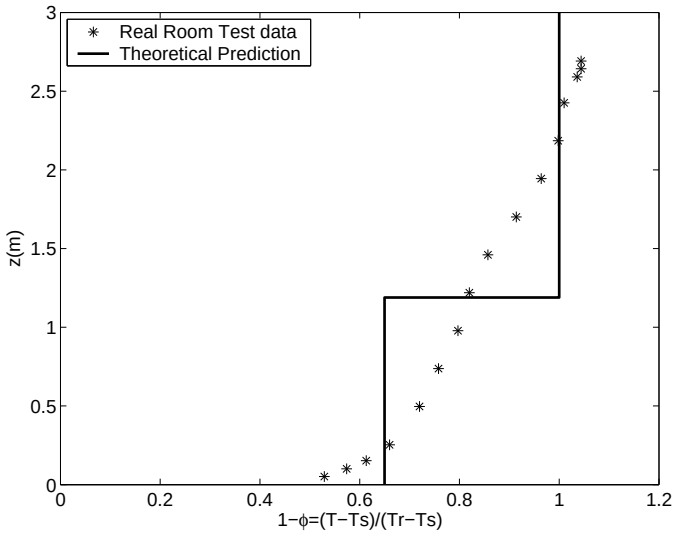

(b)

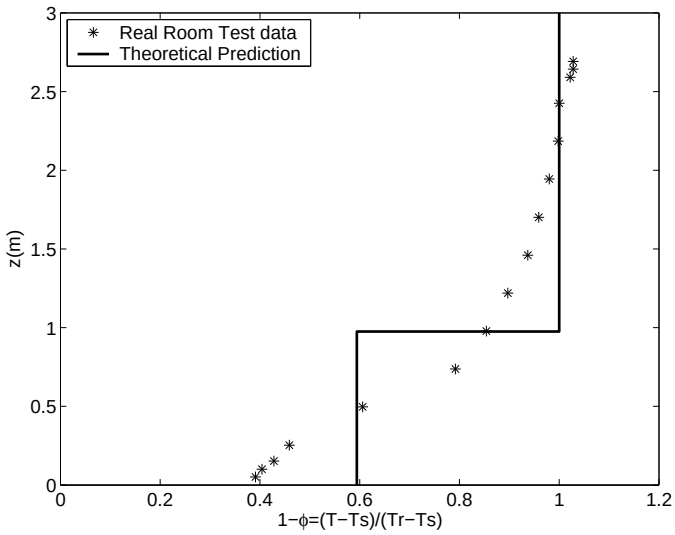

(c)

Figure 6.7: Two-layer model predictions are compared with full-scale measurements, where ϕ is defined in (6.9). (a) Run PG-H5-9; (b) Run PG-H5-10; (c) Run PG-H5-11.

6.2.2 Effects of multiple diffusers for small-scale and full-scale experiments

Exp. No.	$B(\mathrm{cm}^4\mathrm{s}^{-3})$	$M(\mathrm{cm}^4\mathrm{s}^{-2})$	$Q_f(\mathrm{cm}^3\mathrm{s}^{-1})$	n'	Tank Label
1	69.3	182	15.2	1	A
2	68.2	45	7.6	2	A
3	70.1	26	5.0	3	B

Table 6.2: Three different experimental conditions for the small-scale multiple diffusers experiments. B is the buoyancy flux of the heat source, M and Q_f are the momentum fluxes and the volume fluxes of each cooling diffuser. n' is the number of diffusers per plume.

In Chapter 3, we studied the effects of multiple diffusers in a UFAD system. Figure 3.5(a) shows that when the total ventilation flow rate is fixed, increasing the number of diffusers per plume will decrease the interface height, increase the buoyancy difference with the limit approaching the displacement ventilation case, and leave the upper layer temperature unchanged.

Figure 6.8 (a) shows three laboratory experiments with the same heat load B and ventilation flow rate Q_f. With the number of diffusers per plume n' increasing from 1 to 3, the upper layer reduced gravity which is determined only by B and Q, remains unchanged within experimental error. Both the lower layer reduced gravity and the interface decrease as n' changes from 1 to 3.

Figure 6.8 (b) demonstrates six UFAD room test runs with the same heat load and ventilation flow rate. These six runs were selected from many diffuser study test runs, which CBE believes to have good measurements with minor radiation and airflow leakage effects. Heat sources now are typical workstations as shown in figure 6.2. The number of diffusers per workstation n' varies from 0.67 to 2.33. When we compare the test runs with n' increasing from 1 (yellow line) to 2 (red line), we see that the upper layer temperature T_r remains the same, but the temperature profile gets more stratified and the interface height decreases. This trend is consistent with that observed in our salt-tank experiments.

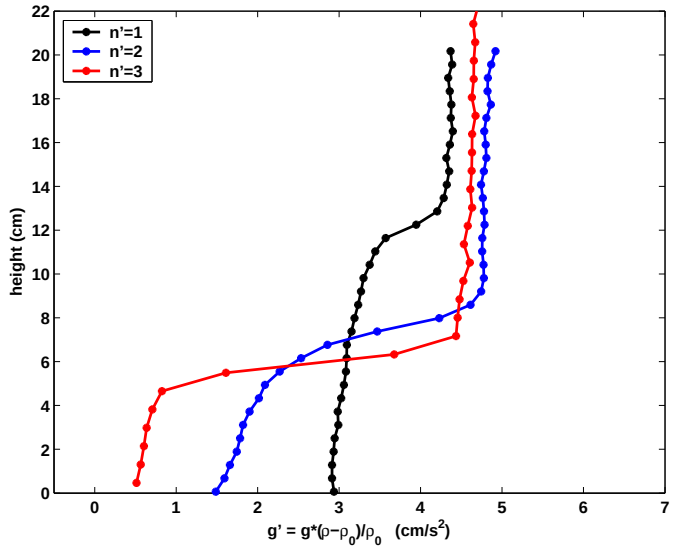

(a)

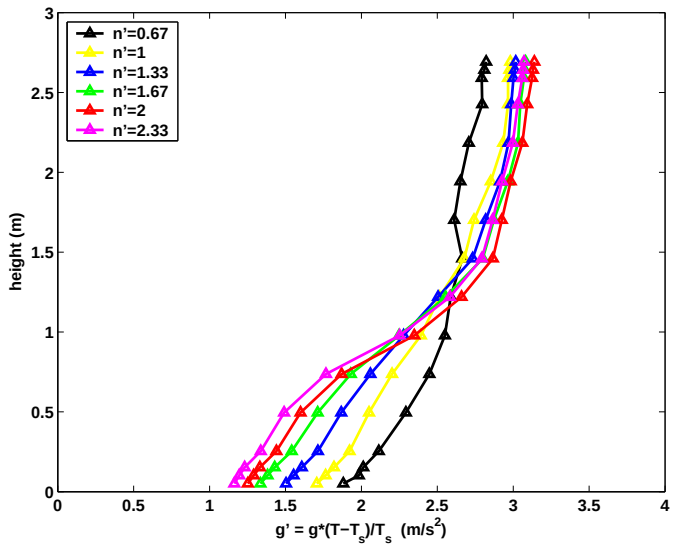

(b)

Figure 6.8: Data comparisons of multiple-diffuser study with fixed total heat load and total room ventilation rate (a) in small-scale experiments; (b) in full-scale room tests.

Test ID	W(kW)	Q(m^{3}s^{-1})	T_s(K)	n	m	n'	Γ
F1	2.27	0.181	292	4	6	0.67	18.62
F2	2.29	0.183	292	6	6	1	11.30
F3	2.31	0.194	291	8	6	1.33	8.60
F4	2.30	0.182	291	10	6	1.67	5.92
F5	2.25	0.178	292	12	6	2	4.62
F6	2.26	0.189	292	14	6	2.33	4.15

Table 6.3: Six different experimental conditions for the multiple diffusers experiments in a real UFAD room chamber. W is the heat load, Q is the room air flow rate; and T_s is the supply air temperature. n and m are the numbers of Krantz swirl diffusers and workstations, respectively. n' is the number of diffusers per workstation. Γ is the non-dimensional parameter defined by (6.7).

6.3 Non-dimensional scaling comparisons

In order to determine whether the scaling of the laboratory tank experiments matches that of the room chamber tests, we examine non-dimensional scaling comparisons in this section. We first define non-dimensional parameters Γ and ϕ, which account for the inputs and corresponding stratification in a UFAD system, respectively. Both full-scale room testing data and small-scale experimental measurements collapse on a single line in Γ-ϕ figure. This fitting line verifies that the scalings are matching, and further, it provides the temperature in both layers for given values of Γ. We also obtain a Γ-$\hat{h}_i$ plot based on the small-scale experimental data, where $\hat{h}_i$ is the non-dimensional interface height. The fitting line gives reasonable estimates for the interface height position in a real UFAD room.

6.3.1 Definition of non-dimensional parameters

Lin & Linden (2005) showed that in a UFAD system, the buoyancy flux of the heat source B and the momentum flux of the cooling jets M are the controlling parameters on the stratification. H is not the critical length scale for the stratification, because the region above the interface plays no role for the

stratification - except for a transient response. With a higher room height H, it will take longer for the stratification to reach steady state, but the upper layer temperature will not change since it is determined by B and Q_f only. Therefore, a non-dimensional parameter Γ can be defined from B, M and the effective area of a diffuser A_d as

$$\Gamma = \frac{M^{3/4}}{B^{1/2}\sqrt{A_d}} = \frac{(Q^2/A_d)^{3/4}}{B^{1/2}\sqrt{A_d}} = \frac{Q^{3/2}}{A_d^{5/4}B^{1/2}}. \tag{6.5}$$

for single-diffuser, single-source cases.

Physically, Γ represents the competition between stratification and mixing, because B is the source to build up the stratification while M measures the mixing of the diffusers. For the same geometry of the diffusers, large Γ means that the mixing dominates, and for small Γ we expect more stratification in the space. Practically, Γ is a parameter only based on external variables - B, Q and A_d. Therefore, it does not require the geometry of the space or the internal measurements, which is a big advantage from the viewpoint of design.

For multi-diffuser and multi-source cases, the idea of dividing the whole enclosure into sub-regions with equal number of diffusers and single heat source in each sub-region is again applied. The air flow and the heat load into each sub-region Q' and B' will be $Q' = Q/m$ and $B' = B/m$ respectively, where m is the number of heat sources, Q and B are the total air flow and the total heat load for the entire UFAD space. Then the momentum flux each diffuser per heat source carries is $M_d = (\frac{1}{n'}Q')^2/A_d$, where n' is the number of diffusers per heat source. Therefore, (6.5) will be modified as

$$\Gamma = \frac{(n'M_d)^{3/4}}{B'^{1/2}\sqrt{n'A_d}} = \frac{Q'^{3/2}}{(n'A_d)^{5/4}B'^{1/2}} = \frac{Q^{3/2}}{m(n'A_d)^{5/4}B^{1/2}}. \tag{6.6}$$

In a real full-scale room, the total room net heat load (plume heat input, minus the room losses) and the total net flow rate coming from the diffusers (input room air flow, minus the room leakage) should be considered. Further, the vertical

component of momentum flux should be used.

$$\Gamma = \frac{(Q\cos\theta)^{3/2}}{m(n'A_d)^{5/4}(0.0281W)^{1/2}}, \tag{6.7}$$

where, Q is the net flow rate coming out from all diffusers (m^3/s), W is the total net heat load (kW), A_d is the effective area of each diffuser (m^2), n' is the number of diffusers per heat source, θ is the angle between the diffuser slots and the vertical direction and m is the number of heat sources.

The second dimensionless parameter - the ventilation effectiveness ϕ, which indicates the strength of stratification, is defined as

$$\phi = \frac{\rho_u - \rho_l}{\rho_u - \rho_o}, \tag{6.8}$$

where ρ_u and ρ_l are the fluid density of the upper layer and lower layer, respectively, and ρ_o is the source density of diffusers in our small-scale salt-tank experiments. Equivalently, in terms of temperature

$$\phi = \frac{T_r - T_{oz}}{T_r - T_s}, \tag{6.9}$$

where T_r, T_{oz} and T_s (K) are the return air temperature, the occupied zone temperature and the supply temperature, respectively.

The maximum stratification corresponds to $\phi = 1$ (displacement ventilation case), while $\phi = 0$, implies that there is no stratification (well-mixed ventilation case).

Using dimensional analysis we find an equivalent parameter Γ for a perimeter zone with a single diffuser

$$\Gamma_L = \frac{Q}{B_L^{1/3}A_d}, \tag{6.10}$$

where, Q (m^3/s) and B_L (m^3/s^3) are the total flow rate and the total heat load per unit width in the perimeter zone.

With n identical diffusers in the perimeter zone, we divide the whole perimeter zone by the number of diffusers so that each sub-zone has a single diffuser. The air flow and the heat load per unit width into each sub-zone Q' and B'_L will be $Q' = Q/n$ and $B'_L = B_L$, respectively. The parameter Γ_L is then defined as

$$\Gamma_L = \frac{Q}{(B_L)^{1/3} n A_d}. \tag{6.11}$$

Note that (6.11) reduces to (6.10) when $n = 1$.

In a real room, the heat load per unit area W_a(kW/m^2) caused by solar insolation on the exterior wall is provided. So, the buoyancy flux per unit length $B_L = 0.0281 W_a H$, where H is the room height. Obviously, the higher the room is, the more heat load per unit width is for the room. Then, for a perimeter zone with n diffusers

$$\Gamma_L = \frac{Q}{(0.0281 W_a H)^{1/3} n A_d}. \tag{6.12}$$

6.3.2 Interior zone scaling comparisons between small-scale and full-scale experiments

Figure 6.9 and figure 6.10 show that the small-scale and full-scale experimental data in the Γ-ϕ plot. The salt tank experiments include single-plume single-diffuser cases (with plume on or above the floor) and multiple-plume multiple-diffuser ones. The room chamber tests include heat sources as manikins, printers and workstations. The number of swirl Krantz diffusers varies from 2 to 12. As seen in figure 6.10, the experimental data collapse on the same fitting line in log-log Γ-ϕ plot, which provides evidence that our salt tank experiments have included most of characteristics of a UFAD system and that the scalings match with that of room chamber tests. The fitting line $y = -0.76x + 0.47$ shows that, as expected, ϕ decreases as Γ increases, since larger Γ means more mixing and less stratification. The least-square fit in figure 6.10 allows us to calculate the occupied zone temperature from a knowledge of the diffuser design, the ventilation flow rate, the heat

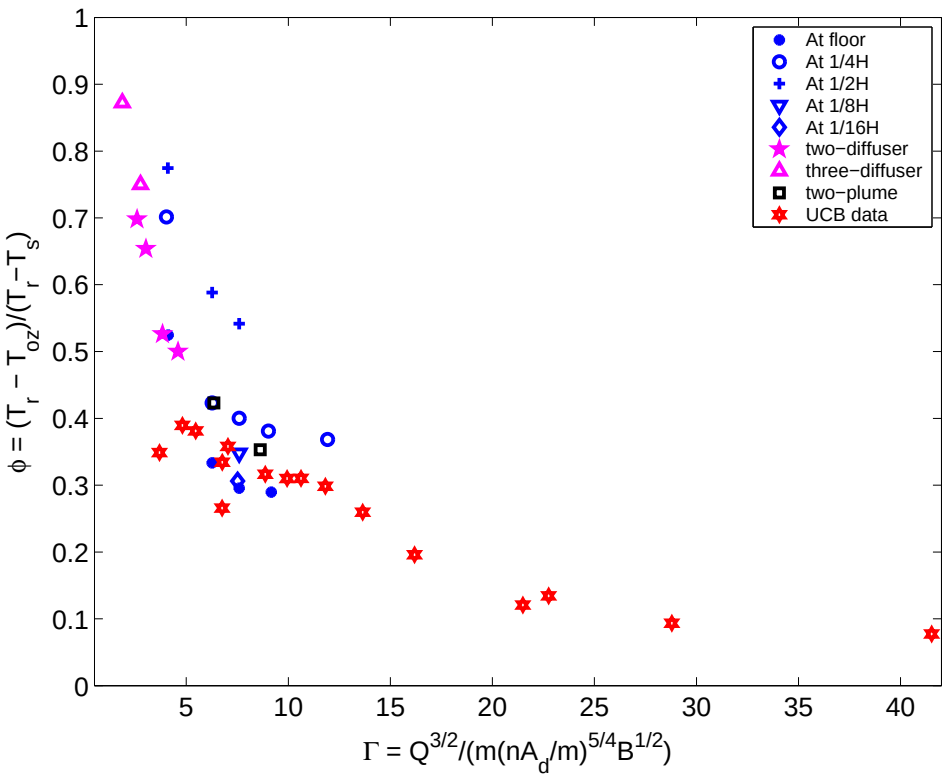

Figure 6.9: Data comparisons in the non-dimensional regular Γ-ϕ plot.

load and the supply temperature.

In order to complete the description of the stratification, the interface height is needed. Figure 6.11 shows the dimensionless interface height ($\hat{h}_i = h/\sqrt{n'A_d}$) of our small-scale experiments plotted against Γ. Based on the discussion in § 3.2.2, for the experiments with elevated heat source, the interface heights have been modified by (6.13).

$$h' = h - \frac{1}{2}h_s + z_v, \tag{6.13}$$

where, h_s and z_v are the vertical position and the virtual origin of the elevated heat source in each sub-region. All data then are located along a line $y = 7.43x - 1.35$ in figure 6.11.

Therefore, if we have the supply temperature: T_s (K); the number of

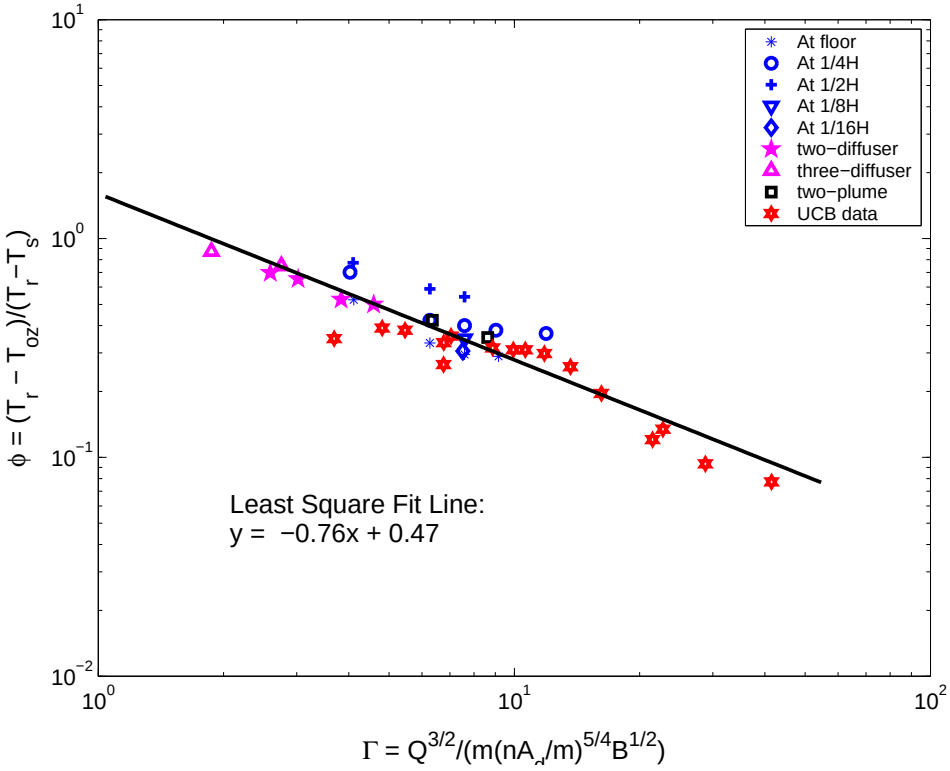

Figure 6.10: Data comparisons in the non-dimensional log-log Γ-ϕ plot.

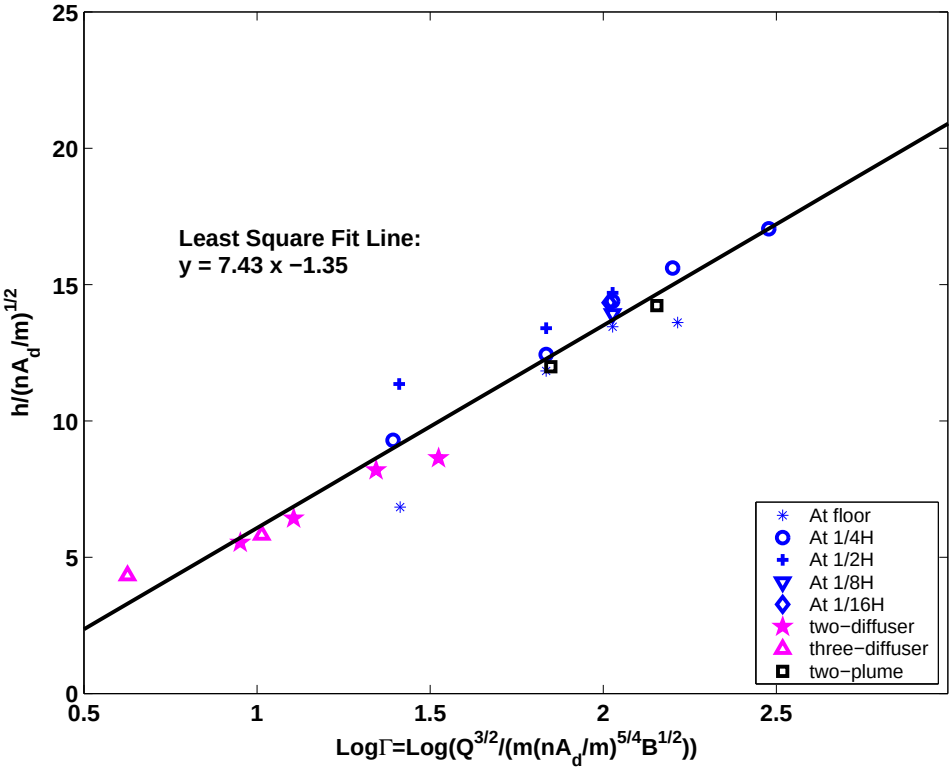

Figure 6.11: Non-dimensional interface height of small-scale experiments.

diffusers: n; the number of heat sources: m; the vertical position of heat sources: h_s (m); the virtual origin of heat sources: z_v (m); the heat load: W (kW); the effective area of a diffuser: A_d (m^2) and the total ventilation rate: Q (m^3/s), then the return air temperature T_r(K):

$$T_r = \frac{0.0281W}{Qg} T_s + T_s; \tag{6.14}$$

the occupied zone temperature T_{oz} (K):

$$T_{oz} = T_r - 1.6\Gamma^{-0.76}(T_r - T_s); \tag{6.15}$$

and the interface height h (m):

$$h = \sqrt{\frac{n}{m} A_d}\,[7.43\ln(\Gamma) - 1.35] + \frac{1}{2}h_s - \frac{1}{2}Z_v, \tag{6.16}$$

where Γ is defined in (6.7).

Now, we go back to figure 6.8 to compare scalings between the two figures. The three laboratory experiments in figure 6.8(a) and six chamber tests in figure 6.8(b) are included in figure 6.10. Therefore, the stratification scalings among those experiments are matching. It is difficult to determine where the interface is for a stratification of a room chamber, because the temperature profile is very stratified as in figure 6.8(b). This is why the interface data of room tests are not included in figure 6.11. However, based on the values of Γ given in table 6.3, the interface heights of these tests are estimated to range from 1.01 to 1.29 m by (6.16), if $z_v = 1$ m is assumed. This interface scaling is consistent with the stratification profiles shown in figure 6.8(b). Hence, the interface scalings of the chamber tests also match with our salt tank experiments.

6.3.3 Perimeter zone non-dimensional scalings

In the room chamber, bar grille diffusers are used in the perimeter zone, which is different from the circular diffuser used in our salt-tank experiments. The

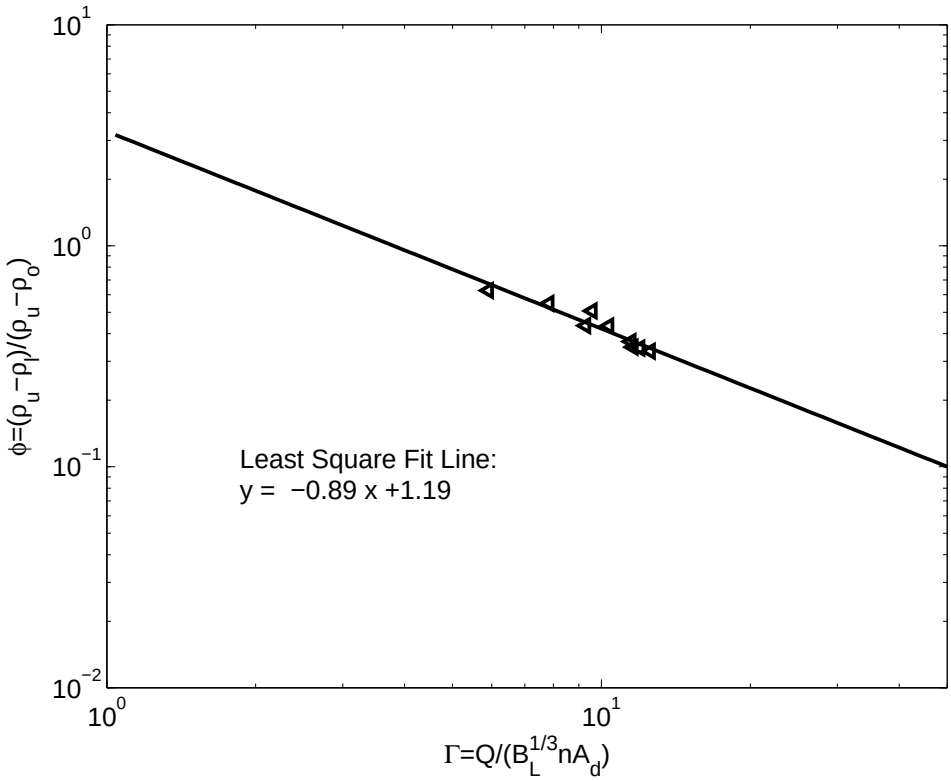

Figure 6.12: Small-scale line-plume experimental data (shown as triangles) in the non-dimensional log-log Γ-ϕ plot.

heat load per unit area varies with the blinds close or open, which is difficult to simulate in the small-scale experiments. In addition, the perimeter zone room chamber data are not available in a form that allows for detailed comparisons. Therefore, we have only done the elementary non-dimensional analysis for our line-plume experimental data, and will leave the comparisons with full-scale perimeter zone testing data to future research.

Using (6.11) and (6.8), the line-plume experimental data are showed in figure 6.12 and figure 6.13.Since the entrainment coefficient used in a line plume $\alpha_l = 0.06$ is different from the one used in a circular plume $\alpha = 0.117$, and also because Q is a different function of z, we expect that the fitting lines for line-plume experiments is different from that for circular plume data for interior zone.

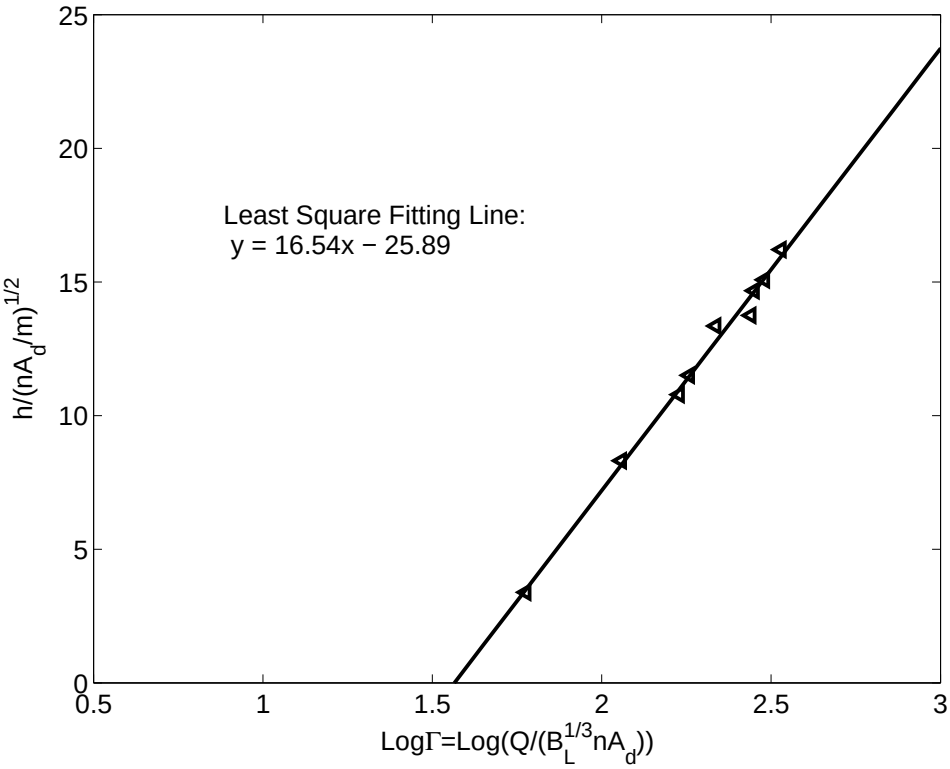

Figure 6.13: Non-dimensional interface heights of small-scale line-plume experiments (shown as triangles) plotted against $\log \Gamma$.

With these new fitting lines, a stratification for different values of Γ_a in a perimeter zone in a real UFAD system can be obtained by the following equation:

Given the supply temperature: T_s (K); the number of diffusers: n; the room height: H (m); the room width: D (m); the heat load per unit area: W_a (kW/m^2); the effective area of a diffuser: A_d (m^2) and the total ventilation rate: Q (m^3/s), then

the return air temperature T_r(K)

$$T_r = \frac{0.0281 W_a H D}{Qg} T_s + T_s; \tag{6.17}$$

the occupied zone temperature T_{oz} (K)

$$T_{oz} = T_r - 3.29\Gamma^{-0.9}(T_r - T_s); \tag{6.18}$$

and the interface height h (m)

$$h = \sqrt{A_d}\,[16.54 \ln(\Gamma) - 25.89] \tag{6.19}$$

where Γ is defined in (6.12).

6.4 Floor leakage study

In practical UFAD systems air enters the space from the plenum through the diffusers and also via small cracks and openings in the raised floor. This leakage flow can be as much as 30% of the flow through the diffusers. This leakage flow cools the space but, since the air enters with low momentum, it does not act as a UFAD flow bringing warm air down from the higher parts of the room. In fact, this leakage acts more like the supply air in a displacement system.

It is possible to simulate the effects of leakage in the laboratory by using two diffusers, one with a horizontal metal plate above it. The open diffuser acts as a standard UFAD diffuser while the covered diffuser acts like a displacement diffuser or leakage.

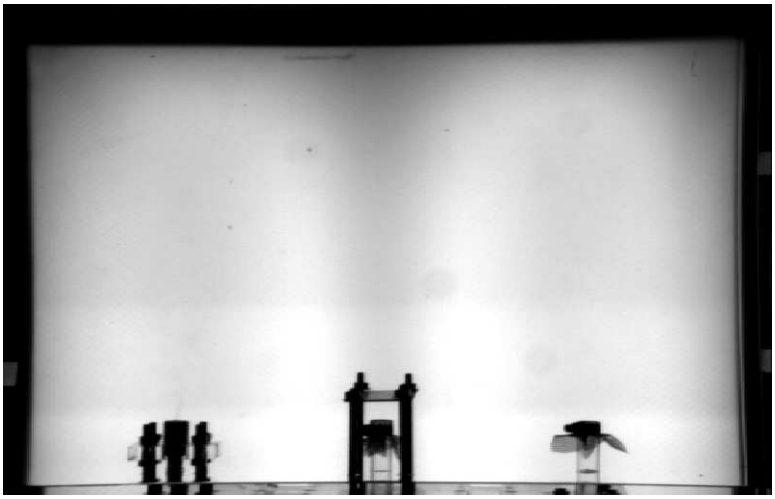

Figure 6.14: A steady-state experimental image of a UFAD system with a single plume on the left, a single diffuser on the right and a displacement ventilation diffuser in the middle which simulates the airflow leakage through the floor.

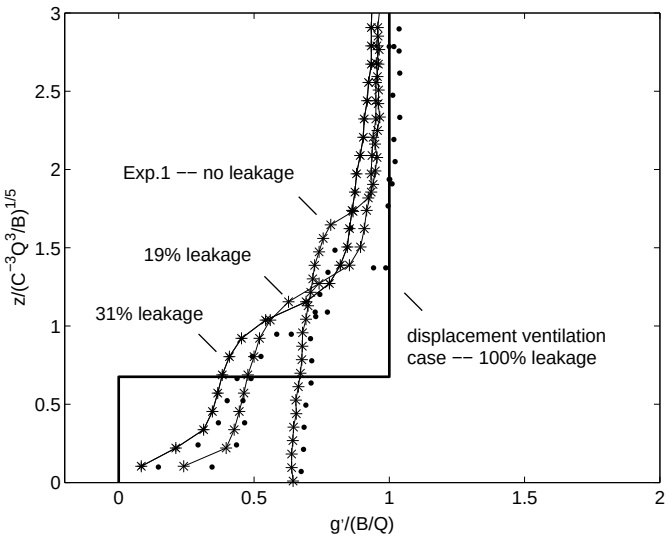

Figure 6.15: Experimental data comparisons among the experiments with the airflow floor leakage rate as 0, 19% and 31% of the total ventilation flow rate. The solid line is the theoretical predications for a displacement ventilation case which is equivalent to the floor leakage rate as 100%.

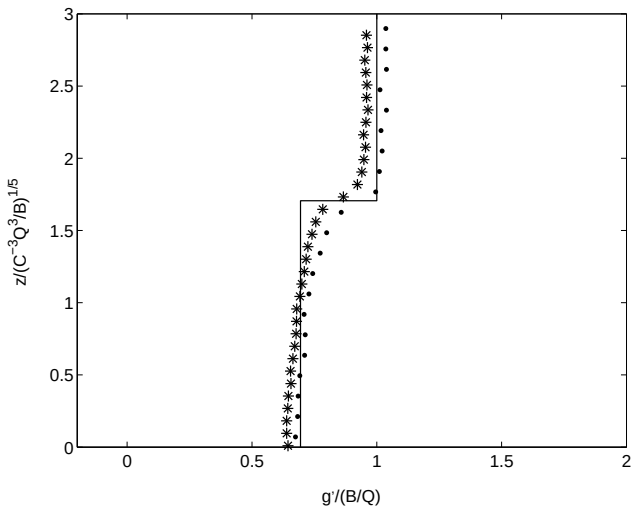

(a)

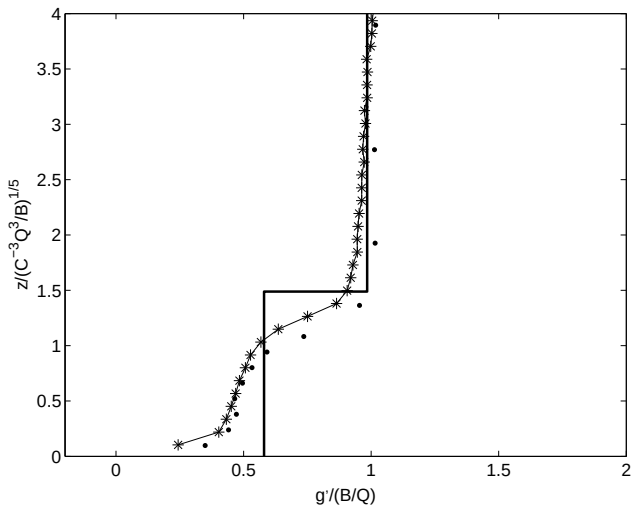

(a)

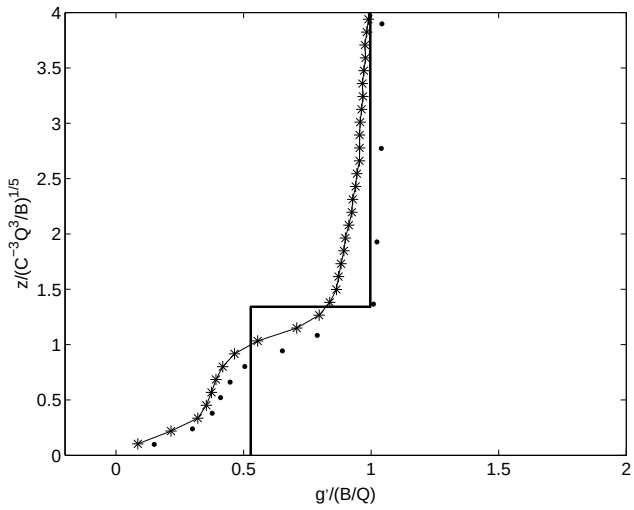

(b)

Figure 6.16: The theoretical model for floor leakage problem gives good agreements with the experimental data when the leakage rate is (a) 0 (displacement ventilation); (b) 19%; (c) 31% of the total ventilation flow rate.

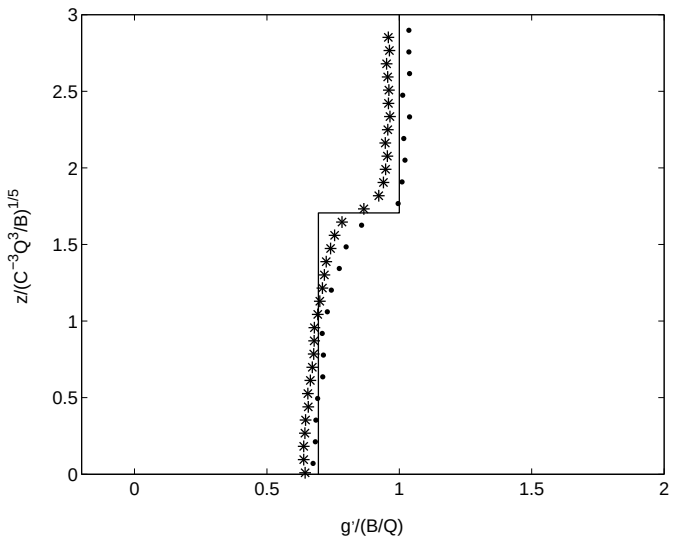

Figure 6.17: The buoyancy profile for Exp.1, which has no airflow leakage through the floor.

We carried out two experiments with the airflow leakage rate as 19% and 31% of the total ventilation flow, respectively, based on the conditions of Exp.1 in table 6.2. Figure 6.14 shows an experimental image at steady state, and we observe that stratification forms and a thin layer of the supply air is spreading on the floor.

The experimental buoyancy profiles with different floor leakage rate are compared in figure 6.15. With larger airflow leakage, the lower zone temperature and the interface height both drop. When the leakage rate reaches 100% of the total ventilation rate, the system turns to displacement ventilation. In all cases, the upper layer temperature remain unchanged as expected.

The single-plume single-fountain model can be applied to estimate the buoyancy profiles for the leakage experiments except that the momentum flux of the diffuser flow is now

$$M = \frac{(1-\eta)^2 Q^2}{A_d}, \tag{6.20}$$

where, η is the percentage of the airflow leakage out of the total ventilation airflow

Q, and A_d is the effective area of the diffuser. The comparisons between theoretical predications and experimental data for experiments with the leakage rate η as 19% and 31% are presented in figure 6.16. When $\eta = 100\%$, it is the displacement ventilation case and the theoretical profile is given as a solid line in figure 6.16. When $\eta = 0$, this floor-leakage model reduces to the single-plume single fountain model. The comparisons for Exp.1 are shown in figure 6.17. It is shown that the model gives reasonable agreements with the experimental data.

6.5 EnergyPlus

One goal of this research is to develop UFAD models that can be implemented in EnergyPlus, in order to allow design practitioners to model the energy performance of UFAD systems and to compare it with that of conventional systems. EnergyPlus is a free and publicly available program maintained by the U.S. Department of Energy. This will be the first comprehensive simulation program capable of modelling the energy performance of UFAD systems and comparing it with that of conventional systems.

EnergyPlus requires straightforward inputs and outputs. One approach to do this implement is to make complicated models representable by the same simple model with quantitative adjustments. We have developed UFAD interior zone models with multiple diffusers, multiple sources, elevated heat sources and floor leakage problem. As shown in figure 6.18, all these complicated model can be related to the simple single-source single-diffuser model. Suppose there are n equal diffusers and m equal heat sources, $n > m$ implies that multi-diffuser model should be used. Otherwise, the multi-source model is applicable. As discussed in Chapter 3 and Chapter 4, these models are quantitatively related to the single-source single-diffuser model by power laws. The effects of an elevated heat source is studied in §3.2.2, and the effects of floor leakage is discussed in §6.4. These two cases are both extensions for single-source single-diffuser model. When the

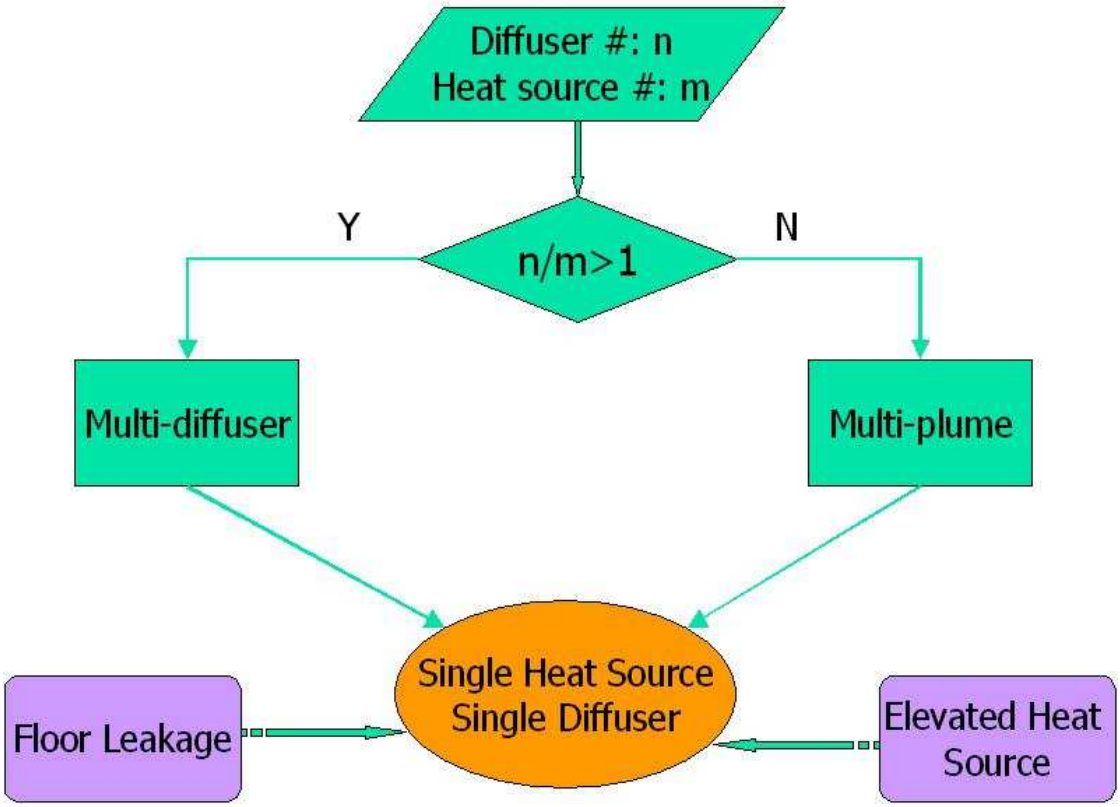

Figure 6.18: The flowchart of modelling an interior zone of a UFAD system. Complicated models reduce to the simple single-source single-diffuser model.

heat sources are of different strengths, we can use the approximate model (§4.2.3), which is based on the basic single-source single-diffuser model.

Another approach to develop a validated UFAD modelling capability for the whole-building energy simulation program, EnergyPlus is to use non-dimensional analysis. We have shown that the scalings of small-scale experiments match full-scale experiments. Therefore, from the scaling comparisons, explicit equations are obtained for both interior zone stratification (equation (6.14)-(6.16)) and perimeter zone stratification (equation (6.17)-(6.19)). These equations have been implemented into EnergyPlus, and have provided encouraging estimates for room stratifications, thus providing guidelines for UFAD design purpose.

6.6 Conclusion

The salk-tank laboratory experiments have dynamic similarity with full-scale UFAD room tests, which we have discussed in Chapter 1. In this chapter, we report qualitative and quantitative comparisons on the stratification and scaling between our small-scale experiments and full-scale room tests.

For the interior zone, we observe stratifications in both small-scale and full-scale experiments. Our two-layer theoretical model gives reasonable estimates of stratifications for the room tests. With the same heat load and ventilation flow rate, the more cooling diffusers there are in a UFAD system, the cooler the occupied zone is and the interface drops till it reaches the displacement ventilation limits. However, the return temperature remains the same for all number of diffusers. The same trend was also seen in small-scale experiments.

By using the non-dimensional analysis, two dimensionless parameters, Γ and ϕ were defined to compare the scalings of two different scale experimental results. Γ is the parameter based on external variables only. The parameter ϕ measures the degree of stratification. We find that ϕ decreases as Γ increases, because larger Γ means the diffusers have more ability to mix the air in the cham-

ber. Experimental data of both small-scale and full-scale are located on a trend line in log-log Γ-ϕ plot, therefore the laboratory stratification scaling matches the scaling of a real room. The interface scaling of the full-scale tests was shown to match that of the small-scale experiments, and can be estimated by the fitting line for laboratory scaled experiments in figure 6.11. Further, the explicit equations about the temperatures in both layers and the interface position, (6.14)(6.15) and (6.16), are determined. These equations have been implemented in EnergyPlus, and have been able to provide us with effective estimates of energy usage and UFAD performance.

For the perimeter zone, only small-scale experimental data were analyzed since the full-scale data are not yet available. Non-dimensional analysis for the small-scale data, also provides us with similar simple equations to estimate the room stratifications.

The salt-tank experiments are simply set up compared with the complexities in the room chamber. Our two-layer uniform temperature theoretical model is too straightforward to simulate the gradual changes in the room stratification. We have only selected those tests with simple setup and good controls to compare with our small-scale experiments. Therefore, all the comparisons presented in this chapter are preliminary. Although it is encouraging to reach this stage, further research remains to be done.

The airflow leakage through the floor is a big concern when a UFAD system is designed. Our laboratory experiments have simulated this leakage problem by using a displacement diffuser in the tank. The modified single-source single-diffuser model was used to estimate the stratifications and the results have been compared with the experimental data, which shows good agreement. The effects of leakage in a real room are to decrease the lower zone temperature and the interface height, which can cause discomfort for occupants in the room.

The complex models developed in this research, such as multi-identical-diffuser model, multi-identical-source model and elevated-source model, can be

related quantitatively to the basic single-diffuser single-source model. The others, like approximate multi-unequal-source model and floor-leakage model, can be solved based on the simple single-diffuser single-source model. These relationships are very helpful in the implementation for EnergyPlus.

Bibliography

Alberson, M. L., Dai, Y. B., Jensen, R. A. & Rouse, H. 1950 Diffusion of submerged jets. *Trans. ASCE* **115** 639–697.

Bachelor, G. K. 1954 Heat convection and buoyancy effects in fluids. *Quart. J. Roy. Met. Soc.* **80**, 339–358.

Baines, W. D. 1975 Entrainment by a plume or jet at a density interface. *J. Fluid Mech.* **68**, 309–320.

Baines, W. D. & Turner, J.S. 1969 Turbulent buoyant convection in a source in a confined region. *J. Fluid Mech.* **37**, 51–80.

Bauman, F. 2004 Underfloor Air Distribution Design Guide. the American Society of Heating, Refrigerating and Air-Conditioning Engineers (ASHRAE), University of California, Berkeley.

Bauman, F. & Webster, T. June 2001 Outlook for underfloor air distribution. *ASHRAE Journal* **43 6**, 18–27.

Bloomfield, L. J. & Kerr, R. C. 1998 Turbulent fountains in a stratified fluid. *J. Fluid Mech.* **358**, 336–356.

Bloomfield, L. J. & Kerr, R. C. 2000 A theoretical model of a turbulent fountain. *J. Fluid Mech.* **424**, 197–216.

Cardoso, S. S. S. & Woods, A. W. 1993 Mixing by a turbulent plume in a confined stratified region. *J. Fluid Mech.* **250**, 277–305.

Caulfield, C. P. & Woods, A. W. 2002 The mixing in a room by a localized finite-mass-flux source of buoyancy. *J. Fluid Mech.* **471**, 33–50.

Cooper, P. & Linden, P. F. 1996 Natural ventilation of an enclosure containing two buoyancy sources. *J. Fluid Mech.* **311**, 153–176.

Dalziel, S. B. 1993 Rayleigh-taylor instability: experiments with image analysis. *Dyn. Atmos. Ocaens* **20**, 127–153.

Dalziel, S. B. 1993 Digimage (image processing software for fluid dynamics). *Tech. Rep.* Department of Applied Mathematics and Theoretical Physics (DAMTP), University of Cambridge, UK.

Ellison, T. H. & Turner, J.S. 1959 Turbulent entrainment in stratified flows. *J. Fluid Mech.* **6**, 423–448.

Fischer, H. B., List, E. J., Koh, C. Y., Imberger, J. & Brooks, N. H.1979 Mixing in inland and coastal water. *Academic Press*

Fisk, W. J. 2000 Health and productivity gains from better indoor environments and their relationship with building energy efficiency. *Ann. Rev. Energy Environ.* **25** 537–566.

Gladstone, C. & Woods, A. W. 2001 On buoyancy-driven natural ventilation of a room with a heated floor. *J. Fluid Mech.* **441**, 293–314.

Grahl, C. L. March 2002 Green Building Quiz: Underfloor Air Distribution Systems. *Environmental Design + Construction.*

Griffith, B. & Chen, Q. 2004 Framework for coupling room air models to heat balance model load and energy calculations. *International Journal of HVAC&R Research*, **10**, 91–111.

Hunt, G. R., Holford J. M. & Dally B.B. 2001 The dependence of the discharge coefficient on density contrast - experimental measurements. *Proc. of the 14th Australasian Fluid Mechanics Conference.*

Hunt, G. R. & Kaye, N. G. 2001 Virtual origin correction for lazy turbulent plumes. *J. Fluid Mech.* **435**, 369–377.

Hunt, G. R. & Linden, P. F. 2001 Steady-state flows in an enclosure ventilated by buoyancy forces assisted by wind. *Building and Environment* **36**, 707–720.

Hunt, G.R., Linden, P.F. & Cooper, P. 2001 Thermal stratification produced by jets and plumes in enclosed spaces. *Building and Environment* **36**, 871–882.

Ito, H. & Nakahara, N. 1993 Simplified calculation model of room air temperature profile in under-floor air-condition system. *International Symposium on Room Convection and Ventilation Effectiveness ISRACVE, ASHRAE.*

Jiang, Y., Su., M., & Chen, Q. 2003 Using large eddy simulation to study airflows in and around buildings. *ASHRAE Transactions*, **109**.

Kaye, K.N. & Linden, P.F. 2004 Coalescing axisymmetric turbulent plumes. *J. Fluid Mech.* **502**, 41–63.

Kumagai, M. 1984 Turbulent buoyant convection from a source in a confined two-layered region. *J. Fluid Mech.* **147**, 105–131.

Li, Y. 1993 Role of multizone models in indoor air flow and air quality analysis. *Indoor Environ.* **2**, 149–163.

Lin, Y.-J. 2003 Plumes and Jets in Semi-Confined Spaces. *PhD thesis, Unveristy of California, San Diego.*

Lin, Y.-J. P & Linden, P. F. 2005 A model for an under floor air distribution system. *Energy and Buildings* **37**, 399–409.

Linden, P. F. 1973 The interaction of a vortex ring with a sharp density interface: a model for turbulent entrainment. *J. Fluid Mech.* **60**, 467–480

Linden P. F. 1999 Natural Ventilation. *Ann. Rev. Fluid Mech.* **31**, 201–238.

Linden, P. F. & Cooper, P. 1996 Multiple sources of buoyancy in a naturally ventilated enclosure. *J. Fluid Mech.* **311**, 177–192.

Linden, P. F., Lane-Serff, G.F. & Smeed, D.A. 1990 Emptying filling boxes: the fluid mechanics of natural ventilation. *J. Fluid Mech.* **212**, 309–336.

Linden, P. F. 2000 Convection in the environment. *Cambridge Press* UK.

Linden, P. F. 1973 The interaction of a vortex ring with a sharp density interface: a model for turbulent entrainmente. *J. Fluid Mech.* **60**, 467–480.

Li Y., Sandberg M. & Fuchs L. 1992 Vertical temperature profiles in rooms ventilated by displacement: full-scale measurement and nodal modeling *Indoor Air* **2**, 225–243.

List, E. J. 1982 Turbulent jets and plumes. *Ann. Rew. Fluid Mech.* **14**, 189–212.

Liu, Q. A., & Linden, P. F. 2006 The fluid mechanics of underfloor air distribution. *J. Fluid Mech.* **554**, 323–341.

McDougall, T. J. 1981 Negatively buoyant veritcal jets. *Tellus* **33**, 313–320.

Mizushina, T., Ogino, F., Takeuchi, H. & Ikawa H. 1982 An experimental study of verical turbulent jet with negative buoyancy. *Warme-und Stoffubertragung* **16** 15–21.

Mora, L., Gadgil, A. J. & Wurtz, E. 2003 Comparing zonal and CFD model predictions of isothermal indoor airflows to experimental data. *Intl. J. Indoor Environ. and Health* **13**, 77–85.

Morton, B. R. 1959 Forced plumes. *J. Fluid Mech.* **5**, 151–163.

Morton, B. R. 1962 Coaxial turbulent jets. *Intl J. Heat Mass Transfer* **5** 955–965.

Morton, B. R., Taylor, G. I. & Turner, J. S. 1956 Turbulent gravitational convection from maintained and instantanious sources. *Proceedings of the Royal Society of London* **A 234**, 1–23.

Mundt, E. 1990 Convective flow above common heat source in rooms with displacement ventilation. *Proc. of the International Conference on Engineering Aero- and Thermaodynamics of Ventilated Room, ROOMVENT '90*,

Musy, M., Winkelman, F. & Wurtz, E. 2002 Automatically generated zonal models for building airflow simulation: principles and application. *Building and Environ.* **37**, 873–881.

Nielsen, P.V. 1988 Displacement ventilation in a room with low-level diffusers. *Presented at the Kaelte-Klima-Tagung 1988, Deutscher Kaelte- und Klimatechnischer Verein e. V.*.

Priestley, C.H.B. 1959 Turbulent transfer in the lower atmosphere. *University of Chicago Press*

Rees, S. J. & Haves, P. 2001 A nodal model for displacement ventilation and chilled ceiling systems in office spaces. *Building and Environ.* **36**, 753–762.

Rouse, H., Yih, C. S. & Humphreys, H. W. 1952 Gravitational convection from a boundary source. *Tellus* **4**, 201–210.

Seban, R. A., Behnia, M. M. & Abreu, K. E. 1978 Temperatures in a heated jet dischared downward *Intl J. Heat Mass Transfer* **21** 1453–1458

Schmidt, W. Z. 1941 Turbulent ausbreitung eines storms erhizter luft. *Z. angew. Math Mech.* **5**, 265–278 351–363.

Sodec, F. & Craig R. 1990 The underfloor air supply system – the European experience. *ASHRAE Transactions* **96** No. Part 2.

Stanke, D. 2001 Underfloor air distribution: Turning air distribution upside down. *Trane Engineers Newsletter* **30-4** 355–386.

Webster, T., Lukaschek, W., Bauman, F., Dickerhoff, D., Jin, H., Daly, A., & Doebber, I. 2005 Energy performance of underfloor air distribution (UFAD) systems. *Project Final Report*

Turner, J. S. 1966 Jets and plumes with negative or reversing buoyancy. *J. Fluid Mech.* **26**, 779-792.

Turner, J. S. 1973 Buoyancy effects in fluids. *Cambridge University Press*

Woods, A. W. & Caulfield, C. P. 1992 A laboratory study of explosive volcanic eruptions. *J. Geophys. Res.* **B 97**, 6699–6712.

Zhang, Q. 2001 Room air stratifcation model for underfloor air distribution system. *MS thesis, University of California, Berkeley.*

Zhang, H., Huizenga, C., Arens, E. & Yu, T. 2005 Modelling thermal comfort in stratified environments. *Proceedings, Indoor Air 2005: 10th International Conference on Indoor Air Quality and Climate, Beijing, China*